STUDIES ON BULK AND THIN FILMS OF LEAD (Pb) MODIFIED CHALCOGENIDE GLASSES

By
Akhyaya K. Pattanaik

Department of Physics
Indian Institute of Technology Guwahati
Guwahati - 781039, INDIA

December, 2002

भारतीय प्रौद्योगिकी संस्थान गुवाहाटी
Indian Institute of Technology Guwahati

Studies on bulk and thin films of Lead (Pb) modified chalcogenide glasses

A thesis submitted
in partial fulfillment of the requirements
for the award of the degree of

Doctor of Philosophy

by
Akhyaya K. Pattanaik

Department of Physics
Indian Institute of Technology Guwahati
Guwahati-781039, INDIA
December, 2002

Dedicated to my mother

Certificate

It is certified that the work contained in the thesis entitled "**STUDIES ON BULK AND THIN FILMS OF LEAD (Pb) MODIFIED CHALCOGENIDE GLASSES**" by **Akhyaya K. Pattanaik**, a student in the **Department of Physics**, **Indian Institute of Technology Guwahati** for the award of degree of **Doctor of Philosophy** has been carried out under my supervision and that, this work has not been submitted elsewhere for a degree.

(Dr. A. Srinivasan)

Department of Physics
Indian Institute of technology Guwahati
Guwahati-781039

भारतीय प्रौद्योगिकी संस्थान गुवाहाटी
Indian Institute of Technology Guwahati

ACKNOWLEDGEMENTS

With the warmest affection, I would like to express my deepest gratitude to Dr. A. Srinivasan for giving me the opportunity to work under his supervision. He has always been a source of new ideas for me. His constant encouragement, advice and guidance made me bold to complete my Ph. D. work without any difficulty.

I would like to pay my sincere and heartfelt gratitude to Dr. Sasanka Ghosh, who left us forever before the completion of my thesis.

I am grateful to Dr. C. Y. Kadolkar, Dr. S. Ravi and Dr. J. B. Baruah for their valuable suggestions to improve my work.

I would like to thank all the faculty members of our department for their timely suggestions and kind help when I needed.

I would like to express my gratitude to Dr. P.S. Robi for permitting me to work in the Materials Science Laboratory, Department of Mechanical Engineering, IIT Guwahati for the measurement of microhardness of my samples. Taking the opportunity, I would like to thank all the members of the mechanical workshop for extending their help during the fabrication of components for my experimental set-up.

I am also thankful to Mr. Sidananda Sarma, Mr. Lokesh Chakravarty, Mr. Chandan Borgohain, Mr. Subhajit Chowdhury, Mr. Dibakar Pratim Deb and Mr. Madan Deka who unfailingly extended their assistance and co-operation to me whenever I needed. My sincere thank to Mr. Pranab Goswami and Mr. Abhijit Borah for their unforgettable help in recovering the data which was temporarily lost from the computer during my thesis writing.

I would like to express my thanks to Dr. Sudipta Nandy for his numerous suggestions, encouragement and his parents for provide me a homely atmosphere during my stay at Guwahati.

I consider myself privileged and fortunate to have friends like Mr. Ullash K. Barik, Mr. Ramesh Mallik, Mr. Pankaj Patro and Mr. Biswajit Pradhan, Mr. Bhabani S. Mohapatra.

My special thanks to Mr. B. Indrajit Sharma for his constant encouragement and kind help. His presence always helped me in many ways. I would like to thank Mr. Manoranjan Kar, Mr. Pramod K. Nayak, Mr. Ardhendu S. Patra, Mr. Susanta Das, Mr. Kamlesh M. Alti, Mr. Hrishikesh Sarma, Mr. Rahul Bhattacharjee, Mr. Sanjay K Dehury and Mr. Bhagat L. Dutta who helped me in many important ways.

Besides, there are many people (including seniors, colleagues and juniors) inside the campus to whom I would like to thank for their encouragement and providing me a cheerful atmosphere since my admission at this institute. They have my deepest thanks and appreciation.

In addition, I am indebted to my mother, brothers and sisters-in-law for their love and affection without which I may not have reached this stage.

I would like to acknowledge Indian Institute of Technology, Guwahati and Council of Scientific and Industrial Research, India (CSIR) for giving me financial support to pursue my Ph. D. work.

(Akhyaya K. Pattanaik)

Preface

Chalcogenide glasses contain group VI (A) elements of the periodic table such as Sulphur, Selenium or Tellurium as their major constituent. Chalcogenide glasses are known to be *p*-type semiconductors. It was reported that Ge-Se glasses containing appropriate amounts of Bismuth (Bi) or Lead (Pb) exhibited *n*-type conduction. Bi modified chalcogenide glasses have received more attention in the literature as compared to Pb modified chalcogenide glasses. In this thesis, a systematic study of the electrical, thermal and optical properties of bulk and thin films of Pb modified chalcogenide glasses is reported. The basic interest in chalcogenide glasses exhibiting *p*-type to *n*-type charge carrier reversal and the general lack of information on thin films of these glasses are the motivations behind this work. The following glass systems have been taken up for study in this thesis work: (a) $Pb_xGe_{42-x}Se_{58}$ ($3 \le x \le 15$); $x_c \approx 9$, (b) $Pb_{20}Ge_xSe_{80-x}$ ($17 \le x \le 24$); $x_c \approx 21$, (c) $Pb_xGe_{42-x}Se_{48}Te_{10}$ ($3 \le x \le 15$); $x_c \approx 9$, (d) $Pb_{20}Ge_xSe_{70-x}Te_{10}$ ($17 \le x \le 24$); $x_c \approx 21$ and (e) $Pb_xIn_{25-x}Se_{75}$ ($1 \le x \le 7$); $x_c \approx 3$, where x_c represents the composition at which *p*- to *n*- type transition is expected to occur.

Bulk glass samples were prepared from high purity elements by the melt quenching technique. Thin films of the glasses were deposited on glass substrates by thermal evaporation of the respective bulk glasses. Amorphous nature of the as-quenched (and as-evaporated) samples was verified by x-ray diffraction. Melt quenched Pb-In-Se samples turned out to be partially crystalline in structure. Attempts were made to prevent nucleation of the crystalline phase during quenching and evaporation. Evaporation onto cooled substrates reduced the percentage of crystalline phase in the Pb-In-Se thin films. Thickness of the thin films was measured using an ellipsometer. The composition of the constituents in the glasses was

verified by microprobe analysis using a scanning electron microscope (SEM-EDX). Experimental observation of glass transition temperature (T_g) of the bulk samples was made to confirm the formation of glasses. Glass transition and crystallisation temperatures, heat capacity jump at the glass transition and the activation energy for glass transition were determined using a Differential scanning calorimeter (DSC). The majority charge carrier type in each glass composition (bulk and thin film) was determined by thermoelectric power (TEP) measurements. TEP measurements on bulk and thin films samples showed that the *p*- type to *n*-type transition occurred near x = 9 at. wt. % Pb in $Pb_xGe_{42-x}Se_{58}$ and $Pb_xGe_{42-x}Se_{48}Te_{10}$ glasses, near x = 21 at. wt . % Ge in $Pb_{20}Ge_xSe_{80-x}$ and $Pb_{20}Ge_xSe_{70-x}$ Te_{10} glass systems, and near x = 3 at. wt. % Pb in $Pb_xIn_{25-x}Se_{75}$ system. Electrical conductivity of the glasses in bulk and film form was measured from room temperature to 400 K using the four-probe technique. Optical band gap of glasses was determined from optical absorption measurements made with a dual beam ultraviolet-visible-near infrared spectrophotometer. Microhardness of bulk glasses was measured using a Vickers microhardness tester. All the experimental results were analysed based on the existing theoretical formalism. The thesis work arranged in six chapters. Chapter I would serve as a general introduction to the present work. Chapter II is devoted for explanation of the experimental techniques used in the above investigations. Chapter III contains details of the experimental findings on the bulk and thin films of Pb-Ge-Se glasses. Chapter IV discusses experimental results of bulk and thin films of Pb-Ge-Se-Te glasses. Chapter V explains the work done on bulk and thin films of Pb-In-Se glasses. Chapter VI is the concluding chapter in which an attempt would be made to summarise the work done on both bulk and thin films of Pb modified chalcogenide glasses. An attempt has been made to correlate the experimental

findings on bulk and thin films of these glasses. Possibilities of practical applications and scope of the future work in this area is also pointed out.

An Appendix containing the procedure for estimating the bond energy of hetero nuclear bonds is appended at the end. References cited in this thesis are listed at the end of the thesis.

भारतीय प्रौद्योगिकी संस्थान गुवाहाटी
Indian Institute of Technology Guwahati

Contents

Chapter 1
Introduction

Glass is a non-crystalline solid. The term glass was derived from the Latin term *glaesum,* which means *a lustrous and transparent material*. The term vitreous is often used as a synonym for glass [1]. The National Research Council *ad hoc* Committee on Infra-red Transmitting Materials in 1968 defined glass as, "*A glass is an x-ray amorphous solid which exhibits the glass transition, the latter being defined as that phenomenon in which a solid amorphous phase exhibits with changing temperature a more or less sudden change in the derivative thermodynamic properties, such as heat capacity and expansion coefficient from crystal-like to liquid-like values*" [2]. This is now accepted as the correct description of a glass.

Glass is obtained when the glass forming liquid is cooled at a sufficiently rapid rate to avoid crystallization at the freezing temperature. This process leads to the formation of a non-crystalline solid, in which the structural disorder of the liquid state is retained. Glasses are generally prepared by the melt quenching technique. Melt spinning, thermal evaporation, sputter deposition, reactive deposition, pulsed laser deposition, chemical vapour deposition, radiation and shock-wave induced amorphisation, anodic oxidation, pyrolysis, sol-gel route and spin coating are some other methods by which glasses have been prepared [3]. Since glassy materials possess only a short-range order, the nature of the chemical bond influences most of their properties. Based on the dominant bond type, glasses may be classified as metallic (*e.g.*, Zr-Cu, Ni-Nb), semiconducting (*e.g.*, Ge-Se, V_2O_5-P_2O_5), molecular (*e.g.*, C_2H_5OH), ionic {*e.g.*, KNO_3-$Ca(NO_3)_2$} and Van der Waals' (isopentane, ortho-terphenyl) glasses [4]. Glasses can be broadly divided into two categories, namely,

oxide glasses (*e.g.* vitreous silica, soda-lime glass, borosilicate glass), and non-oxide glasses (*e.g.* metallic glasses, halide glasses, chalcogenide glasses) [1]. Chalcogenide glasses contain chalcogen elements (group VI A of the Periodic Table) such as Sulphur, Selenium and Tellurium as their major constituent. Chalcogenide glasses have attracted a lot of attention due to their potential in technological applications such as xerography, photovoltaic solar cells, optical memory cores, switching devices, infrared sensors *etc*. [1,4,5].

1.1. Phenomenology of glass transition

The nature of the glass transition is very complex and not yet well understood. When any liquid is cooled, one of the following two events may occur. Either crystallization may take place at the melting point T_m of the corresponding crystal [path (a) in figure 1.1], or else, the liquid will become "super-cooled" for temperatures below T_m [path (b) in figure 1.1]. The viscosity of the super-cooled liquid increases with decreasing temperature and ultimately reaches a value, which is typical of a solid (~$10^{14.6}$ poise). At this stage, the super-cooled liquid is said to have reached the glassy state. The changes occurring in a liquid as it is cooled can be understood readily by monitoring the change in its volume as a function of temperature as illustrated in figure 1.1. The crystallization process is manifested by an abrupt change in volume at T_m, where as, glass formation is characterized by a gradual change in slope of the volume versus temperature curve [1,5]. The region over which the change of slope occurs is termed the glass transition region. Other thermodynamic variables such as entropy (S) and enthalpy (H) exhibit a similar behaviour with change in temperature.

According to the Ehrenfest scheme, the order of a phase transition is defined as *the order of the lowest derivative of the Gibbs free energy (G), which shows a*

discontinuity at the transition point [6]. For liquid-crystal transition at solidification (or melting) temperature T_m, the volume $V = \left(\frac{\partial G}{\partial P}\right)_T$ is discontinuous.

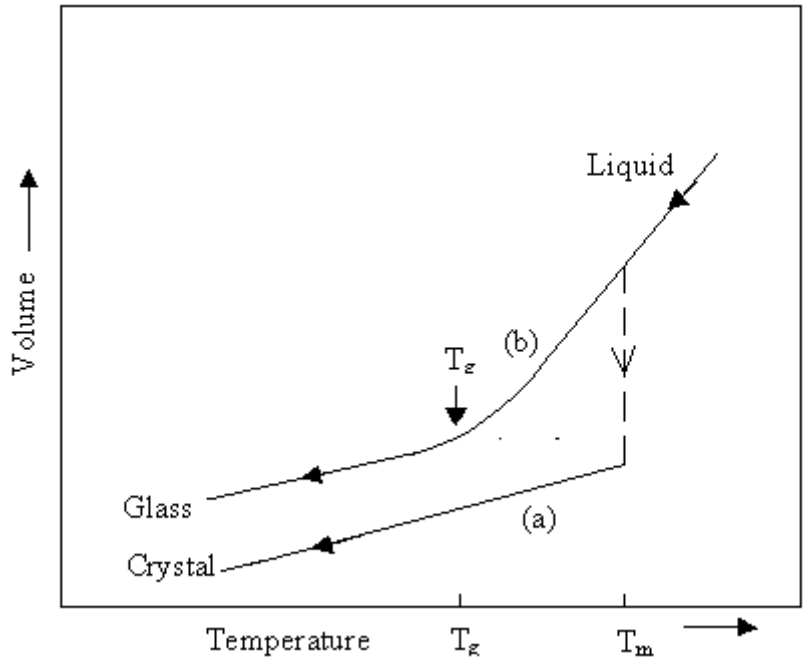

Figure 1.1: Volume change occurring in a liquid leading to the formation of a crystal [path (a)] or a glass [path (b)].

Hence liquid-crystal transition is a first order transition. But in liquid-glass transition, the thermodynamic variables such as V, S, and H are continuous and the quantities which are the second order derivative of the Gibbs free energy such as thermal expansion $\alpha_T = \frac{1}{V}\left(\frac{\partial^2 G}{\partial P \partial T}\right)$, compressibility $K_T = -\frac{1}{V}\left(\frac{\partial^2 G}{\partial P^2}\right)_T$ and heat capacity $C_P = -T\left(\frac{\partial^2 G}{\partial T^2}\right)_P$ are discontinuous. Hence the glass transition is a manifestation of a second order phase transition [5].

The glass transition temperature (T_g) depends on the rate of cooling of the super-cooled liquid [5]. The slower the rate of cooling, the larger is the region for

which the liquid may be super-cooled and hence lower is the T_g (figure 1.2). Thus, the glass transition temperature of a particular material is not an intrinsic property. Instead, it is dependent on the thermal history of the material. T_g is related to the cooling rate q by the relation,

$$q = q_o \exp\left[-\frac{1}{c}\left(\frac{1}{T_g} - \frac{1}{T_m}\right)\right] \qquad (1.1)$$

where c and q_o are constants [7]. The experimentally measured value of T_g is not unique. The value of T_g depends on the time scale of the experiment used to observe it.

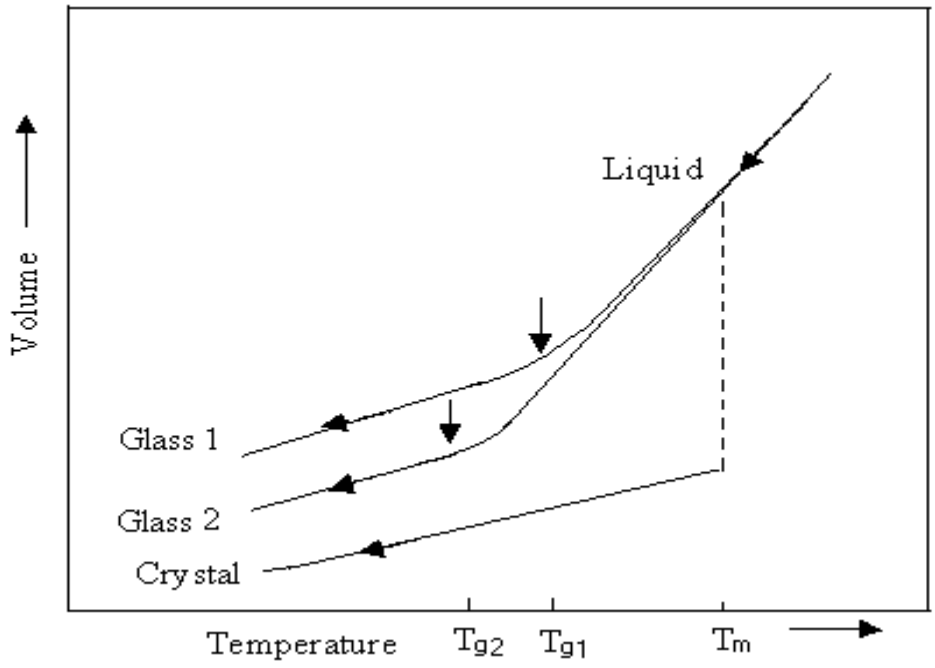

Figure 1.2: Variation in glass transition temperature (T_g) of a glass forming liquid with cooling rate. Glass 1 has been cooled (quenched) at a faster rate than Glass 2 ($T_{g2} < T_{g1}$).

T_g can also be defined in terms of the experimental time scale as, *the temperature at which the liquid attains a certain viscosity η, characteristic of a solid*

(typically, ~ $10^{14.6}$ poise). The viscosity of glass forming liquids changes very rapidly in the region of the glass transition temperature. A wide variety of theories of relaxation have been proposed to understand the glass transition, based on distinct microscopic models [8]. An empirical relation for viscosity at equilibrium is given by the Vogel-Fulcher-Tammann (VFT) equation,

$$\eta = \eta_0 \exp\left[\frac{A}{T - T_0}\right] \qquad (1.2)$$

where η_o, A and T_o are constants. Equation (1.2) is the most successful expression for describing $\eta(T)$ [9,10]. Glasses exhibit a disparate η versus T behaviour near T_g. When $\log(\eta)$ is plotted against T_g/T, this disparate nature exhibited by a host of glasses would be obvious. One such graph (often referred to as the Angell-plot) for selected glasses is depicted in figure 1.3. It can be seen from figure 1.3 that viscosity of certain glasses show Arrhenius type of behaviour, where as, others deviate from the Arrhenius behaviour by varying amounts. Angell [11] termed the glasses exhibiting Arrhenius type of behaviour as “strong” glasses. He used the term fragility to characterise and quantify the anomalous non-Arrhenius transport behaviour, which develops in most glass forming liquids as they approach the glass transition. Strong glasses show a strong resistance to structural degradation in the liquid state. Angell [11,12] proposed a modified form of equation 1.2, with which he accounted for the non-Arrhenius viscosity behaviour exhibited by “fragile” glass formers. The modified VFT equation can be expressed as,

$$\eta = \eta_0 \exp\left[\frac{DT_0}{T - T_0}\right] \qquad (1.3)$$

where η_0, D and T_0 are constants. Angell argued that the disparate non-Arrhenius curves shown in figure 1.3 could be generated using equation 1.3 by merely varying a single parameter D.

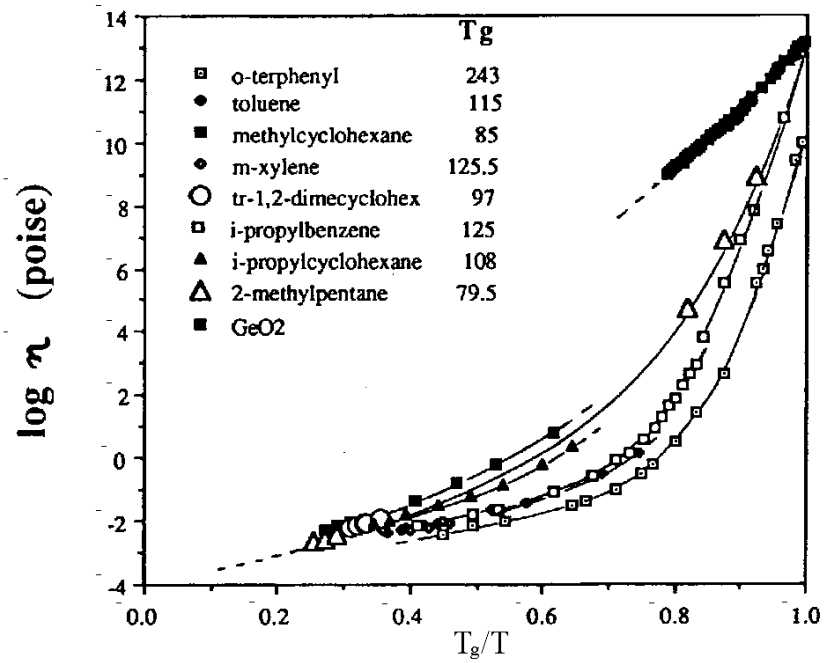

Figure 1.3: log (η) versus scaled temperature (T_g/T) plots of selected glasses near the glass transition temperature showing "strong" and"fragile" behaviour exhibited by glasses [12].

The heat capacity C_{Pg} of the glass is different from the heat capacity C_{Pl} of the super-cooled liquid. The excess heat capacity at the glass transition ΔC_p is then *the difference between the specific heat values of the glass and super-cooled liquid*. ΔC_p is the manifestation of the configuration entropy frozen in during glass formation. Angell [11] proposed that glasses exhibiting a small ΔC_p (at T_g) show a strong resistance to structural degradation in the liquid state. He termed such glasses as "strong". On the other hand, glasses exhibiting large ΔC_p (at T_g) were termed as "fragile". In our previous discussion on the viscosity of glasses, fragility was the term used to characterize the anomalous non-Arrhenius log (η) versus T plots obtained

for most glass forming liquids as they approach the glass transition [11]. How can one relate a glass exhibiting a small (minimum) ΔC_p with minimum fragility? To answer this question, let us consider the Adam-Gibbs equation [13],

$$\eta = \eta_o \exp\left(\frac{C}{TS_c}\right) \tag{1.4}$$

where η is the viscosity, and η_o and C are constants. The parameter S_c is the configurational entropy and is given by the expression,

$$S_c = \int_{T_k}^{T} \left(\frac{\Delta C_p}{T}\right) dT \tag{1.5}$$

where T_k is the Kauzmann temperature (*the temperature at which S_c extrapolates to zero* [14]). When ΔC_p is very small, S_c is almost temperature independent and the Adam-Gibbs equation could be approximated to the Arrhenius form of equation. This shows that the slope of the Arrhenius plot [i.e., ln(η) versus 1/T plot (figure 1.3)] is a minimum when ΔC_p is minimum. According to the above argument, minimum ΔC_p means minimum fragility. Hence ΔC_p can be taken as a measure of the "strong" or "fragile" nature of glasses. In order to differentiate between the fragility behaviour exhibited by the viscosity and the heat capacity jump the following notation has been used [15]. Glasses exhibiting non-Arrhenious viscosity behaviour and small heat capacity jump at T_g are referred to as kinetically fragile (KF) and thermodynamically fragile (TF) glasses respectively [16]. Under this scheme, a glass may be classified into one of the following four categories namely, TS-KS, TF-KF, TF-KS or TS-KF where TS and KS correspond to thermodynamically strong and kinetically strong

glasses. A brief list of glasses belonging to each of the four categories has been compiled [15].

1.2. Structure of glass

In order to obtain the atomic structure of a crystal, the structure of the unit cell needs to be solved as the first step. The complete structure of the crystal is then obtained by a periodical repetition of the position of the unit cell in space. On the other hand, the unit cell of an amorphous material is infinite in size! However, “order” manifests itself in amorphous materials through short-range and medium-range interactions. In order to obtain the complete structure of an amorphous solid, one has to go to the following steps:

1. Deducing the chemical structural units that constitute the short-range order (extending up to 5 Å units) and medium-range order (extending between 5 Å and 20 Å units) in amorphous solids. Extended X-ray absorption fine structure (EXAFS) is a probe particularly sensitive to short-range order, whereas, the radial distribution function (RDF), nuclear and electron spin resonance spectroscopy, Raman and infra-red spectroscopy are equally sensitive to short and medium-range interactions. High resolution electron microscopy (HREM), which probes specimen areas of ~ 30 × 30 $Å^2$ is potentially sensitive to medium-range order.
2. Estimating the amount and the extent of inhomogenities present in the form of phase separation (in melt-quenched chalcogenide glasses) and voids (in vapour deposited thin films) at much longer length scales. Transmission electron microscopy (TEM), optical microscopy and positron lifetime studies are some of the tools that are used to study these coarse structural features.

The structure of amorphous $GeSe_2$ has been investigated by Nemanich *et al* and Phillips. A symmetric ring structure containing six Ge and six Se atoms was

proposed by Nemanich *et al* [17] and the large "raft" structure containing twelve Ge and thirty Se atoms bordered by Se-Se "wrong" bonds was proposed by Phillips [18]. These models are illustrated in figure 1.4.

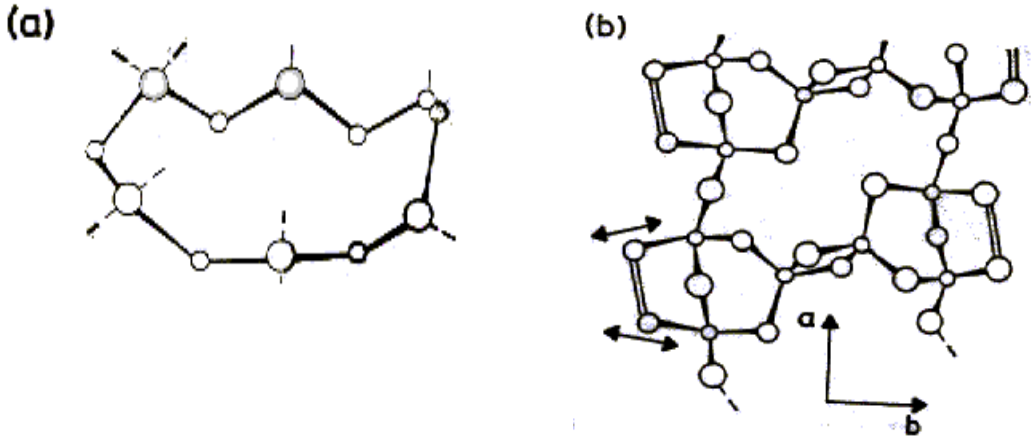

Figure 1.4: The proposed medium-range structures in a-$GeSe_2$ (a) The six membered ring and (b) the "raft" bordered by Se-Se wrong bonds. Bigger circles represent Se and smaller ones depict Ge atoms.

A significant development in structure modelling is the Monte Carlo simulations of the structure of As_xSe_{100-x} glasses ($0 < x < 50$) [19], in which the theoretical and experimental RDFs matched well.

1.2.1. Network models

Since there is no unique structure for an amorphous material, structural modelling is very useful in understanding its structure. Such a model is built using the knowledge of the local order in the system. The computed scattering properties (like RDF) of these models are fitted to those obtained from experiments. Such an exercise gives considerable additional insight into the structure, which cannot be otherwise obtained. Zachariasen's "continuous random network" (CRN) is the basis for all these models. Zachariasen [20] imposed some rules to be followed while building a model for a covalently bonded amorphous solid. These rules were intuitively based on the local similarity between crystalline and amorphous materials

and the lack of long-range order in amorphous solids. The ingenious CRN model proposed by him is applicable to the structure of oxide glasses with the general formulae A_mB_nO, where A is the network-forming cation, B is the network-modifying cation and m and n are non-integers. Several models have been proposed for the local structure of chalcogenide glasses, which are mainly modifications of the CRN model.

An arbitrary composition of a covalent binary alloy with the general formula $A_{100-x}B_x$, which obeys the 8-n rule (where n is the valency) can contain A-A, A-B and B-B bonds (the 8-n "octet" rule is strictly valid only for group IV-VII elements). Two models [21], namely, the "random covalent network" (RCN) and the "chemically ordered covalent network" (COCN) model describe the distribution of such bonds in these covalent binary alloys as the composition is varied.

In the RCN model, the bond distribution is determined only by the local co-ordinates Z_A and Z_B (=8-n) and the concentration x. Any effect leading to preferential ordering is neglected in this approach. The RCN model admits A-A, A-B and B-B bonds at all compositions except at x = 0 and x = 100. The COCN model on the other hand, assumes that heteronuclear A-B bonds are generally favoured. Thus, a completely (chemically) ordered phase occurs at a composition, $x_c = Z_A/(Z_A+Z_B)$. As_2Se_3, GeS_2 and $GeSe_2$ are some examples of this critical (or stoichiometric) composition at which the chemically ordered phase occurs in the respective alloys. In the COCN model (in contrast to the RCN model), only A-A and A-B bonds are allowed in A-rich ($0 < x < x_c$) glasses and conversely, B-B and A-B are the only allowed bonds in B-rich ($100 < x < x_c$) glasses. The bond-counting statistics for 3:2 (*e.g.* As_2Se_3) and 4:2 (*e.g.* $GeSe_2$) alloys according to RCN and COCN models are shown in figure 1.5. The analysis of the vibrational spectra of many chalcogenide

glasses shows that the COCN model is obeyed by most of the chalcogenide glasses. The COCN model predicts the occurrence of a chemical threshold at chalcogenide glass compositions at which an equivalent crystalline (stoichiometric) composition exists. It has been observed that the physical properties of chalcogenide glass compositions corresponding to the chemical threshold (stoichiometric) compositions exhibit observable features which are different from the ones exhibited by the rest of the glass compositions [22]. The COCN model has been used to interpret the composition dependence of several ternary chalcogenide glasses [23,24,25].

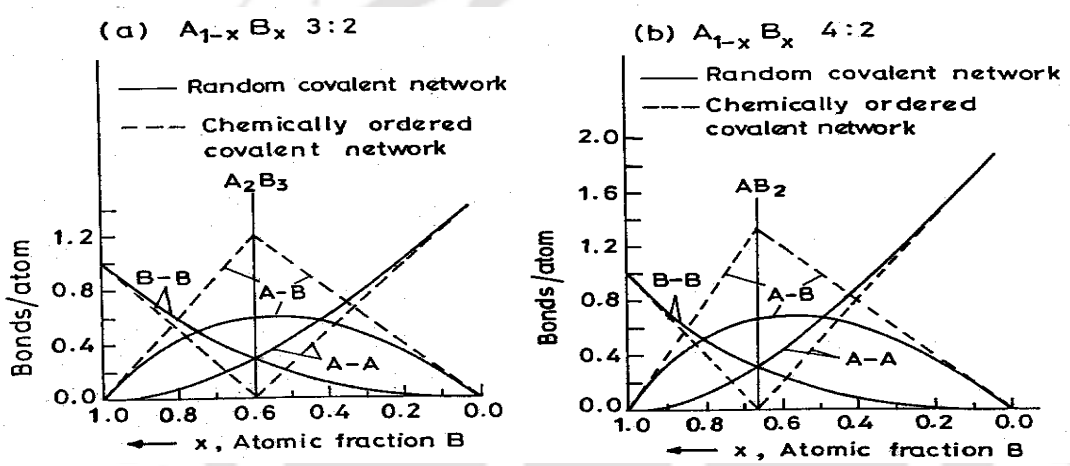

Figure 1.5: Bond counting statistics for (a) 3:2 networks and (b) 4:2 networks according to RCN and COCN models.

It has to be noted that network models are idealistic models in the sense that they generate the amorphous state in a dense state without taking into account structural defects such as voids *etc*. Thus network models are often inadequate in accounting for features observed in medium-range length scale and growth morphology.

1.2.2. Constraint counting models

Phillips proposed [18] a simple model for network glasses based on entirely topological considerations. This dynamical model is based upon the hypothesis that the glass structure is maximally optimised when the number of degrees of freedom

(N_d) for the atoms in a glassy network equals the number of constraints (N_{con}) in the network. Thorpe and co-workers [26,27,28,29] developed this model to predict the elastic behaviour of covalent glasses in terms of the average number of constraints in the system. This model treats the network glass such as A_xB_{100-x} as made up of elastically soft (or floppy) and elastically rigid regions (figure 1.6).

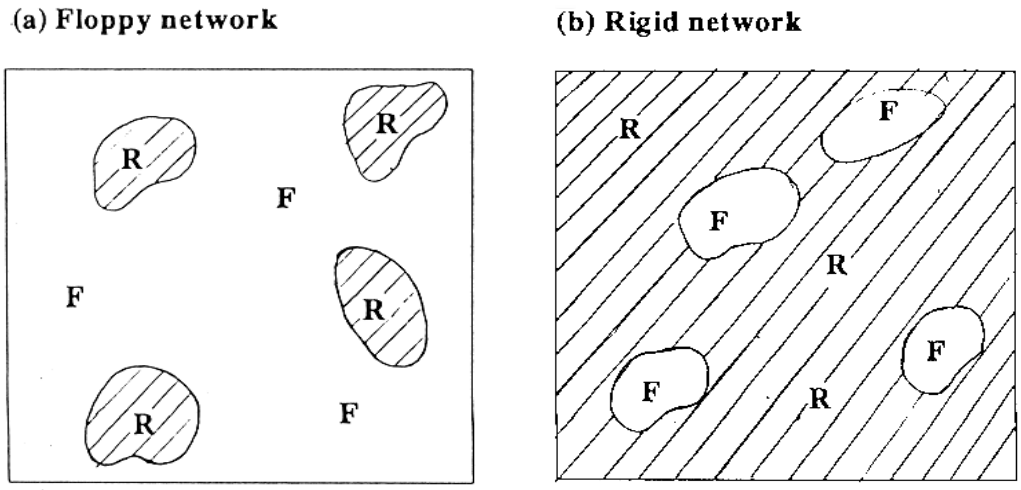

Figure 1.6: Rigid and Floppy regions in networks of a (a) the polymeric glass and (b) rigid amorphous solid.

In a polymeric glass for which $N_d > N_{con}$, there are more soft regions as compared to rigid regions. As N_{con} is increased, the rigid regions increase in size and when $N_d = N_{con}$, the network transforms into a completely rigid glassy structure. This transition phenomena is analogous to the "percolation" phenomena and the rigidity of the network is said to percolate when $N_d = N_{con}$. The under co-ordinated glasses ($N_d > N_{con}$) being soft can be elastically deformed easily by the application of a shearing force. Under such a situation, the system admits the displacement of groups of atoms without the provocation of restoring forces and hence has a number of "floppy" modes (*floppy modes or the zero-frequency modes are the number of deformation that are possible in which the bond lengths and bond angles are*

unchanged). The fraction of modes which are floppy in any glassy network is given by,

$$f = (N_d - N_{con})/N_d \quad (1.6)$$

The constraints (N_{con}) acting on a covalently bonded atom has two contributions i.e., from bond-lengths (bond stretching) and bond angles (bond bending). For an r co-ordinated atom, there are r/2 bond stretching constraints (since each bond is shared by two atoms) and (2r-3) bond bending constraints (where 2 denotes the two polar co-ordinates θ and Φ and 3 refers to the cartesian co-ordinates x, y, z). Since each atom has three degrees of freedom, N_d = 3. Adding up the bond-stretching and the bond bending constraints, the total number of constraints per atom becomes,

$$N_{con} = (r/2) + (2r-3) \quad (1.7)$$

Now considering a binary network glass with N atoms containing n_r bonds (where r = 2 and 4 for group VI and group IV atom, respectively), the fraction of modes which are floppy can be estimated from relation (1.6) as

$$f = 6 - \frac{5 < r >}{2} \quad (1.8)$$

where < r > is the average number of bonds per atom or the “mean co-ordination number”. When $N_d = N_{con}$, the floppy modes disappear since the glass undergoes a change to an elastically rigid structure. The mean co-ordination number < r > at which this transition occurs can be found by substituting f = 0 in relation (1.8), which gives < r > = 2.4. This value of < r > at which the transition occurs is termed as the “rigidity percolation threshold” or the “mechanical threshold”.

It should be noted that the rigidity percolation threshold predicted by this simple model depends only on the mean co-ordination number and is independent of the atomic composition and therefore the local structure. The < r > value at which the threshold occurs for a binary network glass such as A_xB_{100-x} is given by

$$\langle r \rangle = [(x)Z_A + (100-x)Z_B]/100 \qquad (1.9)$$

where Z_A and Z_B are the co-ordination numbers of the elements A and B (calculated using the 8-n rule), respectively, and x is the atomic weight percentage of element A in the glass. For the Ge_xSe_{100-x} glassy system, $Z_A = 4$ and $Z_B = 2$ and so the mean co-ordination number $< r >$ is 2.30, 2.40 and 2.50 for the glass compositions $Ge_{15}Se_{85}$, $Ge_{20}Se_{80}$ and $Ge_{25}Se_{75}$, respectively. Numerical simulations have been carried out [29,30] for both f and elastic moduli of a covalent network with 2-, 3- and 4-fold co-ordination elements. For calculating the $< r >$ dependence of the elastic constants, a 512-atom diamond lattice super-cell (with $< r > = 4.0$) was taken and its bonds were cut at random (thereby reducing $< r >$), taking care that no dangling bonds occur. With such a procedure it could be demonstrated (Figure 1.7) that the elastic modulus C_{11} (longitudinal elastic modulus) and f show a distinct change in slope between $< r > = 2.40$ and 2.45.

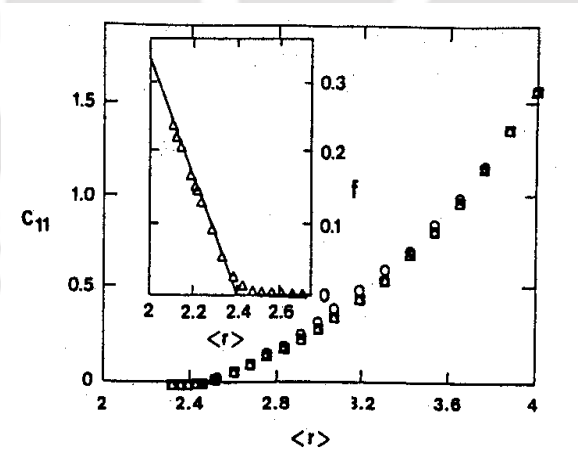

Figure 1.7: Variation of elastic modulus C_{11} with $< r >$ for a 512-atom diamond super cell. Inset shows the variation of f with <r> [29].

The excellent agreement of the results of this numerical simulation with the threshold value predicted by the percolation model stimulated experimental verification of the same in chalcogenide glasses. Notable among these is the report

on the elastic constants of Ge-As-Se glasses [31]. The authors measured the room temperature elastic moduli C_{11} and C_{44} at room temperature for two sets of Ge-As-Se glasses (one with low-As content and the other with high-As content). Their data plotted against the mean co-ordination number showed a change of slope at $< r > = 2.40$ in support of this model. An earlier report [32] on the elastic constants of Ge_xSe_{100-x} glasses showed a similar change of slope at $< r > = 2.40$ as predicted by this model. Apart from the elastic constants, experimental reports on a wide variety of physical properties of binary chalcogenide glasses indicated a threshold behaviour at $< r > = 2.40$ [33]. However, contrary to the earlier report [32] on the elastic constants of Ge_xSe_{100-x} glasses, Yun *et al* [34] and Duquesne *et al* [35] reported that the slope change in the elastic constants of Ge_xSe_{100-x} occurred at $<r> = 2.60$ and 2.70, respectively.

Tanaka [36] reported a similar departure in the threshold value in the $<r>$ dependence of various properties such as photo darkening, molar volume, X-ray diffraction, elastic constants *etc*. of Ge-As-S glasses and proposed an explanation for the observed shift. He pointed out that the interactions in chalcogenide glasses extend to medium-range scale and are not confined to short-range scales as originally considered by Phillips and Thorpe. This means that the number of constraints has been overestimated in determining the rigidity percolation threshold at $<r> = 2.40$. He argued that chalcogenide glasses are known to posses a layered structure and so medium-range interactions have to be considered in relation (1.7). He also showed that for an atom in a planar cluster extending in the xy-plane, the number of constraints reduces to

$$N_{con} = (r/2) + (r-1) \qquad (1.10)$$

Where the number of bond-bending constraints per atom is (r-1). If such a cluster is laid in 3-dimensional space, each atom must have three independent degrees of freedom for stable existence i.e. $N_d = 3$. Therefore, the constraints balancing equation $N_d = N_{con}$ becomes,

$$3 = r/2 + (r-1) \qquad (1.11)$$

From equation (1.11) the <r> value at which the rigidity percolates is 2.67. This means that a two-dimensional glass (or a glass possessing a layered structure) appears to be stably fixed in a three-dimensional space, if the mean co-ordination number of glassy network is 2.67. New experimental results and old data from published work have been reanalyzed [36] in the light of the above arguments.

Recent studies on binary Ge_xSe_{1-x} glasses [37], As_xSe_{1-x} glasses [38] and ternary $As_xGe_xSe_{1-2x}$ glasses [39] suggest the existence of an intermediate phase which is in between the floppy and rigid phases. This intermediate phase occurs for $< r > > 2.40$ for Ge-Se and ternary glasses, and for $<r> < 2.40$ for binary As-Se glasses [38]. This observation shows that this intermediate phase depends extensively on the local and medium-range structures present in glasses. The exotic intermediate phase possesses low molar volume, excellent glass forming tendency and good photomelting properties [37]. These optimally rigid phases are stress-free structures.

Unfortunately, contributions to structural data from intermediate and medium-range order cannot be easily distinguished from short-range order. Though HREM is claimed [40] to be specifically sensitive to medium range order, there are not many reports on HREM studies on chalcogenide glasses relevant to this problem, possibly due to experimental difficulties.

1.2.3. Diffraction pattern of covalent glasses

In the diffraction pattern of covalent glasses, there is a common feature widely observed which is regarded as a signature of the medium-range order (MRO) called “first sharp diffraction peak” (FSDP) or “pre-peak” [41,42]. The FSDP occurs at a value of scattering vector $\vec{Q} = \frac{4\pi \sin\theta}{\lambda}$ in the range 1-2 Å^{-1} in the structure factor $S(\vec{Q})$ of covalent network glasses [43,44]. The FSDP is observed in a wide variety of chalcogenide and oxide glasses *e.g.* As_2S_3, As_2Se_3, $GeSe_2$, GeS_2, SiO_2, Li_2O-Na_2O-SiO_2, but not in pure chalcogens like a-Se, a-Ge and a-Si. FSDP exhibits anomalous behaviour as a function of temperature, pressure and composition. FSDP intensity increases with increasing temperature as reported in As_2S_3, As_2Se_3 [45] and GeS_2 glasses [46] and decreases with increasing pressure [47]. The intensity of FSDP decreases markedly upon the addition of modifiers atoms in chalcogenide glasses *e.g.* GeC_2, As_2C_3 (where C = chalcogen) [48]. In Ge_xSe_{100-x} glasses, FSDP intensity is maximum for the $Ge_{33.3}Se_{66.7}$ glass composition [49] which corresponds to <r> = 2.67. A number of suggestions have been put forward to understand the structural origin of the FSDP [50,51]. Elliott proposed [41,42] that the FSDP is a pre-peak in the concentration-concentration structure factor, arising from the chemical ordering of interstitial voids around cation-centred clusters in the structure. A second pre-peak has also been generally observed in $S(\vec{Q})$ of network glasses at around in $\vec{Q}$~2.91 Å^{-1} for the case of amorphous SiO_2 [43]. This second pre-peak also behaves in an anomalous fashion. This “second pre-peak is termed as the “second sharp diffraction peak” (SSDP). The behaviour and structural origin of SSDP can be understood in exactly the same manner as the FSDP, namely, as a pre-peak originating from the chemical ordering of voids in the structure [52]. Elliott’s intuitive model has been

successful in explaining the temperature dependence of the intensity of FSDP and SSDP of As_2Se_3 glass [53] and the pressure dependence of intensity of FSDP of $GeSe_2$ glass [47].

1.3. Electronic Structure of glass

1.3.1. Energy band models

The transparency of silica (window glass) was the first indication of amorphous materials possessing a band structure without having long-range periodic ordering of atoms. The Bloch equations could satisfactorily explain the behaviour of an electron in a periodic structure. Mott [54,55] made the first effort to extend the band theory to amorphous materials. His suggestions are based on Anderson's localization principle [56]. Anderson suggested that the spatial fluctuations in the potential caused by the configurational disorder in amorphous material could lead to the formation of localized states which do not occupy all the energy states in the band, but form a tail above and below the band. An electron in a localized state will not diffuse at zero temperature to other allowed states with corresponding potential fluctuations. Another suggestion by Mott is the existence of a critical density of electronic states, above which the states in amorphous solid become extended. The mobility of electrons in the extended regions has a finite value, whereas, it is negligible in the localized region. The mobility edge is the critical energy below which the mobility drops sharply. The mobility edges near the "valence" and "conduction" bands have the same significance as the band edges in crystalline semiconductors.

The Cohen-Fritzsche-Ovshinsky (CFO) model [57] is a modification of Mott's model. This model assumes that (i) the nature of the band tails in amorphous materials depends on the existence of disorder (deviation from the perfect periodicity), (ii) the mobility edges in between the localized and extended states are

sharp, and (iii) each atom is expected to satisfy its valence requirements. The CFO model was proposed to understand the electrical switching characteristics of the multicomponent glasses. This model therefore ensures self-compensation and pins the Fermi level close to the middle of the gap. The extent of localization suggested by this model has turned out to be an overestimate.

The Mott and Davis model [58] proposes narrow tails of localized states extending to a few tens of eV into the forbidden gap. This model suggests the existence of a band of compensated levels near the middle of the gap, originating from the defects in the random network such as dangling bonds, vacancies, *etc*. The centre of the band may be split into donor and acceptor bands, which will also pin the Fermi level. Recent experiments on luminescence, photoconductivity and drift mobility of amorphous semiconductors indicate the existence of localized states located at well defined energy levels in the gap. The true gap in the Mott-Davis model is E_A-E_B.

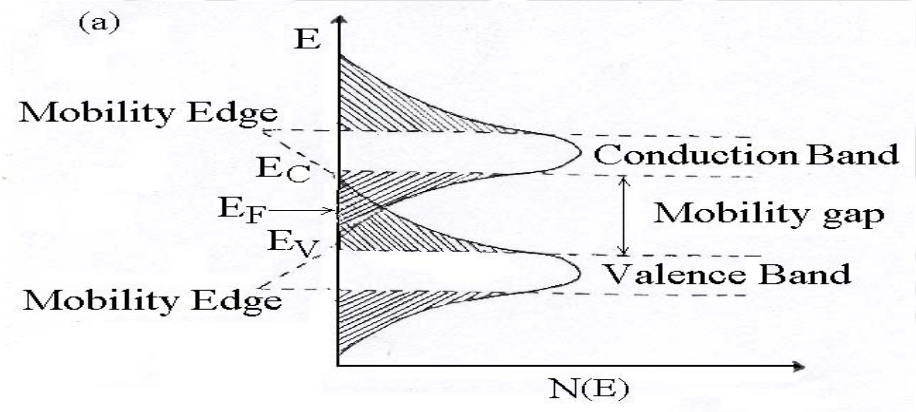

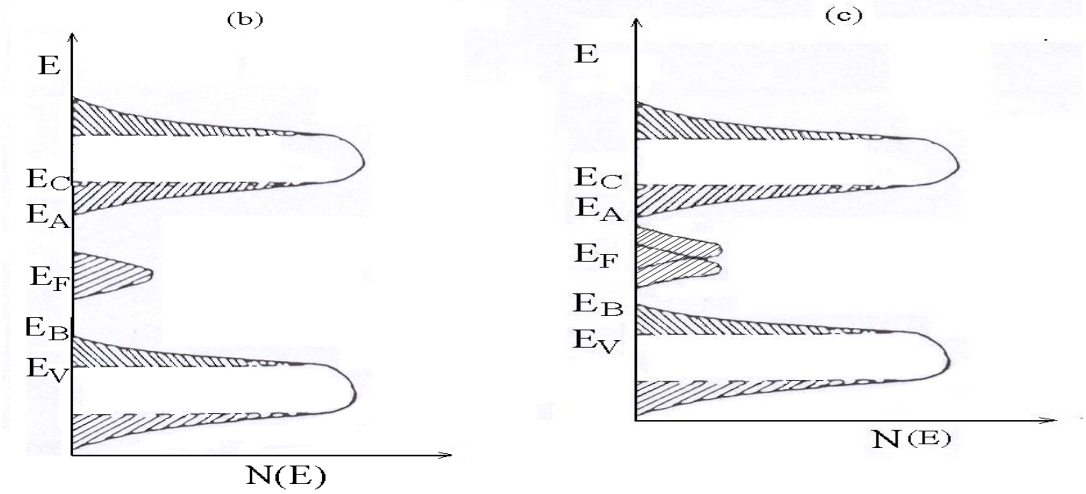

Figure. 1.8: Schematic view of the electronic structure of amorphous solids as proposed by the (a) C F O model and (b) Mott-Davis band model (C) Marshall-Owen model.

Marshall and Owen [59] modified the Mott-Davis model. Their main modification was the splitting of the midgap band into donor and acceptor levels with some overlap. Figure 1.8 shows a schematic view of the electronic structure of amorphous solids as expressed by the CFO and Mott-Davis and Marshall-Owen band models.

1.3.2. Models based on charged defect states in glass

Based on Anderson's hypothesis [60] that *"negative effect correlation energy is a general property of localized states in disordered system*", Street and Mott proposed [61] that chalcogenide glasses contain about 10^{18}- 10^{19} cm^{-3} "dangling" bonds. Dangling bonds are point defect states, which do not satisfy the normal co-ordination owing to local topological constraints. For this reason, the Street-Mott model is also known as Dangling Bond (DB) model. Although this model was successful in explaining many experimental results, it could not explain (i) the origin of high densities of dangling bonds in chalcogenide glasses, and (ii) the existence of large negative correlation energy in chalcogenide glasses.

Kastner proposed a simple model [62] for the electronic states in chalcogenide glasses based on the chemical bonding between atoms. This model considers the electronic states of the solid to be a broadened superposition of the molecular states of the constituent bonds. When any two atoms are close enough for the bonding electrons to interact, the energies of their states get shifted by the interaction. This gives rise to bonding (σ) states with reduced energy and an equal number of antibonding (σ^*) states with increased energy. States, which are unshifted in energy are called non-bonding states. Since the energy between the *s* and *p* states is usually of the same order as the bonding energy, it is possible to promote one of the paired *s* electrons to the *p* states and thereby form two covalent bonds. Group IV elements such as Ge and Si have hybridised sp^3 orbitals, which can conveniently split into four *s*-*p* bonds. Thus, in tetrahedral semiconductors, the bonding band forms the valence band and the antibonding band forms the conduction band. The presence of three unpaired *p* electrons in group V elements doesn't energetically favour such bonding. In group VI elements such as Se and Te, the *s* states lie well below the *p* states and need not be considered. Since only two of the three *p* states can be utilized for bonding, one normally finds chalcogen atoms in two-fold co-ordination. This leaves one non-bonding electron pair. In a solid, these unshared or lone-pair (LP) electrons form a band near the original *p*-state energy. The σ and σ* bands are split symmetrically with respect to this reference energy. Both σ and LP bands are occupied. Thus the bonding band is no longer the valence band. This role is played by the LP band. Figure 1.9 illustrates the bonding in Ge and Se. This chemical approach is valid for chalcogenide glasses. Kastner also predicted that in a chalcogenide alloy, (a) the LP states cease to exist as the valence band, if the concentration of the chalcogenide atoms are reduced below a critical value, and

(b) an Anderson transition (*transition from extended to localized states*) occurs at this critical value.

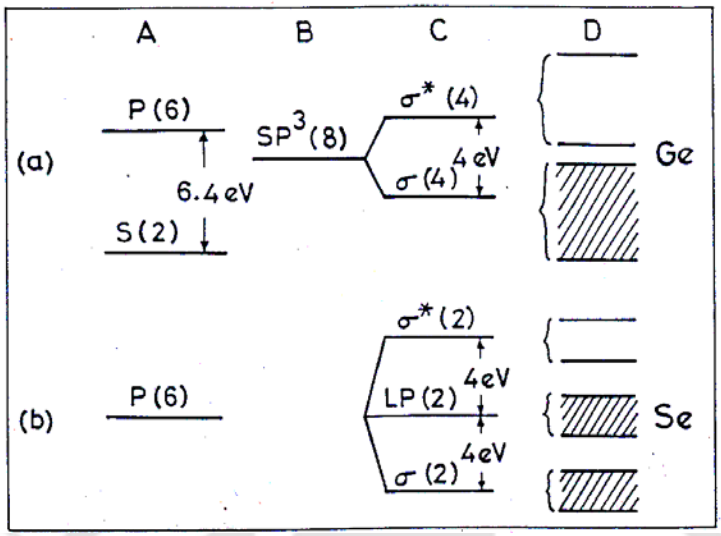

Figure 1.9: Band structure of (a) Ge and (b) Se as proposed by Kastner [62].

Subsequent development of Kastner's chemical approach paved way to the Valence Alternation Model [63]. These developments can be summerised as follows: Dangling bonds have negligible density in chalcogenide glasses because it requires a large amount of energy to create them. But the three-fold co-ordinated chalcogens have relatively low energy defects. When a bond is broken in these glasses, it either breaks symmetrically or asymmetrically. An asymmetrically broken bond leaves an atom with no electron while giving it's both bonding electrons to the other. So one atom has two lone-pairs and is negatively charged, while the other has empty *p*-orbital and is positively charged. This positively charged dangling bond converts a neighbour into a C_3^+ center, thereby forming a full bond by lowering both lone-pair electrons of the neighbour into the bonding orbital. As the number of bonds is conserved, no antibonding electron arises. But the negatively charged centre C_1^- has an extra electron, which raises its energy by an amount equal to the correlation energy (U_{eff}) because of the coulomb interaction. As the two defect states with co-

ordination of three (C_3^+) and one (C_1^-) are formed instead of the normal two-fold co-ordination state (C_2^0), these are called Valence Alternation Pairs (VAP). On the basis of this model, the concept of negative correlation energy in chalcogenide glasses could be well understood. This model also explains successfully the origin of high density of defects in chalcogenide glasses which was not possible using the Street-Mott model.

Recently, Kolobov [64] addressed the question of the origin of *p*-type conduction in chalcogenide glasses. He considered the thermal excitation of charge defect states C_3^+ and C_1^-. The positive defect state C_3^+ cannot be excited directly because the non-bonding states are removed during the formation of the three-fold co-ordination state. So, when one of the neighbours (say, C_2^0 state) of this positively charged defect state gets excited, an electron-hole pair is generated. The electron could be trapped by the C_3^+ state, thereby transforming it into the C_3^0 (unstable) state, which subsequently decays into the C_1^0 state. But the hole generated by this process remains free and mobile in the valence band and contributes to *p*-type conduction type in chalcogenide glasses. But when the negatively charged defect state C_1^- is excited, an electron and C_1^0 state are formed. In the singly co-ordinated defect state (C_1^0), no structural reconstruction takes place in the defect site. So the electron recombines with the C_1^0 state to recreate the C_1^- state originally present before the excitation. Thus, during the entire thermal excitation process, the life-time of the holes generated from the thermally excited positively charged effect states is longer compared to the life-time of the electrons generated by the negatively charged defect states. This results in the observed *p*-type electrical conduction in chalcogenide glasses.

1.4. d.c. electrical properties of chalcogenide glasses

d. c. electrical conductivity of an amorphous semiconductor can be understood from the Davis and Mott model. Depending on the temperature range, three conduction mechanisms are possible in amorphous semiconductors.

Case (i): At high temperatures, an electron that has been excited to the extended states behaves like a conduction electron. This results in the "band transfer mechanism". The electron motion is occasionally interrupted by self-trapping and release events because of the localized states just below it. Thus its overall mobility is reduced [65]. However, the maximum effect on conductivity comes from the density of charge carriers, which is proportional to $\exp[-(E_C-E_F)/k_BT$, where E_C is the mobility edge on the conduction band side. The electrical conductivity σ in this region has the form,

$$\sigma \cong \sigma_o \exp\left(\left[-\frac{E_C - E_F}{2k_BT}\right]\right) \qquad (1.12)$$

where σ_0 is of the order of 10^2-10^4 $ohm^{-1}.cm^{-1}$. Thus the activation energy for conduction is given by (E_C-E_F).

Case (ii): At intermediate temperatures, conduction occurs by hopping of carriers excited from the valence band edge into the localized tail states within the gap. This type of conductivity has the form,

$$\sigma \cong \sigma_o \exp\left(\left[-\frac{(E_b - E_F) + \Delta W_H}{k_BT}\right]\right) \qquad (1.13)$$

where E_b is the energy of the valence band tail and ΔW_H is the activation energy for hopping conduction.

Case (iii): At low temperatures, variable-range hopping (VRH) in a band of localized states at the Fermi energy has been observed. The term variable is used to denote that the hopping range of the electron (R) varies with temperature. Mott showed that $R \approx [\alpha k_B T N(E_F)]^{1/4}$, where $N(E_F)$ is the density of states near the Fermi energy E_F and α is the inverse localization length. VRH conduction is given by [68],

$$\sigma \sim \exp (A/T^{1/4}) \qquad (1.14)$$

where A is a constant. The electrical conductivity in this case is thermally activated. Amorphous As_2Te_3 films deposited by sputtering method showed VRH conduction [69]. Variable range hopping between (paramagnetic) defect states lying at E_F at mid gap was responsible for the observed conduction in these films. VRH conduction has also been reported in many chalcogenide glass thin films like Sb-Bi-Te, Bi-S, Bi-Se, Cd-In-S [70,71,72] and also in bulk Pb-In-Se glasses [73]. But VRH conduction is not observed in many bulk chalcogenide glasses or well-annealed thin films. This is a consequence of the negative effective correlation energy associated with the co-ordination defects, which results in the formation of spin-paired, charge defects lying away from E_F and for which the electron-phonon coupling is so large that the hopping rate becomes slow [74].

The conduction mechanism in oxide glasses could be explained in terms of the small polaron hopping conduction mechanism [1]. A localized charge carrier such as an electron is likely to distort its surroundings. Such a distortion may extend physically over a few atoms. The distortion tends to lower the energy of the carrier. The resulting attraction will cause the carrier to be self-trapped. Under this assumption, the motion of a localized electron may be imagined to be the motion of the electron plus its distorted surrounding. The name “small polaron” has been given

to this entity consisting of the electron plus its distorted surrounding. The small polaron has a larger effective mass than that of an electron in extended states. Taking the case of vanadium pentoxide glasses (*e.g.* V_2O_5-TeO_2 [75], V_2O_5-P_2O_5 [76], small polaron hopping conduction occurs when an electron transfers from a V^{4+} site to V^{5+} site [77]. Mott and Davis proposed that for the small polaron process, the electrical conductivity is given by the relation [66,67],

$$\sigma T = \sigma_o \exp\left(-\frac{W}{k_B T}\right) \tag{1.15}$$

where σ_o is constant and W is an activation energy given by

$$W = W_H + \frac{1}{2} W_D \tag{1.16}$$

where W_D is the distortion energy and W_H is the hopping energy. Figure 1.10 schematically shows the various conduction processes.

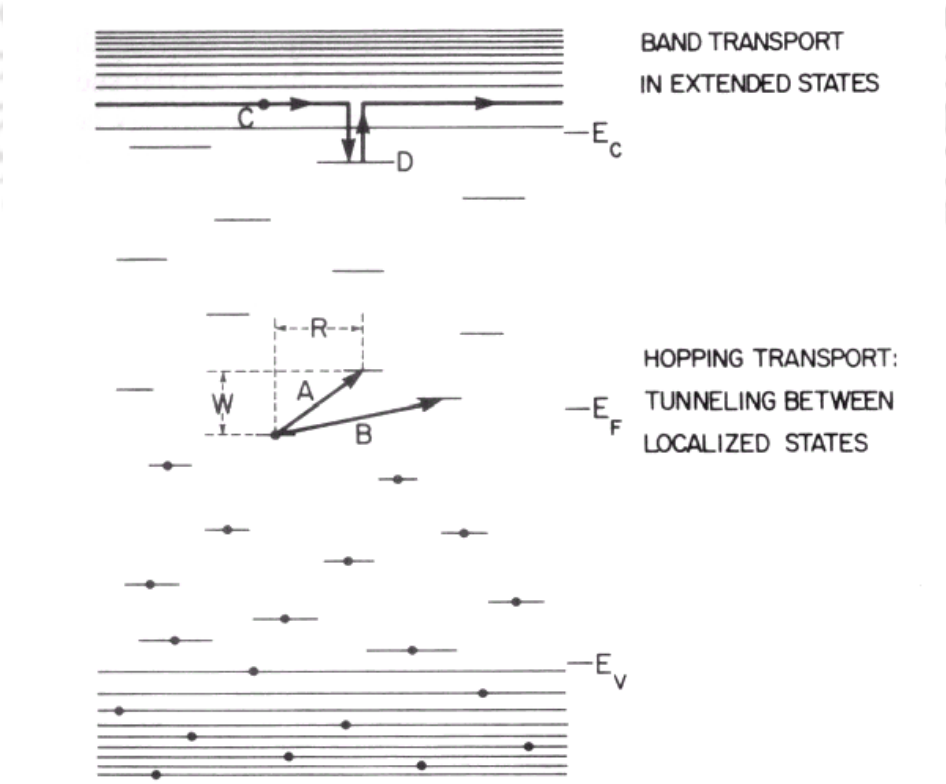

Figure 1.10: Electrical conduction processes in amorphous semiconductors [1].

1.5. Thermoelectric power of glasses

Thermoelectric power also known as Seebeck coefficient is given by the expression, $Q = -\frac{\Delta V}{\Delta T}$, where ΔV is the thermo e.m.f. developed due to the temperature difference ΔT across the surface of a material. Conventionally, hot end of a disc shaped sample is connected to the positive terminal and the cold end to the negative terminal of a high input impedance voltmeter (Electrometer). Due to the temperature gradient developed across the surfaces, majority charge carrier moves from the hot surface towards the cold surface. If the sample is *n*-type, the majority charge carrier is the electron, which moves from the hot surface and accumulates at the cold surface. Thereby, cold end of the sample is at higher negative potential than the lower surface. Consequently, electrometer shows positive e.m.f. resulting a negative Seebeck coefficient. On the other hand, if the sample is *p*-type, then the majority charge carrier (hole) accumulates at the cold end resulting in a negative e.m.f. Hence, the Seebeck coefficient is positive which indicates *p*-type conduction.

For the case of band conduction in extended states, the variation of Seebeck coefficient with temperature is given by the relation [5],

$$Q = \pm\frac{k_B}{e}\left(\frac{\Delta E_s}{k_B T} + A\right) \qquad (1.18)$$

where the positive and negative signs denote *p*-type and *n*-type conduction respectively, e is the electronic charge, k_B is the Boltzmann constant, T the absolute temperature, ΔE_s is the activation energy for thermoelectric power and A is a constant which is dependent on the mechanism of the electrical transport. A = 1, for the case of amorphous semiconductors exhibiting conduction in extended states.

1.6. Hall effect in glasses

When a magnetic field is applied perpendicular to a semiconductor carrying current, a voltage is developed across the specimen in the direction perpendicular to both the current and magnetic field. This phenomenon is known as Hall effect. If H_H is the magnetic field applied perpendicular to the direction of flow of current density J_σ, then the electric field F_H developed perpendicular to H_H and the current density J_σ in the electron-conducting solids are related to a parameter called Hall coefficient R_H [78] given by the relation [79],

$$R_H = \frac{F_H}{J_\sigma H_H} = \frac{1}{ne} \quad \text{or} \quad \frac{1}{pe} \tag{1.19}$$

where n and p are the electron and hole charge density. R_H enables one to determine the charge carrier sign in the case of unipolar conduction (or majority charge carrier type in the case of a semiconductor). The equation

$$\mu_H = |R_H|\sigma = |r_H|\mu \tag{1.20}$$

gives the hall mobility μ_H of the semiconductor. The mobility in non-crystalline semiconductors is much smaller and the mean free path is in the order of the interatomic distances. So the scattering mechanism cannot be predicted using conventional models. *p*-type chalcogenide glasses exhibit a negative Hall coefficient, which is surprising in view of the positive sign of the Seebeck coefficient Q. This contradictory result is viewed as a unique anomaly of amorphous semiconductors [80,81]. However, in the case of $TlAsTe_2$ glass, R_H showed the same sign as Q [81]. An explanation for the observed differences in the sign of R_H and Q in chalcogenide glasses was given by Friedman [82]. For the case of band conduction, Friedman [82] derived the relationship,

$$\mu_H = \frac{4\pi\pi e^2}{3\hbar} a^2 J N_{eff} \left(\frac{\bar{z}}{z}\right) \quad (1.21)$$

where J is the energy of the overlap integral between adjacent bonding centers, N_{eff} is the density of states in the region E_c or E_v, $\bar{z}$ is the co-ordination number and z is the number of interacting centers. The relationship between mobilities μ and μ_H is expressed as,

$$\frac{\mu_H}{\mu} = \frac{kT}{J} \quad (1.22)$$

substituting J ≈ 1 eV gives $\mu_H \sim 10^{-1} cm^2 V^{-1} S^{-1}$. This means that μ_H in amorphous semiconductor is certainly not greater than one-tenth of the mobility in band states. According to Friedman's theory, a configuration of three interacting centers leads to a negative sign for R_H, even if the conduction is due to holes. This provided the first explanation for the anomaly between the Seebeck and Hall effects observed in chalcogenide glasses. A similar relation for the Hall mobility in the polaron hopping mechanism has been formulated by Holstein [83].

The temperature independence of the Hall mobility expected from equation 1.22 and the value of $\sim 10^{-1}$ $cm^2V^{-1}S^{-1}$ have been confirmed in glasses and melts of As-Se-Te [81], Ge-As-Te [84] and Tl-As-Se-Te [81,85] by experimental measurements.

1.7. Optical properties of glasses

Amorphous solids are optically isotropic. However, macroscopic inhomogenities result in small variations in the refractive index of these solids. In amorphous materials, the k-vector conservation in photon-phonon interactions is no longer valid (since these materials do not have a well defined reciprocal space). So all phonons can take part in first order interaction with light. Hence, the entire phonon

density of states appear in the infrared and Raman spectra which result in a broad band instead of the discrete line spectrum observed in crystals. Amorphous materials have a forbidden gap and hence an absorption edge. In chalcogenide glasses, the density of states is determined by the topological disorder, ring statistics of the network and nature of the molecular units [86].

The absorption edge in amorphous semiconductors can be generally separated into three regions [87] on the basis of the value of the absorption coefficient (α). These three regions of the absorption curve (figure 1.11) are referred to as the high absorption (A) region ($\alpha \geq 10^4$ cm^{-1}), the exponential (B) region ($1 \leq \alpha \leq 10^4$ cm^{-1}) and the tail (C) region ($\alpha \leq 1$ cm^{-1}), respectively. The first two regions arise due to transitions within a fully co-ordinated system perturbed by defects, while the third region arises due to transitions involving defect states directly.

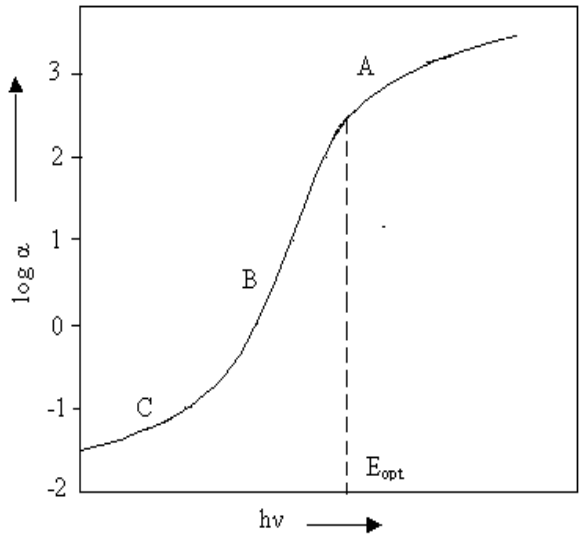

Figure 1.11: Regions A, B, C of a typical absorption curve of an amorphous semiconductor.

In the high absorption (A) region, the absorption coefficient has the following frequency dependence:

$$h\nu\alpha(\nu) = B(h\nu - E_0)^r \qquad (1.23)$$

where ν is the frequency, B is a constant, E_0 is the optical band gap and r is a constant. r = 2, if both conduction as well as valence band edges are parabolic. Exception to this quadratic frequency dependence is observed in *a*-Se and some multicomponent glasses. From the above expression, an empirical definition for the optical band gap can be made. In amorphous materials, all pairs of extended states with energy difference $h\nu$ can contribute to optical absorption. From a plot of $[h\nu\alpha(\nu)]^{1/2}$ versus $h\nu$, E_{opt} can be obtained as the energy at which $[h\nu\alpha(\nu)]^{1/2} \rightarrow 0$ [88].

In the intermediate absorption (B) region, $\alpha(\nu)$ assumes the form,

$$\alpha(h\nu) = C \exp\left(\frac{h\nu}{E_e}\right) \qquad (1.24)$$

where E_e is the energy characterizing the slope and C is a constant. E_e is independent of temperature at low temperatures and has the value of about 0.05 eV to 0.08 eV for most chalcogenide glasses. The origin of this exponential tail is not clear. Disorder induced potential fluctuations [89,90] and strong electron-phonon interactions [91] have been suggested as possible reasons for the exponential absorption.

In the weak absorption tail (C) region, the strength and the shape of the absorption tail are found to depend on the preparation, purity and the thermal history of the material.

1.8. Other physical properties of glasses

1.8.1. Density and Molar volume

Density of a substance is defined as the mass per unit volume. Density is a bond sensitive property [3,92]. The dependence of density upon temperature is through the volume thermal expansion coefficient. Since glasses may, in general, be

regarded as solutions, a more useful property is the molar volume V, defined as the volume of one-gram mole of glass. Then, one can proceed to define partial molar volumes of the structural units constituting the glass. The partial molar volume v_i of a species i in a solution is defined [1] by,

$$v_i = \left(\frac{\partial V}{\partial n_i}\right)_{n_j, T, P} \tag{1.25}$$

where $V = n_i v_i + n_j v_j$, and n_i, n_j are the molar fractions of the species i and j. In essence, the total molar volume is treated as an extensive property in terms of the partial molar volumes of individual species or structural groups. The partial molar volume information can be extracted from the density data of glasses where the constituents have been systematically varied. The molar volume V_m can be determined from the relation,

$$V_m = M/\rho \tag{1.26}$$

where M is the mass of one mole of glass and ρ is the density. V_m can also be expressed [93] by an additive relation of the form,

$$V_m = \Sigma n_i V_i \tag{1.27}$$

where n_i is the number per mole of the structural unit and V_i is its volume.

The dependence of density upon cooling rate, temperature and composition [94] can be studied from the volume variation of a super-cooled liquid as it transforms into glass. Except for a few anomalous cases, such as silica, a fast-cooled glass generally has a higher volume, and hence a lower density, relative to a slow-cooled glass of the same composition. The effect of temperature variation on the density of a glass is usually small in the glassy state [95].

1.8.2. Microhardness

Interest in the microhardness of materials is at least two-fold. There is a general interest in material properties as such and secondly, there is a desire to obtain an understanding of the microhardness based on the models, which involve structural parameters on an atomic scale [96]. Although the physics of hardness is still not understood completely, one can discuss hardness in relation to elastic moduli and bond strength parameters using elastic moduli to constrain the effective bond strength [96]. Hardness of any material is the result of a complex process of deformation during indentation, the nature of which is even more cryptic in the case of glasses because of our limited knowledge of the glass structure. During the process of indentation the material undergoes both compression and shear resulting in the observed deformation, which comprises of elastic deformation, flow and densification [97,98]. The bond strength of a certain compound determines the ratio of recoverable and irreversible deformation. High bond strength causes high elastic moduli preventing breakage, while low bond strength results in a higher percentage of bond breaking concomitant irreversible, plastic flow. This concept led Yamane and Mackenzie [96] to estimate the Vickers hardness number (VHN) from the square root of the bond strength, the bulk modulus B and the shear modulus G,

$$VHN = C\sqrt{\alpha BG} \qquad (1.28)$$

where C is a proportionality constant and α is the bond strength factor [*Vickers Hardness number (VHN), which is obtained by indentation of a specimen with a square pyramidal diamond tip, is a measure of the microhardness*]. From equation (1.28), it is evident that the VHN decreases as the elastic moduli of the glass decreases. This dependence of VHN on elastic moduli of glasses has been observed in many glasses [97,99].

Microhardness of multi-component chalcogenide glasses follow an empirical relationship with the mean co-ordination number <r> [100,101,102]. Microharndess of ternary chalcogenide glasses have been interpreted in terms of the COCN model [24]. Interpretation based on the COCN model argue that microhardness shows inflextion points at the stochiometric (critical) compositions. It has also been found that the microhardness is related to the dilatometric softening point T_d, which is usually obtained from thermal expansion curves. T_d is defined [99] *as the temperature at which the glass sample reaches a maximum length in a length versus temperature curve when heated*. Decrease in microhardness with a decrease in softening temperature has been observed in many glasses [103].

1.9. Majority charge carrier reversal (MCCR) phenomenon in chalcogenide glasses

Chalcogenide glasses are *p*-type semiconductors with the Fermi energy level pinned near the valence band [63]. The origin of the *p*-type conductivity in these glasses could be understood using Kolobov's model [64]. Shattering the myth that the Fermi energy level in these glasses could not be unpinned, Toghe *et al* demonstrated that *n*-type glasses could be obtained when sufficient amount of Bismuth (Bi) [105,106] or Lead (Pb) [107] is added in bulk Ge-C (C = S, Se, Te) glasses. Since Bi or Pb bring about the majority charge carrier reversal (MCCR) in these glasses, they are referred to as Bi modified and Pb modified chalcogenide glasses respectively.

1.9.1. Bi modified Ge-C (C = S, Se, Te) glasses

In order to understand the change of conduction mechanism in Bi-Ge-Se glasses, two models have been proposed. One of them assumes that Bi is incorporated homogeneously in the glass in the form of a charged state. This results

in the alteration of the relative proportions of oppositely charged defect states by the law of mass action, thereby allowing the Fermi level to become unpinned. There have been several suggestions in the literature regarding the sign and co-ordination of the Bi charged defect state, such as positively charged state in three-fold [108] or four-fold [109,110] co-ordination and negatively charged Bi in two-fold [111] or six-fold [110,112] co-ordination.

The second model assumes that the Bi incorporation is not homogeneous and that there are sub-microscopic regions of Bi_2S_3 or Bi_2Se_3 embedded in the glassy matrix. If the concentration of these microscopic entities exceeds the percolation threshold, then the conductivity should be *n*-type since both Bi_2S_3 or Bi_2Se_3 are rigid *n*-type semiconductors. EXAFS studies on Ge-B-S glasses showed that there is no evidence of inhomogenities in these glasses. However, Phillips argued [27] that assuming plastic deformation and atomic displacement in Bi_2S_3 microclusters of 30 to 40 Å dimension, the EXAFS results can in principle support the phase separation model.

A lot of experimental evidence has been reported in support of either of the above models by a number of researchers on various properties of these glasses. These properties include electrical conductivity and thermo electric power [111,112], resistivity under high pressure [113,114], drift mobility [115], photoconductivity [116,117], optical absorption [109,118], far IR transmission and reflectivity [119], Raman scattering [113], photo-emission [108] structural relaxation [110], calorimetry [120,121,122], photoacoustic spectroscopy [123,124], X-ray spectroscopy [125,126,127], *etc*. Thin films of Bi-Ge-Se glasses [120,125,126,128,129] and $Ge_{20}Bi_xSe_{70-x}Te_{10}$ glasses [128] have been prepared by thermal evaporation of the

bulk glasses. *p*- type to *n*- type charge carrier reversal has also been observed in thin films of Bi modified chalcogenide glasses.

Although it is difficult at this stage to say which of the above two models is most appropriate for describing the majority carrier reversal phenomenon in Bi modified Ge-Se-(Te) glasses, recent reports seem to favour the model based on the alternation of defect states by charged Bi defects [127].

1.9.2. Pb modified chalcogenide glasses

In 1987 Tohge *et al* [107] reported *p*- to *n*- type transition in $Pb_xGe_{42-x}Se_{58}$ and $Pb_{20}Ge_xSe_{80-x}$ glasses at x ≈ 9 at. wt. % Pb and x ≈ 21 at. wt. % Ge respectively. After the discovery of *p*- *to n*- transition in Pb-Ge-C (C = S, Se, Te) glasses [107], several studies have been reported in bulk Pb-Ge-Se glasses. They include differential scanning calorimetry [121,130,131], electrical conductivity and TEP [107,132,133,134], optical [121] and thermal diffusivity [135] studies. Most of these studies have attempted to investigate the composition dependence of a particular property of either the $Pb_xGe_{42-x}Se_{58}$ ($0 < x < 15$) or $Pb_{20}Ge_xSe_{80-x}$ series of glasses. The *p*- to *n*- type carrier reversal in $Pb_xGe_{42-x}Se_{58}$ ($0 < x < 20$) glasses has been interpreted in terms of the energetic disposition of Pb^{2+} in these glasses [131]. Recently, *p*- to *n*- type carrier reversal has been reported [136] in quarternary $Pb_xGe_{42-x}Se_{48}Te_{10}$ ($0 < x < 20$) glasses at x ~ 9 at. wt. % Pb. Electrical conductivity and TEP of these glasses have been reported and an explanation to the carrier reversal phenomenon in the lines of Kolobov's model has been provided. There are comparatively less number of investigations on the Pb modified chalcogenide glasses. Detailed studies on both the series of Pb-Ge-Se glasses is necessary to fully understood the mechanism responsible for the carrier reversal in these glasses.

There are two reports from the same research group [73, 137] on bulk $Pb_xIn_{25-x}Se_{75}$ (x = 0, 5, 10, 15) glasses, claiming *n*-type conduction in glasses with x ≥ 5 at. wt. % Pb. This is the only chalcogenide glass system without Ge to exhibit the *p*-type to *n*-type transition in the bulk form.

In this thesis work, lead (Pb) modified chalcogenide glasses have been taken up for study. Applications involving these glasses would generally demand knowledge of the properties of these glasses in the thin film form. Taking view of these factors, a systematic study of the optical, thermal and electrical properties of Pb modified chalcogenide glasses in bulk and thin film forms has been attempted in this thesis work.

भारतीय प्रौद्योगिकी संस्थान गुवाहाटी
Indian Institute of Technology Guwahati

Chapter 2
Experimental Techniques

In this chapter, the experimental techniques used in the current investigations are discussed together with the relevant theory associated with these techniques. Specific instruments and the measurement methodology used are also discussed. The experimental results presented in chapters 3, 4 and 5 are based on the experimental procedures outlined in this chapter.

2.1. Preparation of samples

2.1.1. Bulk glasses

Bulk glasses were prepared by melt quenching technique. Weighed quantities of high purity (99.999 %) elemental powders of lead (Pb), Germanium (Ge), Selenium (Se), Tellurium (Te), Indium (In) (corresponding to their at. wt. % in the desired glass composition) were taken in a fused silica ampoule of 8 mm diameter and 1 mm wall thickness. The ampoules were first rinsed with hydrofluoric acid (HF) and then with double distilled water. The cleaned ampoules were dried in a hot air oven and then stored away with a teflon tape seal. This ampoule containing the mixture of high purity elements was evacuated to about 10^{-5} Torr using a high vacuum pumping system, flame-sealed using a non–oxidising oxy-indane flame. The sealed ampoule was then loaded in a rotary furnace (figure 2.1). The rotary furnace was a modified tubular furnace of 50 mm diameter. The tubular furnace was heated by an assembly of silicon carbide (SiC) heating elements. The temperature of the furnace could be controlled to ± 2 °C at 600 °C and ± 4 °C at 1100 °C. A ceramic tube of 20 mm diameter was inserted into this tubular furnace. This inner alumina tube was connected to a synchronous a.c. motor capable of rotating at 60 rpm. Initially, the ampoule was heated in slow steps up to the desired temperature

(typically, 1000 ˚C). The inner tube containing the ampoule was then rotated for about 10 hours at this temperature and then the ampoule was suddenly dropped into a bucket containing NaCl + ice + water mixture. The furnace temperature during quenching, the temperature of the NaCl + ice + water mixture and the weight of melt in the ampoule were maintained at fixed values in order to ensure similar quenching condition for all samples.

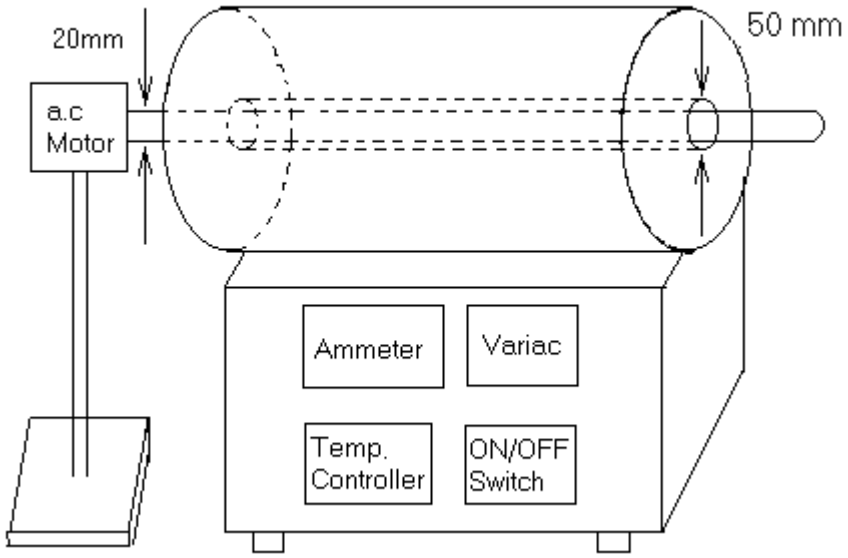

Figure 2.1: Block diagram of the rotary furnace.

2.1.2. Thin films of glasses

Thin films of chalcogenide glasses were prepared by thermal evaporation technique. Figure 2.2 shows the schematic diagram of the high vacuum unit used for depositing thin films by thermal evaporation technique. The unit consists of a stainless steel (SS 316) deposition chamber of length 50 cm, breadth 45 cm, and height 30 cm. This chamber could be evacuated to a low pressure of < 10^{-5} Torr by a pump assembly (DP+RP). The pump assembly is made up of a 4½ inch oil diffusion pump backed by a rotary pump. The pumping speed of the diffusion and rotary

pumps are 500 litres.s^{-1} and 250 litres.min^{-1}, respectively. Rough vacuum in the chamber was measured using a Pirani gauge and high vacuum with a Penning gauge. Two copper electrical feed-throughs were used as electrical connectors for the heating element (evaporation boat, MB). Powdered glass samples were loaded in MB made of high purity molybdenum sheet. The current to the boat could be set at any desired value up to a maximum value of 200 A. The sample holder (SH) was a disc of aluminium of diameter 20 cm and thickness 5 mm. SH could be rotated about the vertical axis by a 1/8 h.p. a.c. motor with the help of a rotary feed-through. The rpm of the motor could be set at any desired value with a help of a control circuit. The temperature of the SH could be varied with the help of accessories such as a liquid nitrogen container and a radiant heater.

For the preparation of thin films of Pb modified Ge-Se(-Te) glasses, bulk glass of appropriate composition was taken in the evaporation boat. Microscope cover slips (borosilicate glass) of length 18 mm, breadth 18 mm and thickness 0.25 mm were used as substrates for deposition of these films. These substrates were rinsed first with detergent solution and then cleaned in an ultrasonic bath [Elma Transsonic 460/H] for about 15 minutes. The cleaned substrates were then dried in a hot air oven. The source to substrate distance was kept at about 25 cm. and the substrate holder was rotated to avoid differential deposition. The molybdenum boats were baked under vacuum for 5 minutes before use and the pressure inside the deposition chamber was maintained at 5×10^{-5} Torr prior to deposition.

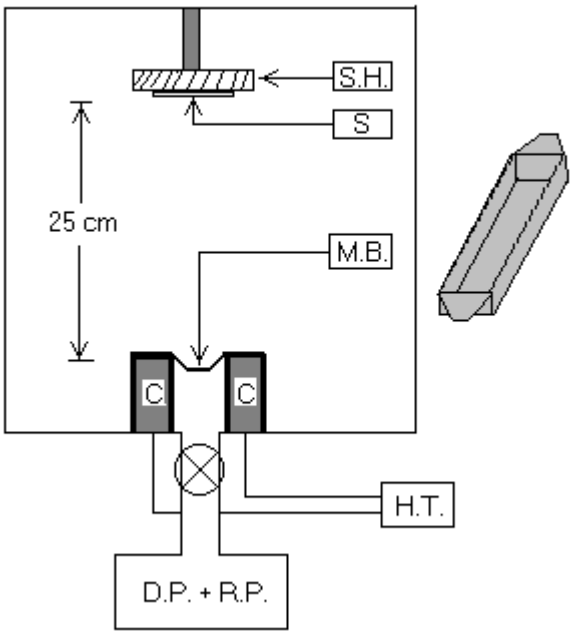

Figure 2.2: Block diagram of thin film coating unit [C - Copper electrodes, H. T.- High voltage circuit, M. B. – Molybdenum evaporation boat, S- Substrate, S. H. - Substrate Holder, D. P. - Diffusion Pump, R.P. - Rotary Pump].

2.2. Characterisation using X-ray diffraction

A commercial X-ray diffraction system for powder samples (Seifert XRD 3003 T/T) was used for the verification of the amorphous nature of the as-quenched glass samples. Cu K_α radiation (1.541 Å) with a Nickel filter was used. The instrument was calibrated with a standard Si reference. The X-ray generator was operated with an acceleration voltage of 40 kV and tube current of 30 mA. The theta-theta goniometer was used in the reflection (Bragg-Brentano) geometry (figure 2.3). A thick layer of powdered sample spread over a poly methyl metha-acrylate (PMMA) plate was used for recording the X-ray diffraction (XRD) patterns. The XRD data provides the variation of intensity/counts per second (cps), recorded by the detector (scintillation counter) as a function of 2θ, where θ is the glancing angle. XRD patterns were

recorded by varying 2θ from 10^0 to 70^0 in steps of 0.02^0. A typical XRD pattern of a glass sample is shown in figure 2.4.

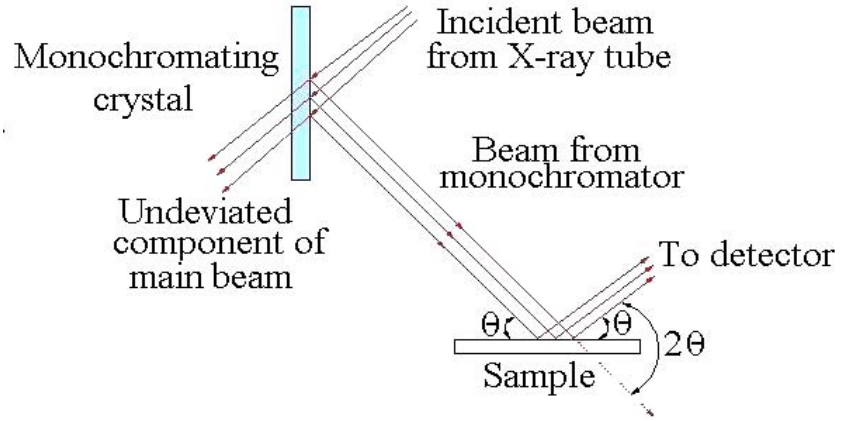

Figure 2.3: Ray diagram of an X-ray diffractometer.

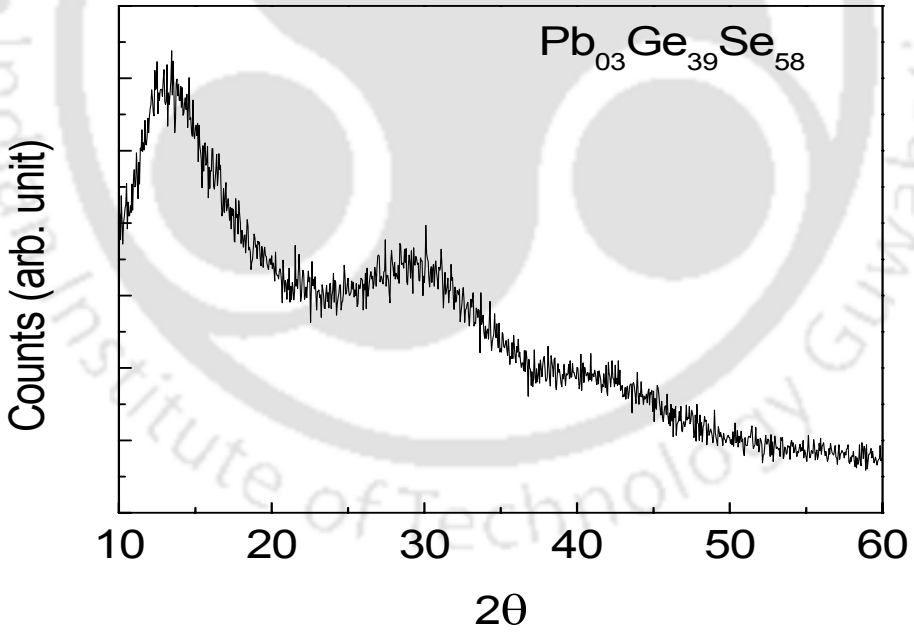

Figure 2.4: A typical XRD pattern of a bulk glass sample.

The absence of sharp crystalline (Bragg) peaks in the XRD pattern with broad humps is the typical signature of an amorphous material. This experimental

technique was used to confirm the amorphous nature of all the samples prepared for the present investigations.

The XRD pattern of a crystalline solid is almost zero everywhere except at the Bragg's angle (θ_B). One would expect a Bragg peak to be very narrow. However, it has been found that the finite number of planes responsible for the Bragg peak results in the broadening of the peak. This phenomenon has been put to use for rapid detection of crystallite size. Starting from the Bragg's law, Scherrer derived an expression for the thickness (t) of the crystallite which is given by the expression [138],

$$t = \frac{\lambda}{B\cos\theta_B}$$

where λ is the wavelength of the X-ray used, B is the FWHM of the Bragg peak and θ_B is the Bragg's angle. For the determination of particle (Crystallite) size, a more exact treatment leads to the equation

$$t = \frac{0.9\lambda}{B\cos\theta_B}$$

The above relation provides reasonable estimate of particle size in the range 10 Å to 1000 Å. This method is useful especially when very few peaks are available for analysis [139].

For the structural analysis of a thin film deposited on a glass substrate, grazing incidence diffraction (GID) technique was used. The refractive index for most of the materials is slightly less than unity at X-ray energies. One can therefore have total external reflection from a surface if the incident angle is small enough (typically 0.05˚ to 1.5˚), depending on the nature of the substrate, electron density and the X-ray energy. Although the substrate is not entirely invisible to X-rays at this point, only an evanescent wave penetrates into the surface and is subsequently scattered from

it. Thus, the X-ray intensity is highest at the surface as desired. It is possible to increase the surface selectivity further by reducing the incident angle which causes the evanescent wave to damp out faster. GID technique works only with very smooth surfaces [140] since surface variations normal to the incident beam can upset the total external reflection condition. A focused incident beam contains a range of incident directions and therefore not all the photons would land below the critical angle for total external reflection. Therefore, a compact and collimated beam of X-rays is required for a good GID. In the present studies, a söller slit assembly called the Grazing Incidence Device was used for obtaining a collimated beam of x-rays suitable for GID work.

2.3. Differential scanning calorimeter

Differential scanning calorimeter (DSC) is a thermal analysis technique with which the thermal behavior of a sample can be studied over a wide temperature range, under isothermal as well as non-isothermal conditions. This thermal technique was commercially developed by Watson *et al* [141]. In this technique, the sample and reference are maintained at the same temperature with respect to each other by proper application of electrical energy. The heat flow, dH/dt to the sample and the reference at the same temperature is recorded as a function of temperature. The reference is an inert material such as alumina (Al_2O_3) or just an empty aluminum sample pan. In non-isothermal measurements, the temperature of the sample and reference are increased at a constant heating rate. Thermal changes in a sample may be of exothermic or endothermic nature. Some examples of endothermic transitions are the glass transition, reduction, dehydration and some decomposition reactions. Crystal-crystal structure transformation, glass-crystal transition, oxidation

and some decomposition reactions are the most frequently studied exothermic transitions.

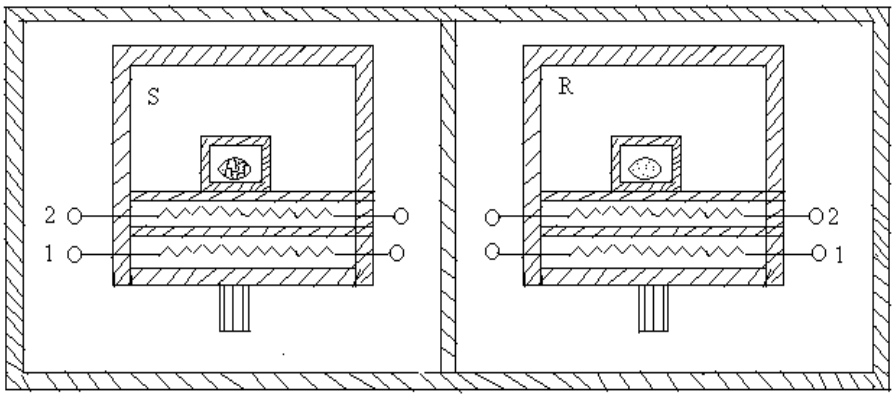

Figure 2.5: Microfurnace assembly in a DSC. S is the sample compartment with sample crucible, R is the reference compartment, 1 is the heater and 2 is the platinum resistance thermometer.

A commercial instrument (Perkin-Elmer, DSC 7) was used in the present investigations. This is a power compensation Differential Scanning Calorimeter in which the heat to be measured is almost totally compensated with electric energy, by increasing or decreasing an adjustable Joule heat. The measuring system consists of two thermally insulated microfurnaces made of a platinum-iridium alloy. A temperature sensor (platinum resistance thermometer) and a heater (made of platinum wire) are embedded in each of these microfurnances (figure 2.5). The measuring range could be extended from –175 ºC (liquid nitrogen cooling) to 725 ºC. In the present studies, the instrument was calibrated for optimum performance from 50 ºC to 500 ºC. High purity zinc (m.p. = 418.6 ºC) and indium (m.p. = 156 ºC) were used to calibrate the instrument's temperature scale. Measurements were done with weighed quantities (~ 20 mg) of glass samples taken in crimped aluminium sample pans. High purity nitrogen gas was continuously purged during the entire duration of the experiment. DSC curves were recorded at constant heating rates of 10, 15, 20 and 30 ºC.min^{-1}.

A typical DSC trace of a glass is shown in figure 2.6. When a glassy sample is heated at a constant heating rate in a DSC, the heat flow exhibits an endothermic baseline shift at the glass transition temperature (T_g), followed by an exothermic peak at the crystallization temperature (T_c). Further heating results in melting of the crystallised sample at the melting temperature (T_m), which is an endothermic transformation. Generally, glasses which are unstable show one or more exothermic peaks corresponding to devitrification of various crystalline phases. Such glasses may sometimes show multiple melting endotherms as well. The T_g values reported in the present studies correspond to the on-set of the glass transition (figure 2.6). The crystallisation temperature reported corresponds to the value at the maximum of the exothermic peak.

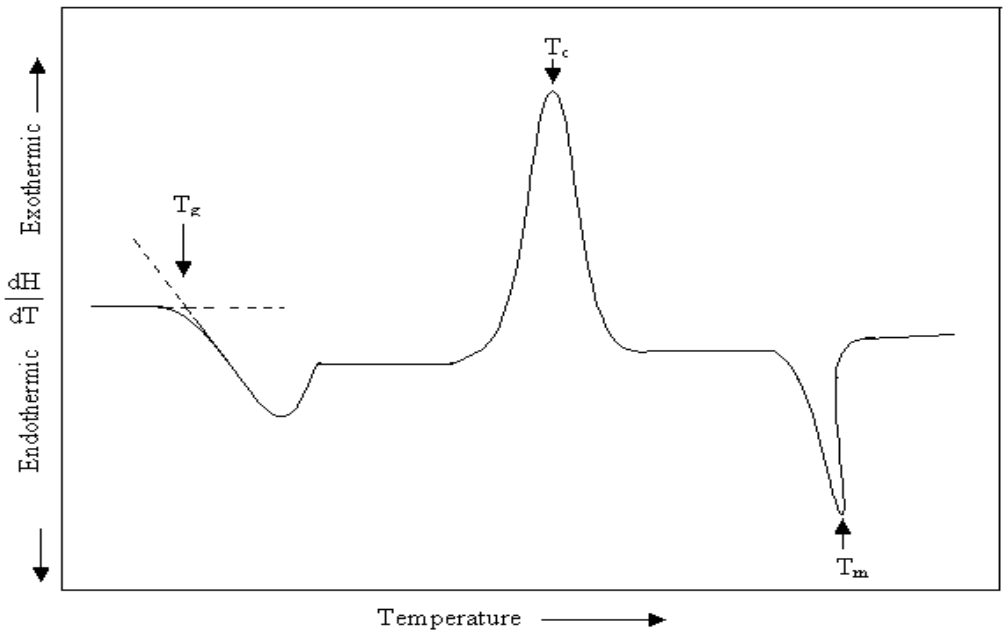

Figure 2.6: A typical DSC curve of a glassy material subjected to a constant heating rate.

A kinetically controlled reaction temperature (such as T_g or T_c) shifts with heating rate. Once the data on T_g and T_c at different heating rates are available, the activation energy of the reaction (which is a measure of the inhibition to the process) could be estimated using the formalism due to Kissinger or Augis–Bennett or Thakor

[142,143]. These methods provide Arrhenius form of relations from which the activation energy could be determined. The Kissinger, Augis-Bennett and Thakor relations are given in equations (2.1), (2.2) and (2.3) respectively.

$$\frac{d\left[\ln\left(\frac{\varphi}{T_g^{\,2}}\right)\right]}{d\left[\frac{1}{T_g}\right]} = -\frac{E_K}{R} \qquad (2.1)$$

$$\frac{d\left[\ln\left(\frac{\varphi}{T_g}\right)\right]}{d\left[\frac{1}{T_g}\right]} = -\frac{E_{A-B}}{R} \qquad (2.2)$$

$$\frac{d\left[\ln\left(\varphi\right)\right]}{d\left[\frac{1}{T_g}\right]} = -\frac{E_T}{R} \qquad (2.3)$$

where φ is the heating rate, E_K, $E_{A\text{-}B}$, and E_T are the activation energy obtained from the Kissinger, Augis-Bennett and Thakor equations, respectively, and R is the universal gas constant. It is evident from the numerator in the equations (2.1), (2.2) and (2.3) that $E_T > E_{A\text{-}B} > E_K$, which has been verified [144,145]. The activation energy for glass transition E_K (Kissinger) and E_T (Thakor) were calculated from the slope of the least squares fit to Kissinger's plot [$\ln(\varphi/T^2)$ versus $1000/T$] and Thakor's plot [$\ln(\varphi/T)$ versus $1000/T$]. Typical Kissinger's plots obtained for the two sets of Pb modified chalcogenide glasses are shown in figure 2.7. The corresponding Thakor's plots for the same sets of Pb modified glasses are shown in figure 2.8.

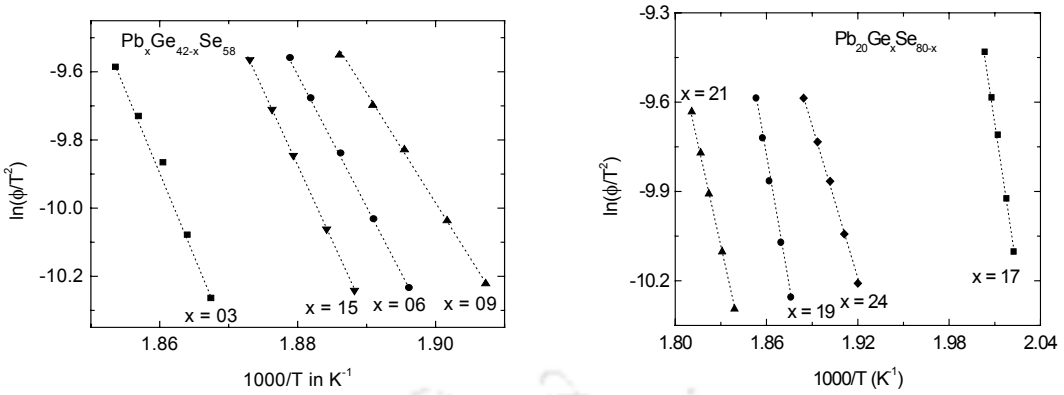

Figure 2.7 : Kissinger's plots for (a) $Pb_xGe_{42-x}Se_{58}$, and (b) $Pb_{20}Ge_xSe_{80-x}$ glasses.

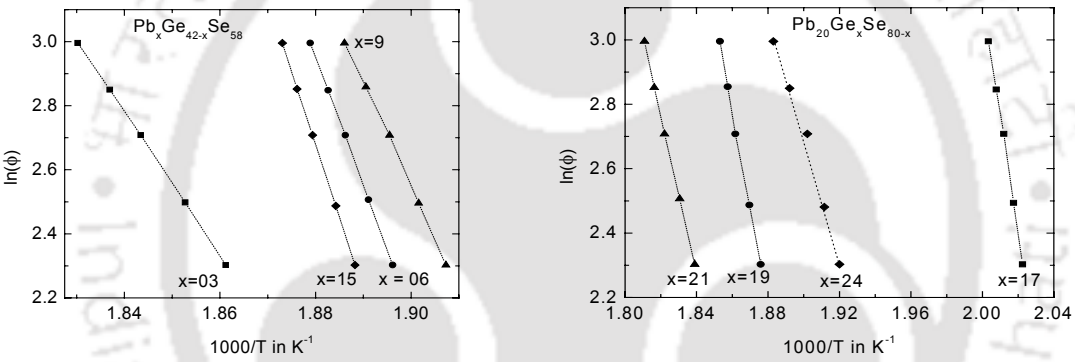

Figure 2.8 : Thakor's plot for (a) $Pb_xGe_{42-x}Se_{58}$, and (b) $Pb_{20}Ge_xSe_{80-x}$ glasses

The heat capacity jump at T_g (ΔC_p) is a typical feature of a glass. ΔC_p exhibited by a glass as it is heated at a constant heating rate through T_g could be determined by the methods of a ratio proposed by O'Neill [146]. This procedure requires three DSC curves $\frac{dH}{dt}$ versus T under identical conditions. One for obtaining base-line over the temperature range of interest, the second run with weighted quantity of a reference material (usually α-Al_2O_3 or saphire crystal) and the third run with weighted quantity of the glass sample (figure 2.9).

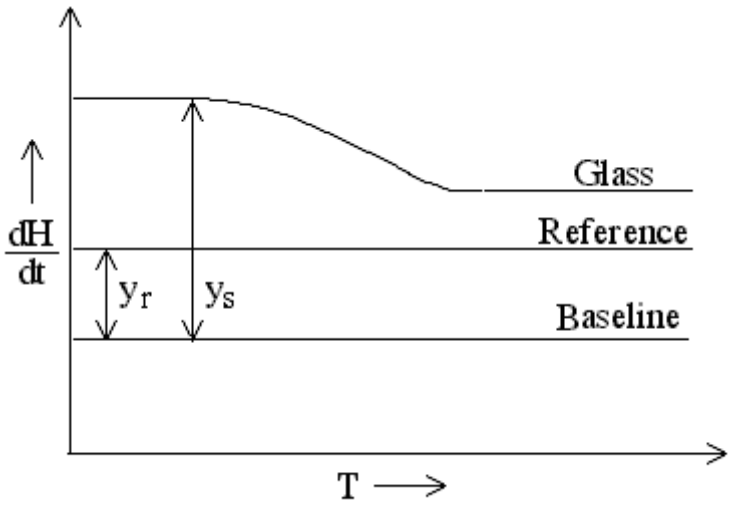

Figure 2.9 : Typical curve for ΔC_p at T_g of Pb modified chalcogenide glasses.

The co-ordinate deflection of the reference curve with respect to the base-line (y_r) and the sample curve with respect to the base-line (y_s) are then measured. If the heat capacity of the reference (C_{pr}) is known, then the heat capacity of the sample (C_{ps}) is given by,

$$C_{ps} = \frac{y_s\, m_r}{y_r\, m_s} C_{pr} \qquad (2.4)$$

where m_r and m_s are the masses of the reference and sample. C_{ps} of the sample is then plotted as a function of temperature. The heat capacity jump at T_g (ΔC_p) is then calculated from such a curve as depicted in figure 2.9. DSC instruments can directly provide ΔC_p values through a software. In this thesis work, the procedure proposed by O'Neill was used to obtain ΔC_p values of the Pb modified glasses.

The degree of fragility of a glass can be defined in terms of the relaxation time for viscosity (τ) as,

$$m = \frac{d\log_{10}(\tau)}{d\left(\frac{T_g}{T}\right)} \qquad (2.5)$$

Depending on the value of the degree of fragility (m), glasses can be classified as strong or fragile glass. The lower limit of m for the strong glass is 16, whereas, the upper limit for fragile glass is 200 according to theoretical estimation. [16,147]. As already discussed in the first chapter, minimum ΔC_p could be correlated to minimum thermodymanic fragility (or maximum thermodynamically strong nature) of this glass composition. The degree of fragility can also be obtained from the Tool-Narayanswamy-Moynihan (TNM) expression,

$$\tau = \tau_0 \exp\left(\frac{x\,\Delta h^*}{RT}\right)\exp\left(\frac{(1-x)\,\Delta h^*}{RT_f}\right) \qquad (2.6)$$

where x (0 < x < 1) is the non-linearity parameter, Δh^* is the apparent activation energy and T_f is the fictitive temperature (*T_f is the temperature at which the structure of the glass would be in equilibrium if instantaneously removed to it*). Substituting the above value of τ in the expression for m equation (2.5) gives

$$m = -\frac{\Delta h^*}{RT_f \ln(10)} \qquad (2.7)$$

The fictitive temperature T_f has been found to be close to the value of T_g obtained from DSC measurements [16]. If the difference in excess heat capacity and the change in enthalpy is negligible [or independent of heating or cooling rate (q)], then the relationship between quenching rate (q) and glass transition temperature (T_g) can be given by

$$\frac{d\ln|q|}{d\left(\frac{1}{T_g}\right)} \approx -\frac{E_\eta}{R} \qquad (2.8)$$

where E_η is the activation energy for viscous flow. The above equation is in the same form as equation (2.3). Equation 2.8 is known as Bartenev's equation [79]. Comparing equation 2.3, 2.7 and 2.8 one can see that Δh^*, E_η and E_T refer to the

same quantity. Hence, degree of fragility m has been related to E_η by the relation [148],

$$m = \frac{E_\eta}{2.3RT_g} \qquad (2.9)$$

where R is the universal gas constant. In this thesis, the notation E_η has been used to refer to the activation energy obtained using the above relations. This should not be misunderstood as referring to data obtained from viscosity measurements.

Comparing the values of ΔC_p and m (or E_η/T_g) provides a means to classify glasses into four groups such as (TS-KS), (TS-KF), (TF-KS), (TF-KF) where TS, TF, KS, KF stands for thermodynamically strong, thermodynamically fragile, kinetically strong, kinetically fragile respectively [16]. The above procedure was used to determine the degree of fragility in succeeding chapters.

2.4. Thermoelectric power measurement

Thermoelectric power (TEP) or Seebeck coefficient (Q) of glasses has been discussed in chapter 1. Thermoelectric power measurements were performed on as-quenched (bulk) samples using an indigenously developed set-up. A temperature gradient was maintained across a thin slice of glass sample by passing an electric current through a resistive heater embedded inside a copper block on which the sample was placed (figure 2.10). A spring-loaded copper rod, which served as an electrode was placed over the sample. The potential difference developed due to thermal conduction through a thin slice of the sample was recorded using an electrometer (Keithley 6512). The temperature gradient between the lower and upper sample surfaces was monitored using two calibrated thin film PT100 sensors placed on the two sides of the sample. The resistance values of the calibrated sensors were

recorded using two digital multimeters (Hewlett Packard 34401A). The whole assembly was kept in a vacuum chamber capable of maintaining a low pressure of < 10^{-4} Torr. With this arrangement, the thermoelectric power of the samples could be measured from room temperature to 450 K with an experimental error of ± 2 %. As a convention, the lower surface of the sample (hot end) was connected to the positive terminal of the electrometer and the upper surface (cold end) was connected to the common terminal of the electrometer.

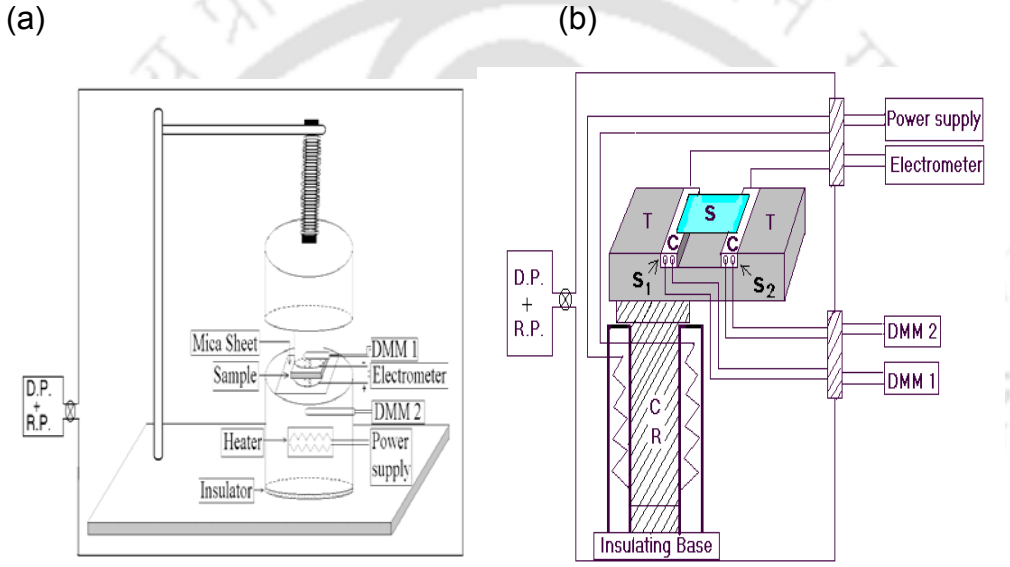

Figure 2.10: Schematic of the thermoelectric power measurement set-up for (a) bulk samples, and (b) thin film samples [Please see text for a description of the derivation used].

For the TEP measurement on thin films, a set up shown in figure 2.10b was designed and fabricated. The sample holder (TT) consisted of a teflon base with a cleft in the centre. Two copper square rods of 5 mm side were embedded on either side of this cleft. These copper plates served as the two electrodes for TEP measurements. Calibrated platinum resistance sensors S_1 and S_2 (PT 100) embedded in the copper rod served as temperature sensors. The teflon assembly rested on a copper rod (C.R.) which was inserted into a tubular heating coil wound over a ceramic tube. The whole assembly was placed in such a manner that one end

of the teflon sample holder could be heated up to 450 K. Such an arrangement provided a temperature difference of about 20 °C between the two copper electrodes. During TEP measurements, the substrate containing the thin film was placed between the copper plates (with the film side facing the electrodes) and gently pressed with a teflon lid from the top (not shown in figure). The complete unit was placed inside a vacuum chamber which could be evacuated to better than 10^{-4} Torr. The resistance of the PT 100 sensors corresponding to the temperature at the two ends of the thin film sample was read by two 6½ digit digital multimeters (HP 34401A) and the thermo e.m..f developed across the sample was measured with an electrometer (Keithley 6512). As a convention, the hot end of the film is connected to the positive terminal of the electrometer and the negative terminal to the cold side. The electrical connections for the heater, thermo e.m.f. measurement and sensors and were taken out through an electrical feed through.

When a temperature difference, ΔT is established between the upper and lower surfaces of a bulk samples (or the two ends of a thin film sample), charge carriers moves from the hot probe to cold probe, thus creating a thermo e.m.f. ΔV across the sample. The Seebeck coefficient is then given by, $Q = -\frac{\Delta V}{\Delta T}$. If the potential difference measured by the electrometer (using the convention specified above) is negative, then Q is positive and the sample is a *p*-type semiconductor. On the other hand, if the potential difference is positive then Q is negative and so the sample is an *n*-type semiconductor. The majority charge carrier type in each bulk and thin film sample was identified and quantified using the TEP measurement. The above procedure yielded Q values with an uncertainty of ± 2 %.

2.5. Thin film thickness measurement

Ellipsometry was used for determining the thickness of the evaporated thin films. In this technique, the change in polarization state of a polarized light beam incident on the sample at an oblique angle is measured. The relationship between the thickness of the film and the optical constants of the surface (or substrate) upon which the film is deposited is given by [149],

$$\tan\Psi e^{i\Delta} = \frac{(r_{p01} + r_{p12}e^{-2ix})}{(1 + r_{p01}r_{p12}e^{-2ix})} \frac{(1 + r_{s01}r_{s12}e^{-2ix})}{(r_{s01} + r_{s12}e^{-2ix})} \quad (2.10)$$

where, $x = \frac{2\pi}{\lambda} d(n_1^2 - n_0^2 \sin^2\varphi)^{1/2}$, $r_{p,s01}$ = the Fresnel reflection coefficient for the air-film interface, $r_{p,s02}$ = the Fresnel reflection coefficient for the film-substrate interface, n_0 = refractive index of the air, n_1 = refractive index of film, d = thickness of film, λ = wavelength of light, φ = angle of incidence, Ψ = the amplitude ratio and Δ = the phase difference.

An ellipsometer is used to measure ψ and Δ from which the film thickness and refractive index can be calculated. Figure 2.11 shows the schematic diagram for the ellipsometer (Gaertner L119XUV) used for measuring the thickness of the thin films. In actual practice, the measurement consists of setting the compensator at a fixed angle and rotating the polarizer and analyzer circles until the reflected beam from the specimen is extinguished. When the extinction is achieved, the polarizer and analyzer circles are read and these readings are converted into film thickness and refractive index by a computer program.

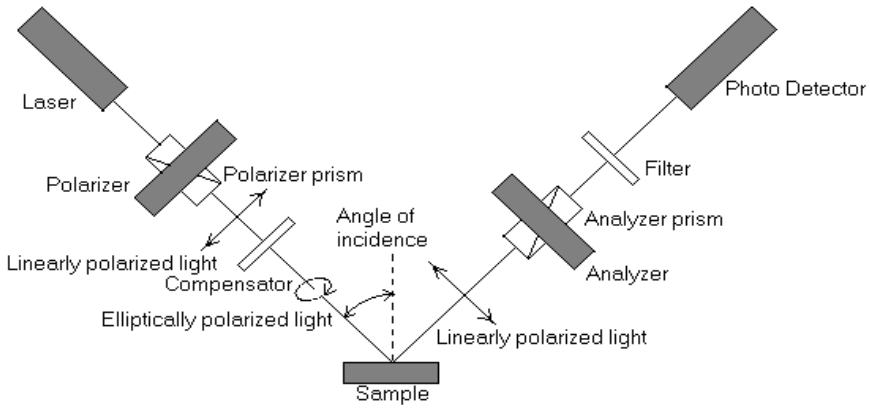

Figure 2.11: Schematic diagram for an ellipsometer showing the different components and the general geometry of the experiment.

2.6. Compositional analysis of glass samples

The composition of bulk glasses and the thin film of these glasses could be analysed using a Scanning Electron Microscope (SEM) with Energy Dispersive X-ray Analysis (EDX) accessory. EDX analysis of the composition of the sample is based on the following principle. When an electron beam strikes a solid surface, electrons and X-rays are emitted from the surface (figure 2.12a). The x-ray photon may be absorbed by an atom resulting in the ejection of one of the bound electrons of that atom. The energy distribution of emitted X-rays and electrons are shown in figure 2.12b and figure 2.12c respectively.

(a)

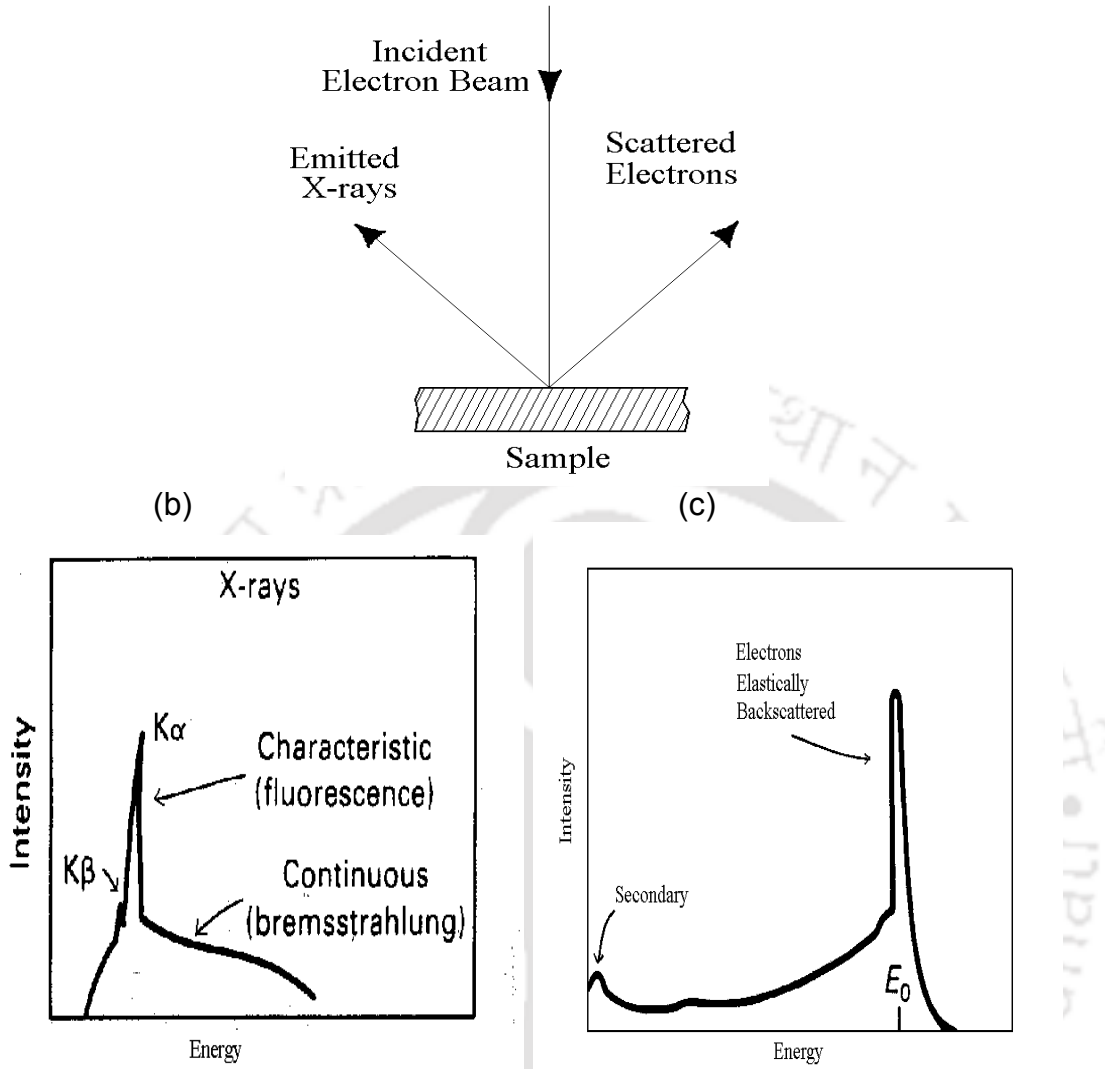

Figure 2.12: Energy distribution of (a) the scattering process of an electron beam in a SEM (b) X-rays and (c) electrons after emission from the sample surface.

X-rays emitted from the surface are detected by the energy-dispersive X-ray detector. Energy dispersive X-ray detectors normally detect X-ray energies from 0.185 keV (Boron K) to about 15 keV. In principle, this energy range is sufficient to cover at least one x-ray line (from the K-, L-, or M- family) of all elements with atomic number $Z > 4$ listed in the periodic table. The detector generates electrical signals proportional to the intensity of these X-ray lines from which the atomic constitution of the surface could be determined. Thin window energy-dispersive detectors allow

detection of elements with Z as low as 6 carbon [150]. The characteristic X-ray line(s) emitted by the sample are recorded for analysis of the sample composition. The composition analysis was performed by a standardless analysis procedure. In this procedure the elements are quantified by calculating the area under the peak of each identified element. Sensitivity factors required to convert the area under the peak into appropriate weight or atomic percent were then computed after taking into account the accelerating voltage of the beam used to produce the spectrum. One of the popular algorithms used for this purpose is called the ZAF [151], where Z stands for the atomic number of the element. A and F are the absorbance and fluorescence values are used for the data reduction. Standard software packages supplied by the SEM-EDX manufacturer was used without any further modification to obtain the percentage constitution of various elements in the samples.

Compositional analysis on glass samples were done using a commercial SEM-EDX instrument (JEOL, JSM-5800). Both spot and overall analysis were performed on the samples. Since the glass samples had low electrical conductivity at room temperature, a conducting layer of carbon was deposited on the samples prior to analysis. The carbon coating was done using a sputtering unit supplied along with the SEM-EDX instrument. The SEM-EDX was operated with an acceleration potential of 20 kV and each spectrum was collected for about 100 s. A typical EDX spectrum of one of the Pb modified glass samples is shown in figure 2.13. The sample surface was first inspected with the SEM. SEM inspection of Pb-Ge-Se and Pb-Ge-Se-Te showed a homogenous surface with a few voids. SEM inspection of Pb-In-Se films showed sub-micron regions of crystallinity. The results obtained on Pb-In-Se films would be discussed in chapter 5.

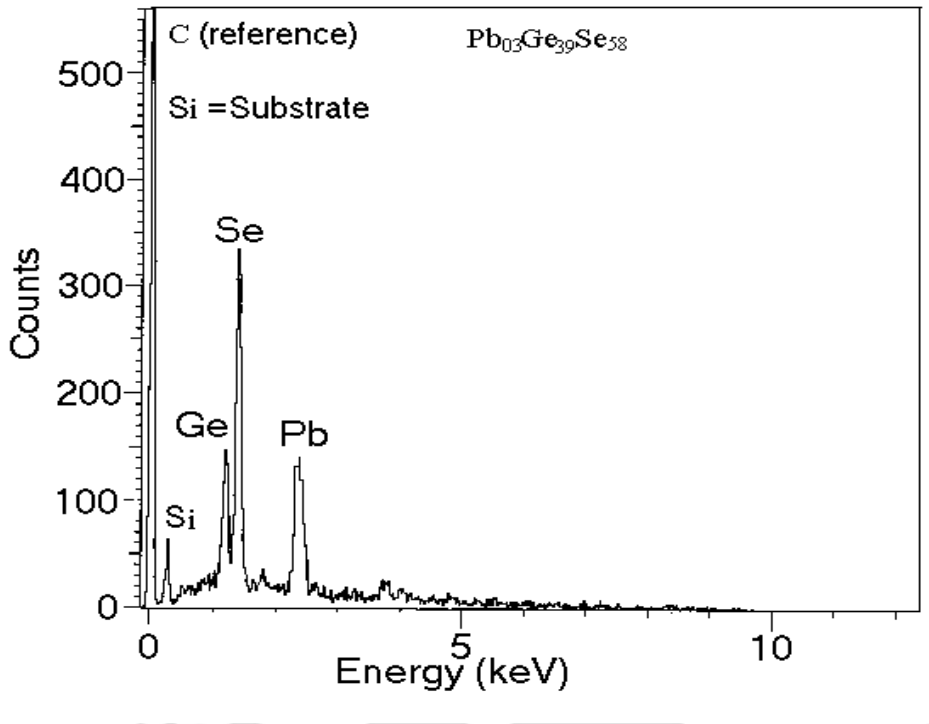

Figure 2.13: EDX spectrum of the Pb-Ge-Se glass

2.7. Optical band gap measurement

Ultraviolet-visible-near infra-red spectrophotometer permits one to measure [79] the optical absorbance of a thin slice of glass as a function of wavelength (λ). The optical band gap of semiconducting glasses can be estimated from the optical absorption curves [152]. A typical absorption curve of a Pb modified Ge-Se-Te glass is shown in figure 2.14.

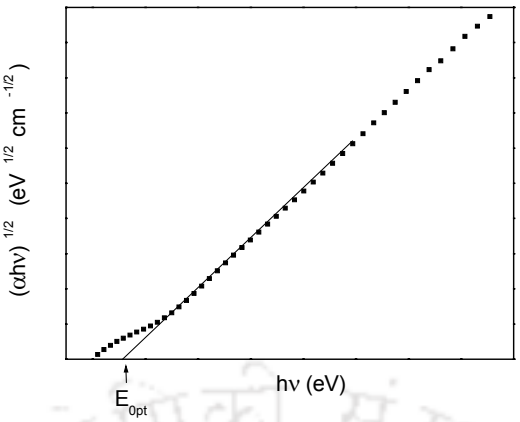

Figure 2.14: $(\alpha h\nu)^{1/2}$ versus hν plot for a typical chalcogenide glass sample.

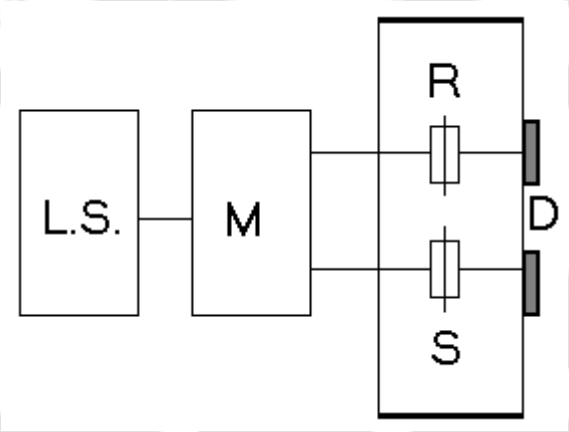

Figure 2.15: Block diagram of a double beam uv-vis-nir spectrophotometer. [LS= Light sources (Deuterium and halogen lamp), M=double grating monochromator,R=Reference,S=Sample,D=Detector (Photomultiplier tube and PbS)

A commercial dual beam uv-vis-nir spectrophotometer (Shimadzu UV-3101PC) was used for recording the optical absorption curves of glass samples. This optical system (figure 2.15) consists of a double grating monochromator M, light sources LS (deuterium lamp and halogen lamp) and a detector assembly D (Photomultiplier tube and PbS detector). The optical spectrophotometer is controlled by a personal computer supported by a software provided by the instrument manufacturer. Wavelength can be continuously varied between 190 nm and 3200 nm for absorption measurements. In the present investigation, a wavelength range of

300 nm to 800 nm was sufficient for the measurement of optical band gap of the samples studied.

2.8. Microhardness measurement

The microhardness (or simply the hardness measured over a micron distance scale) is a characteristic property of solids. The hardness is a measure of the resistance of a material to being penetrated and eroded by another material's sharp projections. The popular measurement method involves the use of a diamond micro indenter in the shape of a square pyramid (Vickers). Figure 2.16 shows the geometry of Vickers square pyramidal indenter.

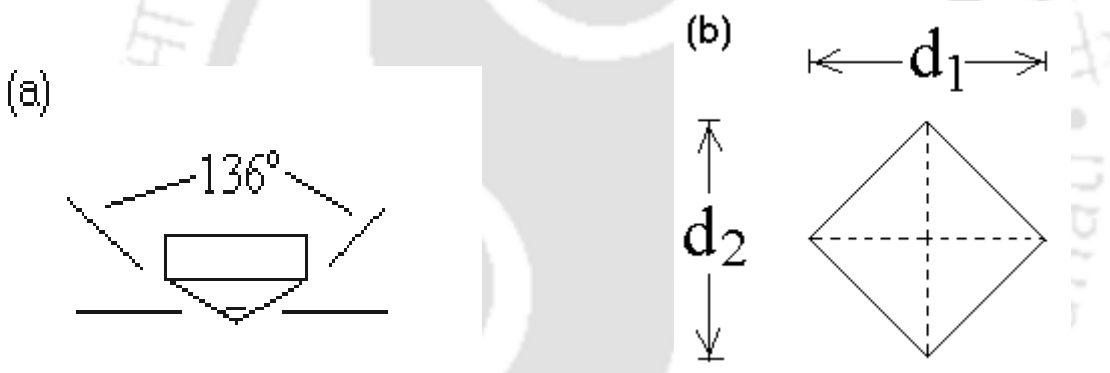

Figure 2.16: (a) Geometry of Vickers square pyramidal indenter. (b) d_1 and d_2 are the diagonals of the indentation made on the sample by a Vickers pyramidal indenter.

For the Vickers indenter,

$$\text{VHN} = \frac{\text{force}}{\text{area}} = \frac{2\text{F}\sin\left(\frac{\theta}{2}\right)}{\text{d}^2} \qquad (2.11)$$

where F is the force in kg, θ is the inclined angle of Vickers pyramid and d [= $(d_1+d_2)/2$] is the average diagonal of the impression in mm. Since θ = 136° for the Vickers pyramid, VHN (expressed usually in units of $kg.mm^{-2}$) may be written as,

$$VHN = \frac{1.8544F}{d^2} \quad (2.12)$$

Total indentation time range between 15-25 seconds was used for the present measurements, which was sufficient for the load to gradually descend onto the surface and reach an equilibrium penetration depth. When an indentation is made in a glass, initially the glass is elastically compressed (by the hydrostatic component) and sheared (by the shear component). Next, after reaching the elastic limit, the balance of the hydrostatic stress component permanently densifies the glass under the indentation, whereas the balance of the shear stress component causes the glass to undergo plastic deformation [153,154]. When the indenter is withdrawn, the elastic portion recovers, *i.e.*, a slight shrinkage of the impression size is expected. Clearly, the hardness number cannot be independent of the applied load. Also, when large loads are used, cracking from the diagonals is likely to develop. The cracking implies the occurrence of a fracture.

Careful preparation of the sample surface is necessary prior to indentation. For this, the samples were mounted on a resin and given a mirror finish. The polished samples were then indented using a Vickers diamond pyramidal indenter. The diagonal lengths of the indents were measured using an optical microscope. A typical indentation made on a polished glass sample is shown in figure 2.17. The indentation corresponds to an applied load of 50 gm and loading time of 15 seconds. The microhardness values reported in this thesis are the average values of at least ten independent indents made on each sample composition under identical loading conditions. In the present study, a Buehler Simplet 2 mounting press, a Buehler Ecomet 6 variable speed grinder/polisher and a Buehler Micromet 2100 automated microhardness tester were used. All measurements were made at room

temperature.

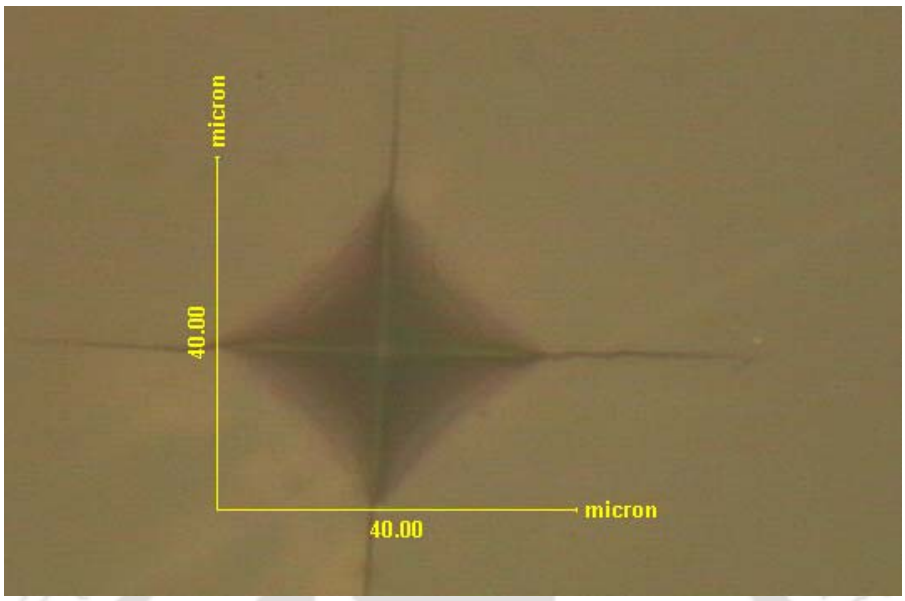

Figure 2.17: A typical indent made on a polished glass surface using a Vickers pyramidal indenter.

2. 9. d. c. electrical conductivity measurement

Many conventional methods for measuring electrical resistivity are unsatisfactory for semiconductors because metal-semiconductor contacts are usually rectifying (non ohmic) in nature [155]. There is also the possibility of minority carrier injection by one of the current carrying contacts. An excess concentration of minority carriers will affect the potential of other contacts and modulate the resistance of the material [78]. The collinear four-probe method used as experimental technique for measuring resistivity overcomes the difficulties mentioned above and also offers several other advantages. It permits measurements of resistivity [156] in samples having a wide variety of shapes, including the resistivity of small volumes within a bigger piece of semiconductor. The basic experimental arrangement for the collinear four-probe measurement is indicated in figure 2.18.

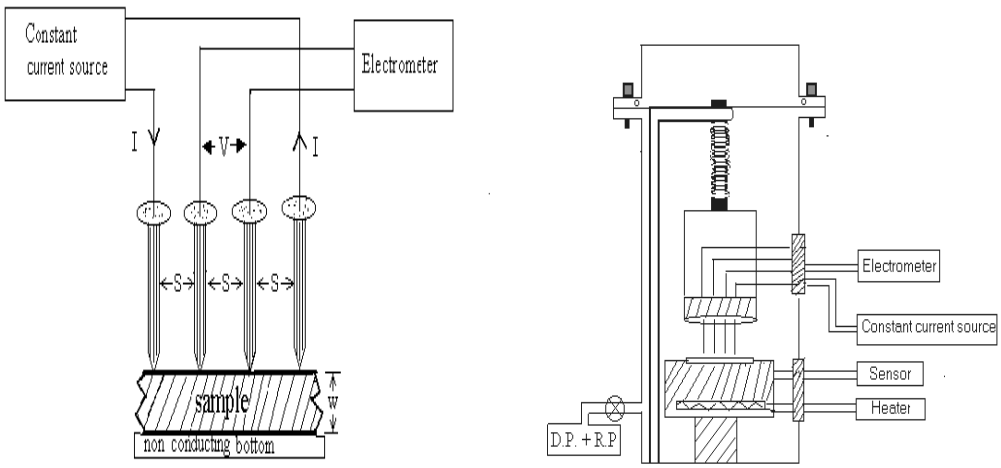

Figure 2.18: Schematic diagram of electrical resistivity set-up. The probe assembly is shown in the left and the complete unit encased in a vacuum chamber is shown in the right.

Four sharp probes are placed on a flat surface of the material to be measured. Current is passed through the outer electrodes and the floating potential is measured across the inner pair. If the flat surface on which the probes rest is adequately large and the sample is big enough, the semiconductor may be considered to be of semi-infinite volume [157]. To prevent minority carrier injection and to make good contacts, the surface on which the probes rest may be mechanically clamped. The experimental circuit used for measurement is illustrated in figure 2.18 and the following points are assumed:

The resistivity of the material is uniform in the area of measurement.

There is no minority carrier injection into the semiconductor by the electrodes.

The surface on which the probes rest is flat with no surface leakage.

The four probes used contact the surface at points that lie in a straight line.

The diameter of the contact between the metallic probes and the semiconductor is small compared to the distance between the probes.

The boundary between the current carrying electrodes and the bulk material is

hemispherical and small in diameter.

The bottom surface of the semiconductor is non-conducting.

Let the four probes be spaced S_1, S_2 and S_3 apart. Current I is passed through the outer probes (1 and 4) and the floating potential V is measured across the inner pair of probes 2 and 3. The floating potential V_f at a distance r from an electrode carrying current I in a material of resistivity ρ_o is given by

$$V_f = \frac{\rho_o I}{2\pi r} \tag{2.13}$$

There are two current carrying electrodes numbered 1 and 4 and the floating potential V_f at any point in the semiconductor is the difference between the potential induced by each of the electrodes, since they carry currents of equal magnitude but in opposite directions [158, 159]. Thus

$$V_f = \frac{\rho_o I}{2\pi}\left(\frac{1}{r_1} - \frac{1}{r_4}\right) \tag{2.14}$$

where r_1 = distance from probe number 1 and r_4 = distance from probe number 4. The potentials at probe 2, V_{f2} and at probe 3, V_{f3} can be calculated from relation (2.13) by substituting the proper distances as follows.

$$V_{f2} = \frac{\rho_o I}{2\pi}\left(\frac{1}{S_1} - \frac{1}{S_2 + S_3}\right) \tag{2.15}$$

$$V_{f3} = \frac{\rho_o I}{2\pi}\left(\frac{1}{S_1 + S_2} - \frac{1}{S_3}\right) \tag{2.16}$$

The potential difference V between probes 2 and 3 is

$$V = V_{f2} - V_{f3} = \frac{\rho_0 I}{2\pi}\left(\frac{1}{S_1} + \frac{1}{S_3} - \frac{1}{S_2 + S_3} - \frac{1}{S_1 + S_2}\right) \tag{2.17}$$

and the resistivity ρ_o is computable as

$$\rho_o = \frac{V}{I}\frac{2\pi}{\left(\frac{1}{S_1}+\frac{1}{S_3}-\frac{1}{S_1+S_2}-\frac{1}{S_2+S_3}\right)} \tag{2.18}$$

When the point spacing is equal, that is $S_1 = S_2 = S_3 = S$, the above relation simplifies to

$$\rho_o = \frac{V}{I} 2\pi S \tag{2.19}$$

If the sample is in contact with a non conducting medium, a correction factor G_7 [which is a function (w/S)] is applied to $\rho_{0,}$ in order to obtain the actual resistivity ρ, given by,

$$\rho = \frac{\rho_o}{G_7\left(\frac{w}{S}\right)} \tag{2.20}$$

where,

$$G_7\left(\frac{w}{S}\right) = 1 + 4\frac{S}{w}\sum_{n=1}^{\infty}\left[\frac{1}{\sqrt{\left(\frac{S}{w}\right)^2+(n)^2}} - \frac{1}{\sqrt{\left(\frac{2S}{w}\right)^2+(2n)^2}}\right] \tag{2.21}$$

The function G_7 is tabulated in table [2.1] and plotted in figure 2.19. For smaller values of w/S, the function G_7 approaches the case for an infinitely thin slice, or

$$G_7\left(\frac{w}{S}\right) = \frac{2S}{w}\log_e 2 \tag{2.22}$$

Appropriate values of G_7 corresponding to the required w/S ratio were obtained from the polynomial fit shown in figure 2.19.

Table 2.1: Correction factor G_7 used in resistivity measurement as a function of w/S ratio.

Sl.no.	w/S	G_7(w/S)
1	0.1	13.863
2	0.141	9.704
3	0.2	6.931
4	0.33	4.159
5	0.5	2.78
6	1	1.504
7	1.414	1.223
8	2	1.094
9	3.333	1.0224
10	5	1.007
11	10	1.00045

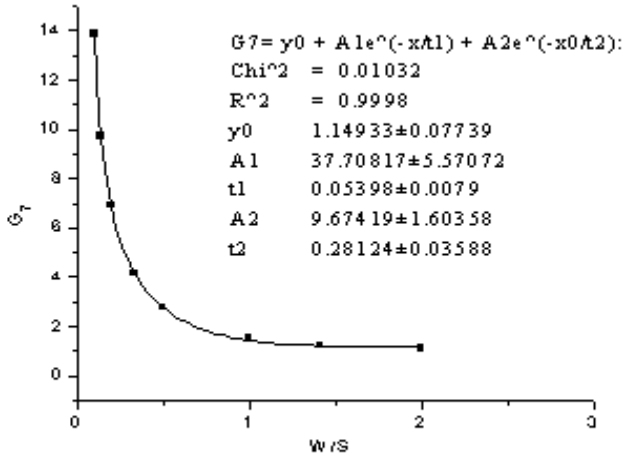

Figure 2.19: Correction factor G_7 as a function of w/s ratio.

For thin film samples, when the thickness of the sample is much less than the probe distances (*i.e.* w ≤ S/2), the thin layers are characterized by their sheet resistance ρ_s.

The sheet resistance is given by,

$$\rho_s = \frac{\rho}{d} = \frac{\pi}{\ln(2)}\frac{V}{I}F = 4.532\left(\frac{V}{I}\right)F \qquad (2.23)$$

where F is a correction factor which depends on the size of the sample and the dimension of probes. When probes are perpendicular to and at a distance w from a non-conducting boundary the correction factor is given as a function of the normalized distance w/S by the relation,

$$F = \frac{1}{1+\frac{1}{1+\frac{2w}{S}}-\frac{1}{2+\frac{2w}{S}}-\frac{1}{4+\frac{2w}{S}}+\frac{1}{5+\frac{2w}{S}}} \qquad (2.24)$$

But when the probe distance from the boundary of the sample is four times probe spacing or more, the correction factor F is reduced to unity. In such a case, the sheet resistance is given by

$$\rho_s = \frac{\rho}{w} = \frac{\pi}{\ln(2)}\frac{V}{I} = 4.532\left(\frac{V}{I}\right) \qquad (2.25)$$

The electrical resistant of the films studied in the present investigations analysed using equation 2.25.

Chapter 3

Studies on bulk and thin films of Pb-Ge-Se glasses

Pb and Se form a solid solution over the entire range of composition and yield the stochiometric compounds PbSe and $PbSe_2$. On the other hand, Ge and Pb do not form a solid solution over the entire composition range. However, the Pb-Ge-Se ternary system shows homogeneous miscibility over a wide range of compositions. Feltz *et al* [160] and Linke *et al* [161] reported the glass forming region in this ternary system along $(PbSe)_a(GeSe)_y(GeSe_2)_{1-a-y}$ tie-lines. The glass compositions studied by them could be grouped into four series, namely,

Series A: $y = 0.65 - a$, where $0.225 < a < 0.50$

Series B: $y = 0.70 - a$, where $0.150 < a < 0.48$

Series C: $y = 0.50 - 0.5\,a$, where $0 < a < 0.067$ and $0.23 < a < 0.46$

Series D: $y = a$, where $0.287 < a < 0.38$

They also reported glass transition temperature, molar volume, thermal expansion, refractive index, optical absorption edge and electrical conductivity of these glasses. The results obtained by them can be summarized as follows: The composition dependence of molar volume, T_g and coefficient of thermal expansion of the four series of glasses was interpreted on the basis of the formation of appropriate structural units as the concentration of the three components in $(PbSe)_a(GeSe)_y(GeSe_2)_{1-a-y}$ system was systematically varied. Their interpretation was consistent with results of the radial distribution function investigations on these glasses [162]. They showed that the Pb atom existed as Pb^{2+} in these glasses. The co-ordination number of Pb^{II} was found to be between three and five. The increase in co-ordination number from three to five is expected to increase the Pb-Se bonding

distance in the co-ordination. The electrical conductivity of the four series of samples increased with an increase in PbSe concentration. On the other hand, the activation energy for electrical conduction decreased with an increase in PbSe component. The optical band gap of Series A and Series B glasses showed very little variation when PbSe percentage was varied. From the above results, a band picture of these amorphous semiconductors was evolved on the following lines.

1. The most probable defects in Ge-Se glasses were taken into account. At thermal equilibrium, it was supposed that the saturated Ge atom interacts with the lone-pair of its neighbouring Se atom and converts it into Se_3^+ state by breaking one of its Ge-Ge bonds. This reaction gives Se_3^+ and Ge_3^- defects. The positive lone-pair interaction energy at Se_3^+ site is overcome by the energy gained in (Ge-Ge)-(Ge-Se) (which amounts to -11.8 kcal.mole^{-1}).
2. Addition of PbSe to these glasses results in the formation of Pb-Se bonds in the glassy state. Pb atom was expected to be in Pb^{2+} configuration. Therefore, Pb atoms would try to tie-up with the Se_3^+ states by converting them into Se_1^- states. The effect of Se_1^- was neglected since the Ge_3^- defects have lower oxidation energy.

The interest in these glasses was regenerated after Tohge *et al* [107] showed that *p*-type to *n*-type conduction change occurs in two series of Pb-Ge-Se glasses, namely, $Pb_xGe_{42-x}Se_{58}$ ($0 \leq x \leq 20$) termed "Series I" and $Pb_{20}Ge_xSe_{80-x}$ ($15 \leq x \leq 24$) termed "Series II" (figure 3.1). In the first series, *p*-type to *n*-type conduction change was observed near 9 at. wt. % of Pb, whereas, in case of second series, the carrier reversal occurred when Ge at. wt. % was about 21 by them. Thermoelectric power and electrical conductivity of $Pb_{20}Ge_xSe_{80-x}$ glasses showed that minimum values at the composition at which the carrier type reversal occurs. The activation

energy for electrical conduction showed a maximum at this composition. It was also noticed from the thermoelectric power measurements that the Seebeck coefficient of series II glasses change its sign from positive to negative near 21 at. wt. % Ge. The change in conduction type in these glasses attributed to the shift of the Fermi energy level towards the conduction band edge rather than to the change in the relative magnitude of electron and hole mobilities. Differential scanning calorimetry [121,130] studies on series II glasses showed that T_g and the activation energy for glass transition exhibited maximum values at the composition at which the *p*- to *n*- type reversal occurs. ΔC_p showed a minimum value near 21 at. wt. %, which was shown as a signature of the formation of a rigid structure at this composition. DSC studies on $Pb_xGe_{42-x}Se_{58}$ glasses [131] showed that T_g and ΔC_p values were minimum near the composition at which the carrier reversal occurred. The Seebeck coefficient values ranged from 0.6 $mV.K^{-1}$ to -0.85 $mV.K^{-1}$ as calculated from the thermoelectric power measurement for glasses with $0 \leq x \leq 20$. They also reported that the variation of electrical resistivity with composition showed a plateau-like character near room temperature. The composition dependence of room temperature resistivity appears to have a slope change at the *p*- to *n*- transition. Composition dependence of density and molar volume of these glasses have been interpreted on the basis of the chemical nature of the constituents. The charge carrier reversal in these glasses has been attributed to changes in the charge defect states induced by the addition of impurity atoms as proposed by Kolobov [64]. Compositional dependence of thermal diffusivity of series I and II glasses showed [135] a minimum at the *p*- to *n*- transition which has also been interpreted in terms of Kolobov's model. $Pb_7Ge_{35}Se_{58}$, $Pb_8Ge_{34}Se_{58}$ and $Pb_9Ge_{33}Se_{58}$ thin amorphous have been prepared [134]. The field dependence of electrical conductivity of these thin film of Pb-Ge-Se glasses have

been analysed in the light of the Poole-Frenkel effect (*PFE suggests that charge carrier can be created by ionization of impurity states*).

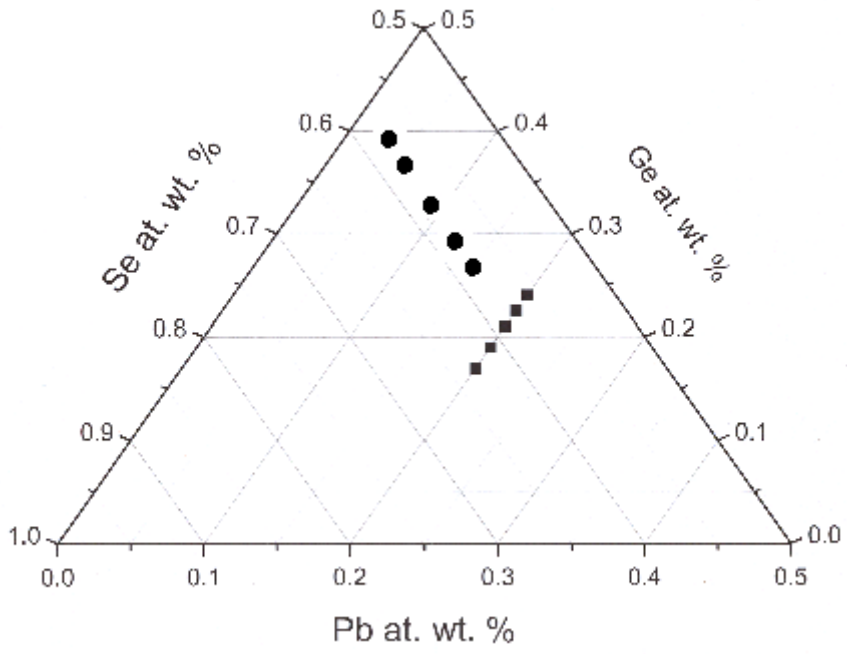

Figure 3.1: Ternary plot showing the two series of Pb-Ge-Se glasses in which *p*- to *n*- transition was observed.

3.1. Sample preparation and characterisation

In the current investigations, bulk samples of $Pb_xGe_{42-x}Se_{58}$ series of glasses with x = 3, 6, 9, 13, 15 and $Pb_{20}Ge_xSe_{80-x}$ glasses with x = 17, 19, 21, 22.5, 24 were prepared by the melt quenching technique discussed in chapter 2. In order to ensure similar quenching conditions for all the glass samples, the following precautions were taken: The total weight of the mixture was maintained at 5 gm., the melt was allowed to homogenize for 10 hours at 1000º C and quenched in ice-cold water containing NaCl. The amorphous nature of the as-quenched glasses was verified by XRD. A typical XRD pattern of Pb modified Ge-Se glass is shown in figure 3.2. The XRD patterns of the glasses revealed that the samples were amorphous with no crystalline peak within the scan range of $10º < 2\theta < 70º$. The majority charge

carrier type in the bulk samples was determined by TEP measurements. These measurements revealed that $Pb_3Ge_{39}Se_{58}$, $Pb_6Ge_{36}Se_{58}$, $Pb_{20}Ge_{17}Se_{63}$ and $Pb_{20}Ge_{19}Se_{61}$ glass compositions were *p*-type and the rest were *n*-type semiconductors. A DSC was employed to verify the occurrence of the glass transition under a constant heating rate of 10 $^{\circ}C.min^{-1}$. All the samples showed a single glass transition temperature (T_g) within the temperature range of 490 K to 550 K at this heating rate.

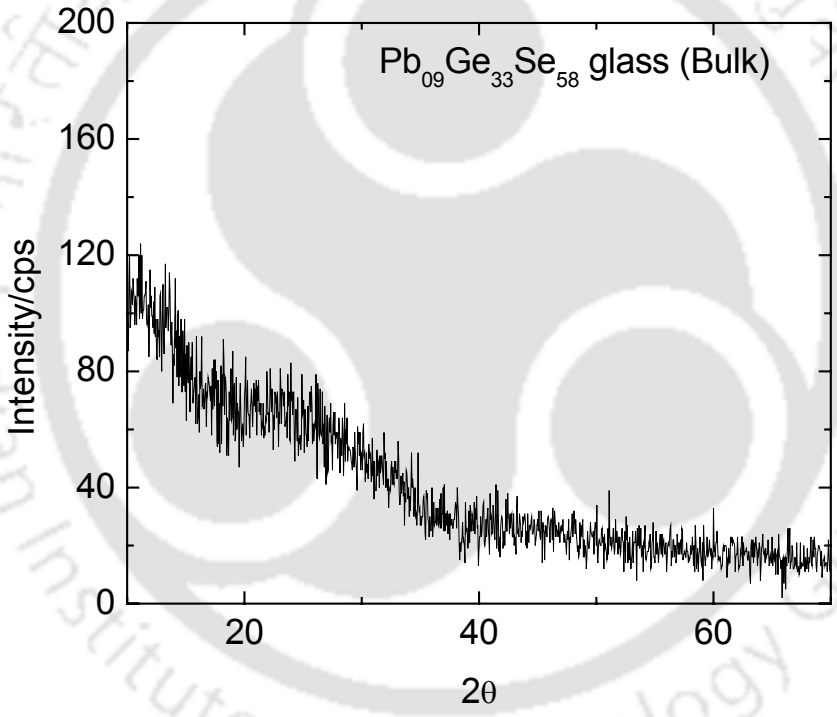

Figure 3.2: A typical XRD pattern of a bulk Pb-Ge-Se glass.

Thin film samples of both the series of Pb-Ge-Se glasses were prepared by thermal evaporation of bulk glasses using the apparatus described in chapter 2. Powdered bulk glass samples weighing ~ 0.5 gm were evaporated from molybdenum evaporation boats. The films were deposited on cleaned glass substrates (microscope cover slips) by passing a current of 200 A through the

molybdenum boat for about 3-5 minute duration. A source shutter was used to prevent deposition until the evaporation boat reached the desired temperature. The amorphous nature of the as-deposited thin films was verified using an X-ray diffractometer equipped with the grazing incidence device. A typical x-ray diffractogram of a Pb-Ge-Se film on glass substrate is shown in the figure 3.3. The XRD pattern of all the thin film samples showed that they were perfectly amorphous. Thickness of the deposited films was measured with the help of an ellipsometer. Films with a wide variety of thicknesses ranging between 1500 Å to 5000 Å were prepared. Although a quartz crystal monitor was available for *in-situ* thickness measurement during deposition, calibration of these monitors could not be done satisfactorily due to the lack of acoustic impedance data of the glass samples. As a result, the deposition procedure had to standarised by controlling the pressure in the chamber, weight of the source used, heater current and deposition time. With such precautions films with thickness within 2000 ± 200 Å could be prepared. Compositions of individual samples was analysed using a SEM-EDX. The composition of each sample was found to be identical to the bulk samples used for deposition with an uncertainty of ± 2 %.

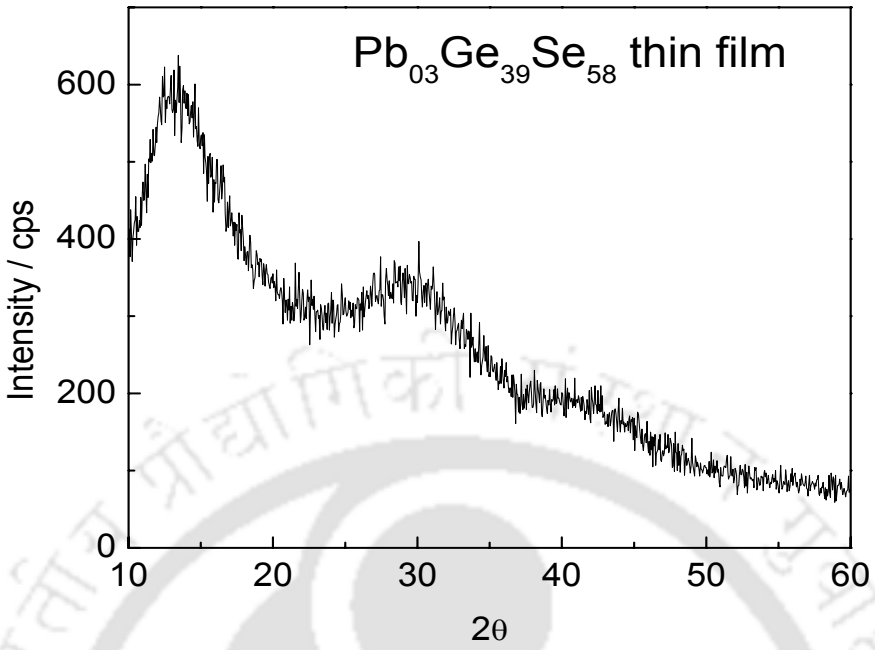

Figure 3.3: A typical diffractogram of a Pb-Ge-Se thin film obtained using the grazing incidence device.

3.2. Differential scanning calorimeter studies

DSC studies on $Pb_xGe_{42-x}Se_{58}$ ($3 \leq x \leq 15$) glasses and $Pb_{20}Ge_xSe_{80-x}$ ($17 \leq x \leq 24$) glasses were performed following the procedure explained in chapter 2. The experiments were performed with ~ 20 mg samples. The DSC curves were recorded over a temperature range of 323 K to 723 K for different heating rates such as 10 °C.min^{-1}, 15 °C.min^{-1}, 20 °C.min^{-1} and 25 °C.min^{-1}. Figure 3.4 shows the DSC curves obtained for Pb-Ge-Se glasses under a constant heating rate of 10 °C.min^{-1}.

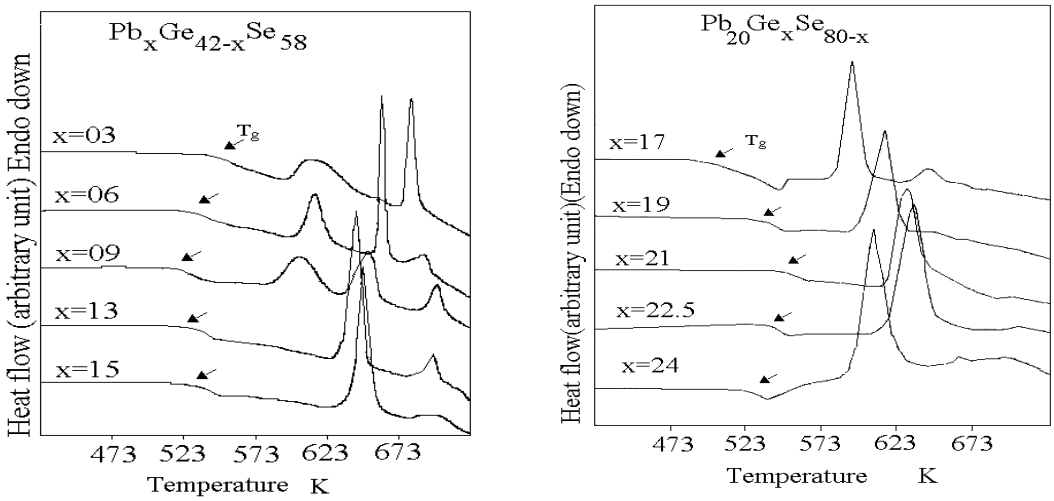

Figure 3.4: DSC curves of Pb-Ge-Se glasses recorded at a heating rate of 10 °C.min^{-1}.

All glasses exhibited a glass transition temperature (T_g) marked by a distinct endothermic baseline shift. T_g was observed in the temperature range from 495 K to 545 K for both $Pb_xGe_{42-x}Se_{58}$ (series I) and $Pb_{20}Ge_xSe_{80-x}$ (series II) glasses when heated at 10 °C.min^{-1}. On heating beyond the glass transition temperature, the glass samples exhibited either a single crystallization peak or multiple crystallization peaks. Multiple crystallization peaks signify the devitrification of different crystalline phases in the multicomponent glasses. Glass transition temperature (T_g) and crystallisation temperature (T_c) obtained under a constant heating rate of 10 °C.min^{-1} are tabulated in the table 3.1. Earlier reports on T_g and T_c of series I [131] and series II [122,130] glasses are given in within parenthesis. It can be seen that both the present and reported data showed the same trend. Minor differences in the T_g and T_c values are due to variation in preparation conditions.

Table 3.1: Glass transition temperature (T_g) and first crystallisation temperature (T_c) of Pb-Ge-Se glasses obtained when heated at 10 °C.min^{-1}. Data taken for [131] and [120,130] are given in the brackets.

Sample composition	T_g (K)	T_c (K)	Sample composition	T_g (K)	T_c (K)
$Pb_{03}Ge_{39}Se_{58}$	544 ± 1 (---)	616 ± 1 (---)	$Pb_{20}Ge_{17}Se_{63}$	498 ± 1 (505)	594 ± 1 (628)
$Pb_{05}Ge_{37}Se_{58}$	--- (520)	--- (711)	$Pb_{20}Ge_{19}Se_{61}$	533 ± 1 (537)	615 ± 1 (656)
$Pb_{06}Ge_{36}Se_{58}$	527 ± 1 (---)	615 ± 1 (---)	$Pb_{20}Ge_{21}Se_{59}$	544 ± 1 (556)	629 ± 1 (673)
$Pb_{09}Ge_{33}Se_{58}$	524 ± 1 (---)	604 ± 1 (---)	$Pb_{20}Ge_{22.5}Se_{57.5}$	535 ± 1 (---)	624 ± 1 (---)
$Pb_{10}Ge_{32}Se_{58}$	--- (530)	--- (667)	$Pb_{20}Ge_{23}Se_{57}$	--- (536)	--- (679)
$Pb_{13}Ge_{29}Se_{58}$	527 ± 1 (---)	644 ± 1 (---)	$Pb_{20}Ge_{24}Se_{56}$	524 ± 1 (530)	608 ± 1 (653)
$Pb_{15}Ge_{27}Se_{58}$	528 ± 1 (537)	648 ± 1 (658)			

The variation of glass transition temperature T_g with composition (x) for both the series of glasses is shown in figure 3.5. T_g of series I glasses decreases with the addition of Pb and attains a minimum value for x = 9 at. wt. % Pb. Beyond x = 9 at. wt. % Pb, there is not much variation in T_g with further addition of Pb. T_g is an bond sensitive property. The variation of T_g with composition can be understood on the basis of the variation in average bond energy of these glasses. It can be seen from figure 3.5 that T_g of series I glasses decreases with increase in Pb content. As Pb replaces Ge, the number of Ge-Se bonds decreases and the number Pb-Se bonds increases. The single bond energy of Pb-Se is lower than Ge-Se (Appendix I). Hence, the average bond energy of the glasses decrease as Pb content is increased in Series I. In the case of Series II, T_g increases with the addition of Ge, attains a maximum value at 21 at. wt. % of Ge and then decreases. In this series the Pb content remains constant, whereas, Se atoms are gradually replaced by Ge atoms. Tohge *et al* [107] counted the number Ge-Se, Ge-Ge and Se-Se bonds in various compositions of $Pb_{20}Ge_xSe_{80-x}$ glasses. Their calculations were based on the COCN model with the assumption that Ge and Se atoms bond with four and two other atoms, respectively, and that heteronuclear bonds are favoured over homonuclear bonds. Figure 3.6 shows the results obtained from their calculations. From the figure

it is clear than Ge-Se bonds are maximum in number when Ge at. wt. % is 20. On the other hand, Se-Se bonds start decreasing and vanish at 20 at. wt. % Ge and Ge-Ge bonds start appearing after 20 at. wt. % Ge. Accordingly, the average bond energy of the glasses start increasing with addition of Ge, attains a maximum value near 21 at. wt. % of Ge and then decreases in this series of glasses. Since T_g depends on the average bond energy of the glass, it shows a maximum at 21 at. wt. % Ge.

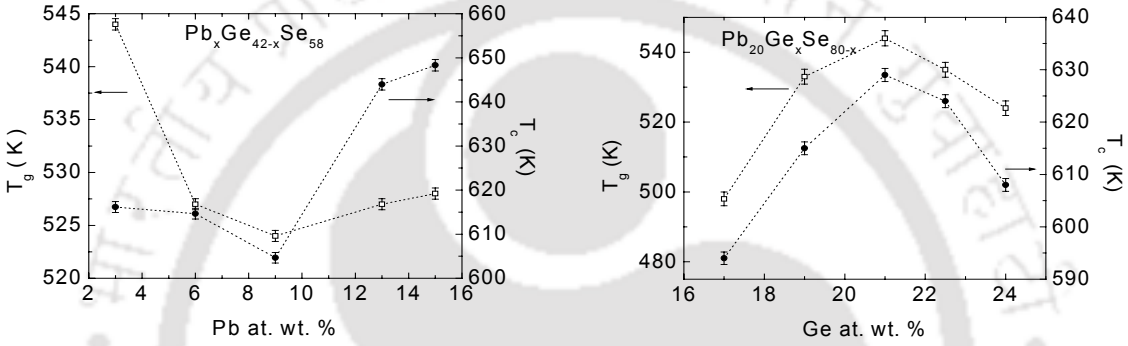

Figure 3.5: Variation of T_g and T_c with composition x for bulk Pb-Ge-Se glasses. Data correspond to DSC runs performed at 10 °C.min^{-1}.

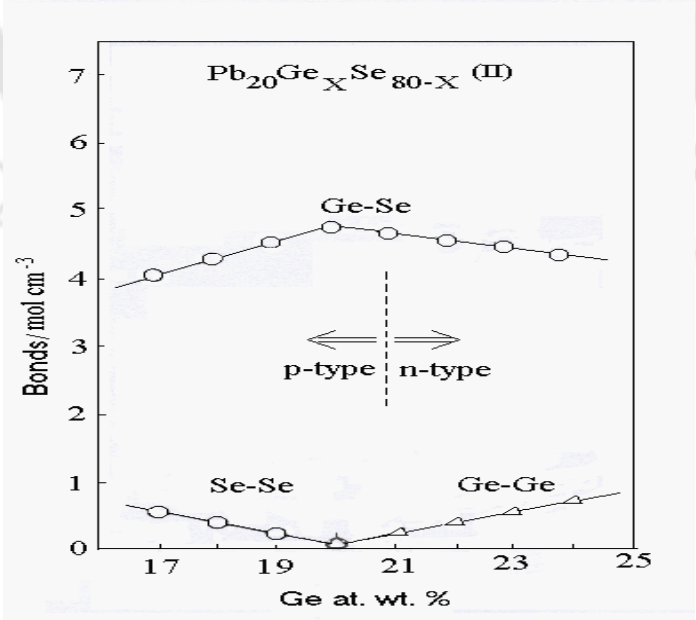

Figure 3.6: Bond statistics in Pb-Ge-Se glasses [107].

The crystallization temperature T_c corresponding to the first crystallization exotherm for the two series of Pb-Ge-Se glasses is shown in figure 3.5. T_c shows a maximum at 21 at. wt. % of Ge for series II glasses and minimum at 9 at. wt. % of Pb for Series I. These results are consistent with those reported on Series I [131] and Series II [121] glasses. A higher T_c signifies a relatively stronger inhibition to the nucleation and growth of the crystalline phase. If one assumes that the first exotherm corresponds to the same crystalline phase in the case of all the glasses, then one can say that the glass compositions at x = 9 at. wt. % Pb (Series I) and x = 21 at. wt. Ge (Series II) exhibit the highest inhibition to crystallization. Closely spaced crystallizations such as the ones exhibited by these glasses makes the task of identifying each phase crystallizing at their respective T_cs by XRD very difficult. The reason for this is annealing the glass sample at the first crystallization temperature invariable results in partial crystallization of the adjacent phases, thereby, hindering individual identification of the crystallised phases. It is not possible to compare the T_c of other exotherms since all glasses do not exhibit the same number of crystalline exotherms.

Kissinger's and Thakor's relations (equation 2.1 and 2.2) were used for estimating the activation energy for the glass transition of various glass compositions using the procedure described in chapter 2. The activation energy obtained for glass transition E_K (Kissinger) and E_T (Thakor) obtained for the two series of Pb-Ge-Se glasses have been plotted in figure 3.7 and 3.8. From figure 3.7 and figure 3.8, it can be seen that E_K and E_T for both the series of glasses show a minimum value at the composition at which the *p*- to *n*- transition was observed. As the activation energy is a measure of the resistance imposed by the glassy network for the glass-supercooled liquid transition, one can say that the glass-supercooled liquid transition

is least hindered for the compositions with 9 at. wt % of Pb in Series I and 21 at. wt. % of Ge in Series II glasses.

The activation energy for viscous flow E_η has been estimated using relation 2.3. E_η values of Pb-Ge-Se samples are tabulated in table 3.3, together with the degree of fragility m calculated using relation 2.9. Both E_η and m show minimum values at the compositions at which the *p*- to *n*- type transition was observed. From the value of m, these glasses can be classified as kinetically strong (KS). Such KS behaviour is normally exhibited by network glasses such as chalcogenides (Ge_8Se_{92}, $Ge_{12}Se_{88}$, $Ge_{15}Te_{85}$, Se) [163].

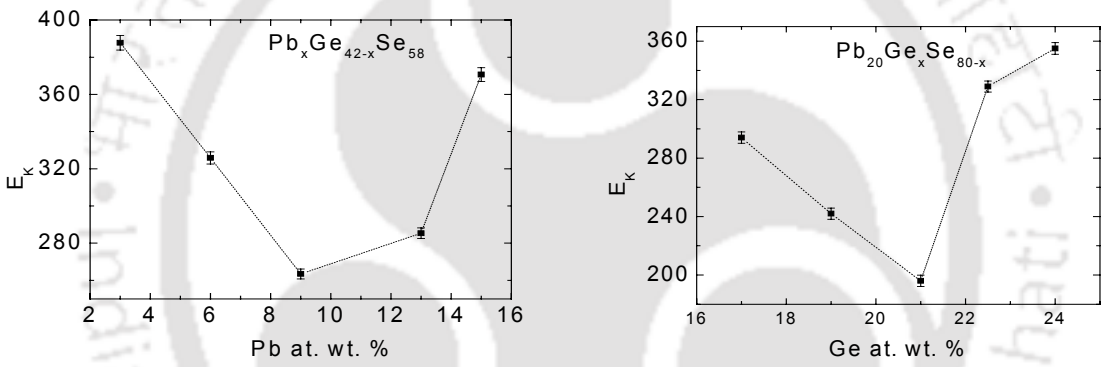

Figure 3.7: Variation of activation energy E_K for glass transition with composition for Pb-Ge-Se glasses.

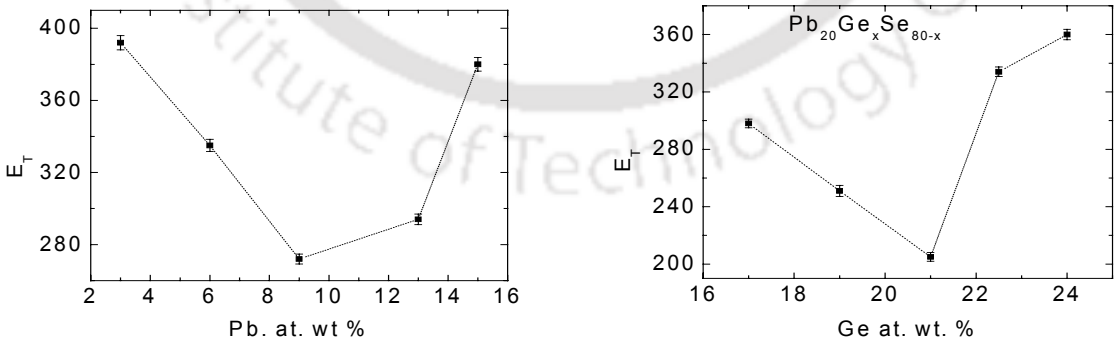

Figure 3.8: Variation of activation energy E_T for glass transition with composition for Pb-Ge-Se glasses.

Table: 3.2: Activation energy for glass transition (E_K and E_T) of Pb-Ge-Se glasses.

Sample composition	E_K (kJ.mol^{-1})	E_T (kJ.mol-1)	Sample composition	E_K (kJ.mol^{-1})	E_T (kJ.mol-1)
$Pb_{03}Ge_{39}Se_{58}$	388 ± 4	392 ± 2	$Pb_{20}Ge_{17}Se_{63}$	294 ± 3	298 ± 2
$Pb_{06}Ge_{36}Se_{58}$	326 ± 3	335 ± 2	$Pb_{20}Ge_{19}Se_{61}$	242 ± 2	251 ± 2
$Pb_{09}Ge_{33}Se_{58}$	263 ± 3	272 ± 2	$Pb_{20}Ge_{21}Se_{59}$	196 ± 2	205 ± 2
$Pb_{13}Ge_{29}Se_{58}$	285 ± 3	294 ± 2	$Pb_{20}Ge_{22.5}Se_{57.5}$	330 ± 3	334 ± 2
$Pb_{15}Ge_{27}Se_{58}$	371 ± 4	380 ± 2	$Pb_{20}Ge_{24}Se_{56}$	355 ± 4	360 ± 2

Figure 3.9 shows the composition dependence of the excess heat capacity at T_g (ΔC_p) of Pb-Ge-Se glasses belonging to Series I and Series II. The present data could be interpreted in terms of the thermodynamic fragility behaviour [16] already discussed at length in the first chapter. As shown in the figure, ΔC_p shows a minimum at the MCCR composition in the case of Series I as well as Series II glasses. Minimum ΔC_p could be correlated with minimum thermodynamic fragility [or maximum thermodynamically strong (TS) nature] of this glass composition with respect to the rest in the respective series. Since ΔC_p is a representation of the configurational entropy frozen in during the glass formation, the minimum ΔC_p signifies minimum configurational change at the glass-supercooled liquid transition for the glass in question.

Table 3.3: Excess heat capacity and degree of fragility (m) of the Pb-Ge-Se glasses.

Sample composition	ΔC_p (JK-1mol-1)	E_η (kJ.mol^{-1})	m	Sample composition	ΔC_p (JK-1mol-1)	E_η (kJ.mol^{-1})	m
$Pb_{03}Ge_{39}Se_{58}$	31.0 ± 0.3	392	38	$Pb_{20}Ge_{17}Se_{63}$	37.6 ± 0.4	294	31
$Pb_{06}Ge_{36}Se_{58}$	25.9 ± 0.3	335	34	$Pb_{20}Ge_{19}Se_{61}$	35.0 ± 0.3	242	25
$Pb_{09}Ge_{33}Se_{58}$	20.5 ± 0.2	272	27	$Pb_{20}Ge_{21}Se_{59}$	22.2 ± 0.2	196	20
$Pb_{13}Ge_{29}Se_{58}$	27.8 ± 0.3	294	29	$Pb_{20}Ge_{22.5}Se_{57.5}$	32.6 ± 0.3	330	32
$Pb_{15}Ge_{27}Se_{58}$	30.4 ± 0.3	380	38	$Pb_{20}Ge_{24}Se_{56}$	40.7 ± 0.4	355	36

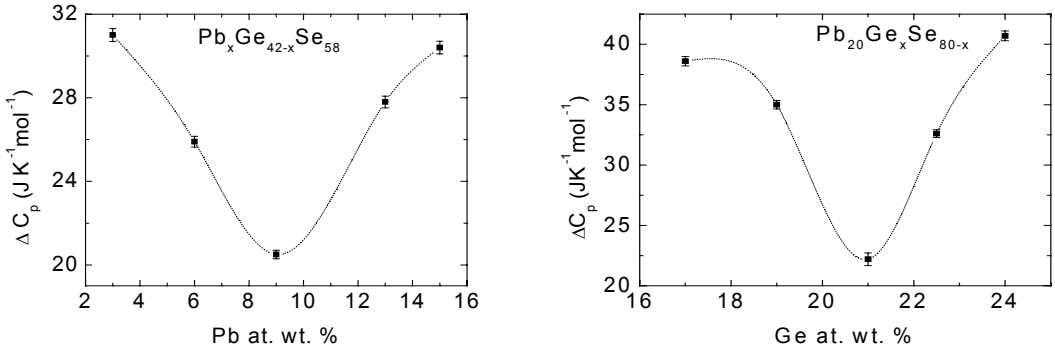

Figure 3.9: Variation of excess heat capacity at T_g (ΔC_p) with composition for Pb-Ge-Se glasses.

Degree of fragility m and ΔC_p variations indicate that the composition at which *p*-type to *n*- type transition (MCCR) occurs are characterized by KS-TS behaviour. ΔC_p values of $Pb_xGe_{42-x}Se_{58}$ glass and $Pb_{20}Ge_xSe_{80-x}$ [121] reported earlier are also shown in table 3.3 along with the present data. The high values obtained in the present work is due to the different thermal history of the glasses. In the earlier work, the samples were annealed at T_g before the ΔC_p measurement. Annealing at T_g and cooling back results in a reduction in the configurational entropy frozen in doing the glass formation. Hence their ΔC_p values are lower than the present data. However it is obvious that both the sets of data show the same type of dependence with variation in composition. There is no rigid rule about the procedure, for obtaining ΔC_p. In this work as-quenched glasses were used without annealing in all DSC studies in order to obtain consistent results.

3.3. Thermoelectric power

The Seebeck coefficient (Q) was calculated for the two series of Pb-Ge-Se glasses according to the procedure mentioned in chapter 2. Q values at 348 K are tabulated in table 3.4 and the variation of Q with composition is shown in figure 3.10. The temperature dependence of the Seebeck coefficient (Q) for individual glass samples in the range of 313 K to 413 K is shown in figure 3.11. From the slope

of the least squares fit of the corresponding plots, the activation energy (E_s) for each glass composition was calculated. The values are tabulated in table 3.4 and shown in the figure 3.12. The Q values of $Pb_xGe_{42-x}Se_{58}$ glasses given within parentheses have been reported by Vaidhyanathan *et al* [131] at 373 K, whereas, those given in parentheses along with $Pb_{20}Ge_xSe_{80-x}$ glasses are the values reported by Tohge *et al* [107] at 348 K. The data taken from the literature shows the same trend as the ones obtained in the present work.

For thermoelectric power measurements on the thin film samples, the set up described in chapter 2 was used. The Seebeck coefficient (Q) was calculated at 348 K. The variation of Seebeck coefficient with composition and the temperature dependence of the Seebeck coefficient between 313 K to 383 K are shown in the figure 3.13 and figure 3.14 respectively. The activation energy for the thermoelectric power (E_s) calculated and tabulated in table 3.5. The variation of E_s with the composition is shown in figure 3.15. The sign of the Seebeck coefficient (Q) was found to be positive for $Pb_3Ge_{39}Se_{58}$, $Pb_6Ge_{36}Se_{58}$, $Pb_9Ge_{33}Se_{58}$, $Pb_{20}Ge_{17}Se_{63}$, $Pb_{20}Ge_{19}Se_{61}$, whereas, the rest of the glass composition showed negative Seebeck coefficient.

Table 3.4: Seebeck coefficient and activation energy for thermo electric power of $Pb_xGe_{42-x}Se_{58}$ and $Pb_{20}Ge_xSe_{80-x}$ bulk glasses.

Sample composition	Q ($mV.K^{-1}$)	E_s (eV)	Sample composition	Q ($mV.K^{-1}$)	E_s (eV)
$Pb_{03}Ge_{39}Se_{58}$	0.47 ± 0.02 (---)	0.62 ± 0.04 (---)	$Pb_{20}Ge_{17}Se_{63}$	1.15 ± 0.04 (1.7)	1.41 ± 0.03
$Pb_{05}Ge_{37}Se_{58}$	--- (0.10)	---(0.86)	$Pb_{20}Ge_{19}Se_{61}$	0.82 ± 0.03 (1.0)	1.26 ± 0.03
$Pb_{06}Ge_{36}Se_{58}$	0.27 ± 0.01 (---)	0.47 ± 0.03 (---)	$Pb_{20}Ge_{21}Se_{59}$	-0.70 ± 0.03 (---)	0.65 ± 0.03
$Pb_{09}Ge_{33}Se_{58}$	-0.14 ± 0.01 (---)	0.12 ± 0.01 (---)	$Pb_{20}Ge_{22}Se_{58}$	--- (-0.8)	---
$Pb_{10}Ge_{32}Se_{58}$	-- (-0.25)	--- (0.76)	$Pb_{20}Ge_{22.5}Se_{57.5}$	-1.15 ± 0.04 (---)	1.17 ± 0.04
$Pb_{13}Ge_{29}Se_{58}$	-0.44 ± 0.02 (---)	0.58 ± 0.03 (---)	$Pb_{20}Ge_{23}Se_{57}$	-- (-0.78)	---
$Pb_{15}Ge_{27}Se_{58}$	-0.65 ± 0.03 (0.44)	1.01 ± 0.05 (0.73)	$Pb_{20}Ge_{24}Se_{56}$	-1.23 ± 0.04 (0.9)	1.27 ± 0.04

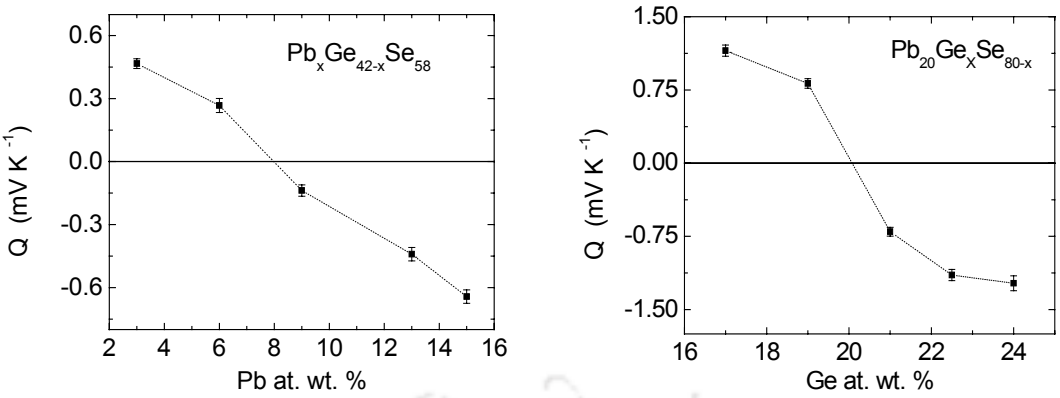

Figure 3.10: Variation of Seebeck coefficient with composition of bulk Pb-Ge-Se glasses at 348 K.

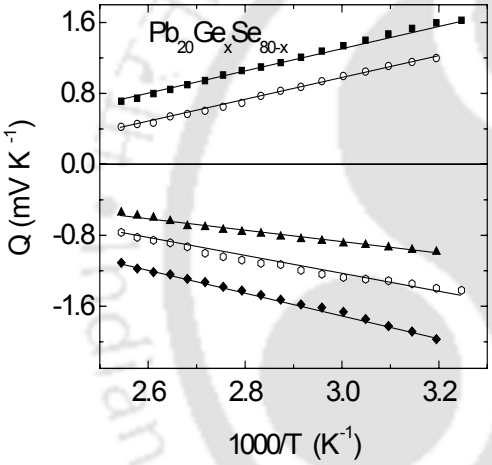

Figure 3.11: Temperature dependence of Seebeck coefficient of bulk Pb-Ge-Se glass.

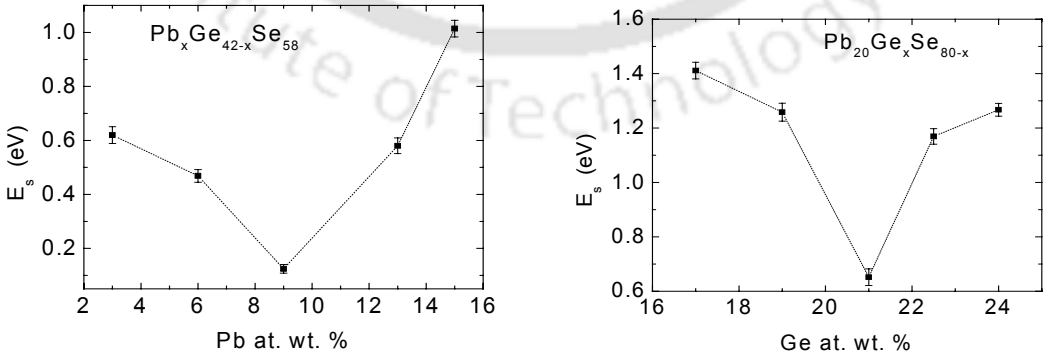

Figure 3.12: Variation of activation energy for thermoelectric power with composition.

Table 3.5: Seebeck coefficient and activation energy for $Pb_xGe_{42-x}Se_{58}$ for thermal conduction in thin films.

Sample composition	Q (mV. K^{-1})	E_s (eV)	Sample composition	Q (mV. K^{-1})	E_s (eV)
$Pb_{03}Ge_{39}Se_{58}$	1.34 ± 0.04	1.02 ± 0.03	$Pb_{20}Ge_{17}Se_{63}$	1.67 ± 0.05	1.15 ± 0.03
$Pb_{06}Ge_{36}Se_{58}$	1.04 ± 0.04	0.88 ± 0.03	$Pb_{20}Ge_{19}Se_{61}$	1.41 ± 0.04	1.08 ± 0.03
$Pb_{09}Ge_{33}Se_{58}$	0.67 ± 0.02	0.76 ± 0.03	$Pb_{20}Ge_{21}Se_{59}$	-1.36 ± 0.04	0.89 ± 0.03
$Pb_{13}Ge_{29}Se_{58}$	-1.34 ± 0.04	0.87 ± 0.03	$Pb_{20}Ge_{22.5}Se_{57.5}$	-1.71 ± 0.05	1.14 ± 0.03
$Pb_{15}Ge_{27}Se_{58}$	-1.79 ± 0.05	1.09 ± 0.03	$Pb_{20}Ge_{24}Se_{56}$	-1.99 ± 0.06	1.27 ± 0.03

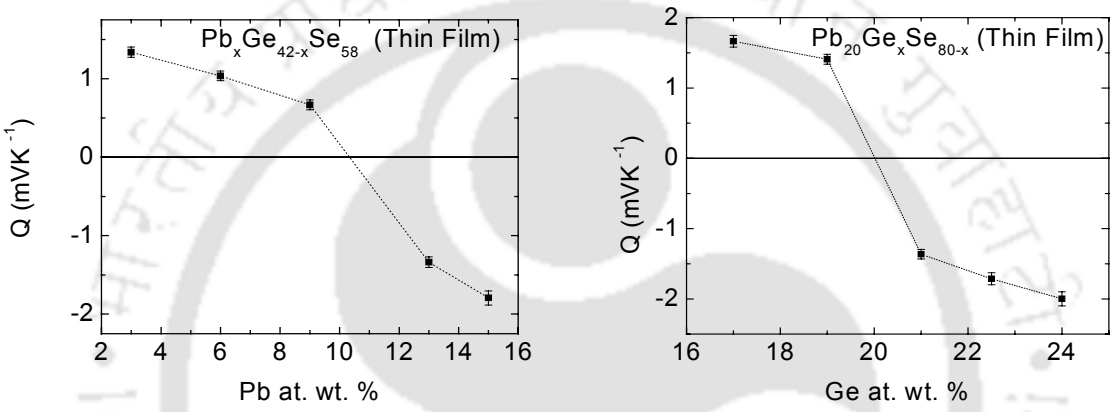

Figure 3.13: Variation of Q with composition in Pb-Ge-Se thin films

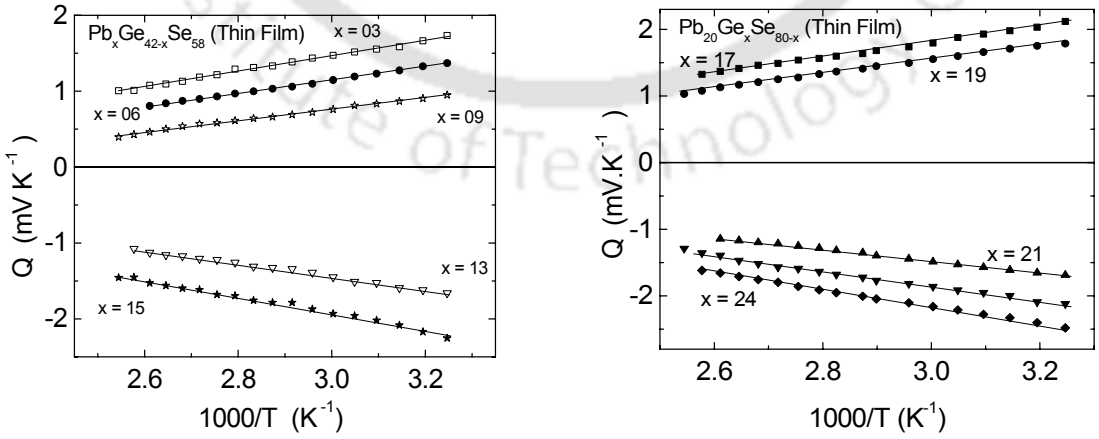

Figure 3.14: Temperature dependence of Seebeck coefficient of Pb-Ge-Se thin films

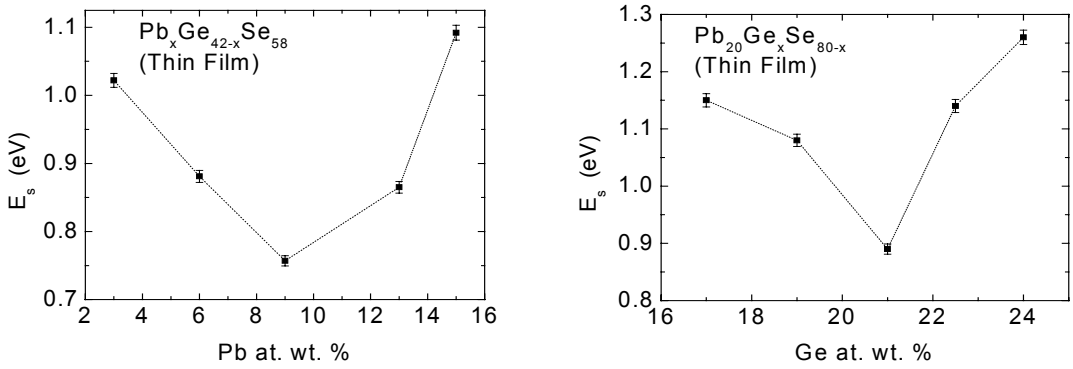

Figure 3.15: Variation of activation energy (E_S) for TEP of Pb-Ge-Se thin films as a function of composition.

The carrier sign reversal phenomenon in Pb-Ge-Se glass can be interpreted in terms of Kolobov's [64] proposal of modifications in defect states with the addition of Pb. In the case of Selenium, the triply and singly co-coordinated defect states are Se_3^+ and Se_1^-, respectively. One can consider Se_3^+ as a hole-bearing atom. X-ray studies have confirmed [162] that Pb exists as Pb^{2+} in lead chalcogenide glasses. On addition of Pb to Ge-Se glasses, Pb^{2+} converts some Se_3^+ into Se_1^-, whereas, the number of Ge_3^- remains unaffected. As the number of Se_3^+ decreases, the number of holes generated at the time of thermal excitation also decreases. Simultaneously, the number of negative charge defect states Se_1^- increases. This results in the reduction of hole generating (triply co-ordinated and positively charged) defect states and at the same time increases the number of electron generating (singly co-ordinated and negatively charged) defect states. This disturbance in the concentration of the VAPs culminates in the unpinning of the Fermi level and shifts it towards the conduction band. In this manner, one can account for the *p*- to *n*-type transition observed in these glasses with the addition of Pb. SEM studies on Pb-Ge-Se glasses do not show any noticeable inhomogeneities even at sub-micron scales. This observation does not support the idea of percolation of microcrystalline clusters

as a plausible model for the conduction type change in these glasses. In the case of $Pb_{20}Ge_xSe_{80-x}$ (series II) glasses, Pb concentration remains constant, whereas, Ge atoms gradually replace Se atom. The effect of Pb in suppressing Se_3^+ defect states has already been discussed. When Ge replaces Se, Ge_3^- states increase in number, gradually depleting Se_3^+. Effectively, the positive charged defect state responsible for the generation of holes reduces in number, resulting in the alternation of charge defect states. This unpins the Fermi level and shifts it towards the conduction band.

It is interesting to note that in thin film of series I glasses, $Pb_{09}Ge_{33}Se_{58}$ glass showed *p*- type conduction whereas the corresponding bulk composition showed *n*-type conduction. This observation suggests that a large number of dangling bonds (VAP) are present in the thin film as compared to the bulk glass. More Pb^{2+} concentration is required to suppress the Se_3^+ states. This argument is also supported by the higher Q values exhibited the thin film samples.

3. 4. Electrical conductivity

d. c. electrical conductivity data of bulk Pb-Ge-Se glasses was recorded from 348 K to 425 K and for the thin films from 313 K to 400 K. The electrical resistivity of the bulk samples and thin films at 348 K is tabulated in the table 3.6 and table 3.7, respectively. For the $Pb_{20}Ge_xSe_{80-x}$ series of glasses, resistivity values reported at 398 K by Tohge *et al* [107] has been incorporated in table 3.6. The conductivity data in the temperature range of 345 K to 425 K could be fitted to equation 1.15. The ln (σ) versus 1000/T plots for all the glasses are shown in figure 3.16 and figure 3.17. The activation energy for electrical conduction (E_σ) calculated from the slope of ln (σ) versus 1000/T curves is tabulated in table 3.6. The variation of the E_σ with composition is shown in figure 3.21. The linearity of the ln (σ) versus 1000/T over the temperature range of study confirms that the electronic conduction is due to a single

conduction mechanism namely, band transport mechanism, in which the electron in the extended state behaves as a conduction electron. The electrical resistivity measured at 398 K for each bulk glass composition is tabulated in table 3.6 along with the E_σ values. $Pb_xGe_{42-x}Se_{58}$ data published earlier [131] is shown in brackets in column 2 and 3 of table 3.6. $Pb_{20}Ge_xSe_{80-x}$ glass data reported [107] is also shown in the table. It has to be noted that Vaidhyanathan et al data shown in table 3.6 correspond to 300 K. The exponential nature of the resistivity data results in lower ρ values at higher temperatures. At 300 K, the variations in resistivity value between compositions is higher compound to the variations at 398 K, which explains the difference between the present and published data. The higher electrical conductivity of the thin films is a consequence of the dimensionality effect. Resistivity (ρ) and E_σ of both bulk and thin films of series II glasses show the same type of variation with compositions. In the case of series I glasses, although ρ and E_σ of both bulk and thin film sample decreases with increasing Pb content. There is a subtle difference in their respective behaviour as shown in figure 3.18 and 3.19. Vaidhyanathan *et al* [131] have pointed out a slope change in ρ at the composition at which the *p*- to *n*-type transition occurs in $Pb_xGe_{42-x}Se_{58}$ glasses. Similar feature is also seen in figure 3.18. Further in the case of ρ_s of thin films of $Pb_xGe_{42-x}Se_{58}$, the carrier change was observed after 9 at. wt. % .

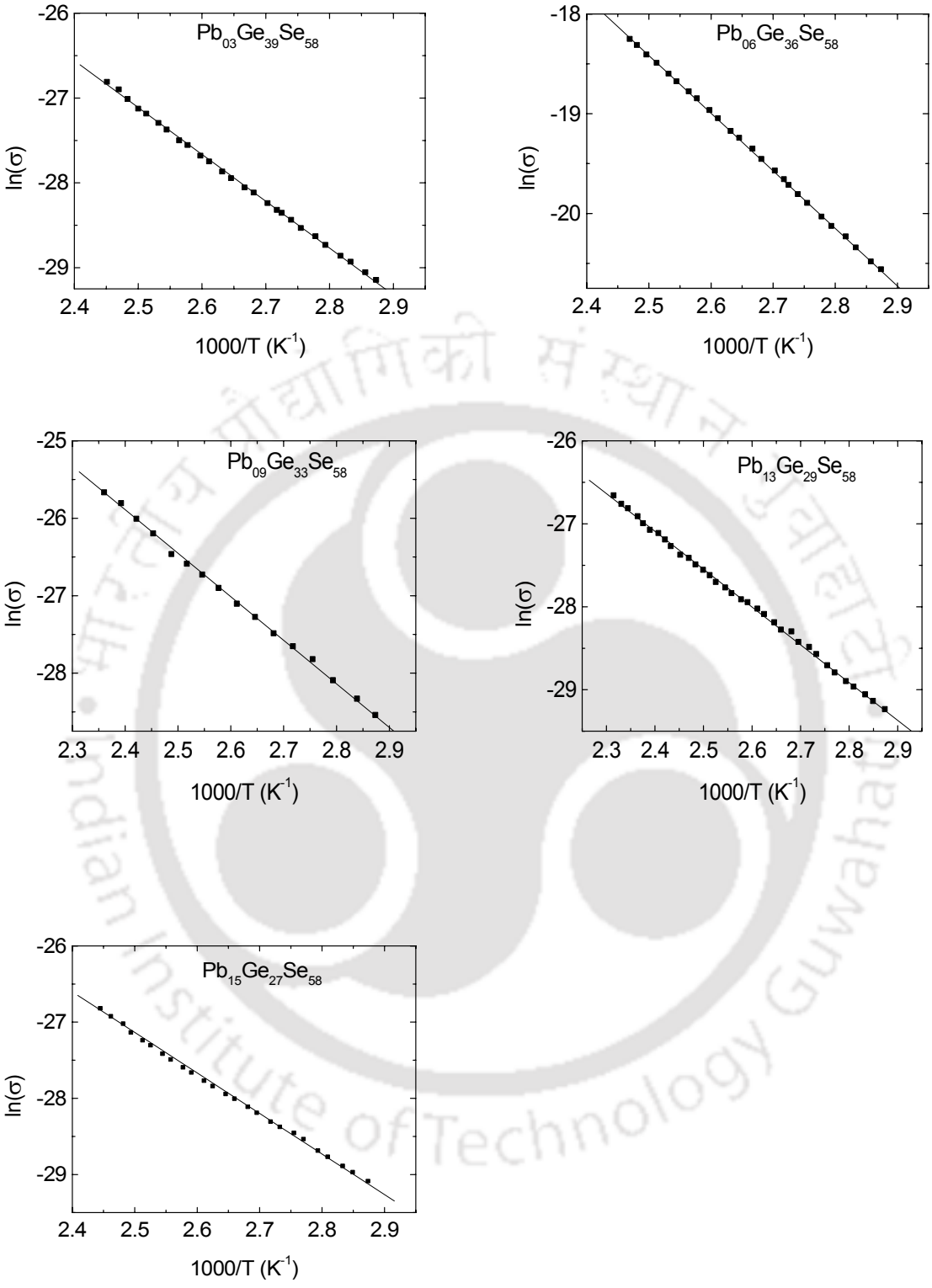

Figure 3.16: ln (σ) versus 1000/T plots of bulk Pb-Ge-Se glasses.

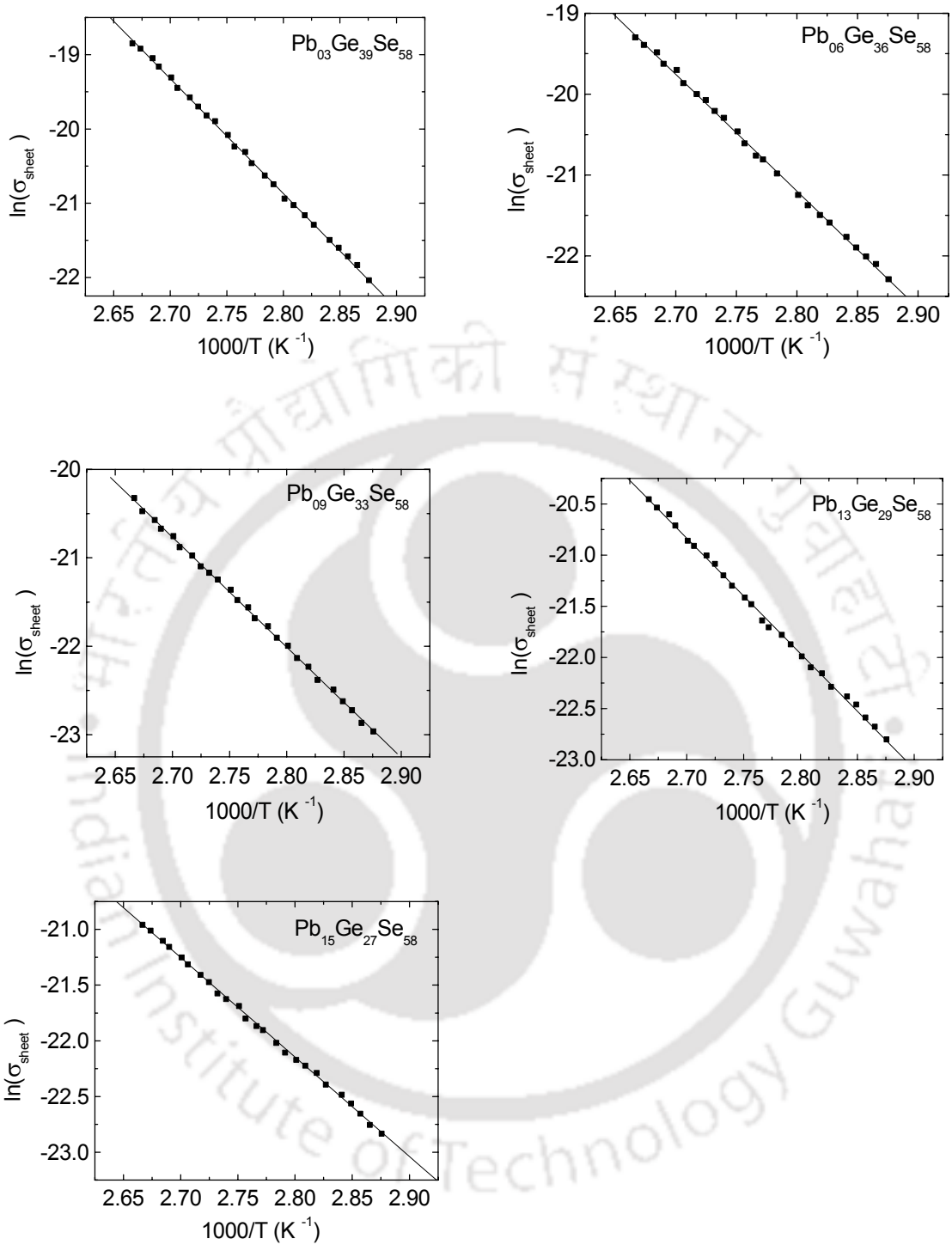

Figure 3.17a: ln (σ) versus 1000/T plots of $Pb_xGe_{42-x}Se_{58}$ thin films

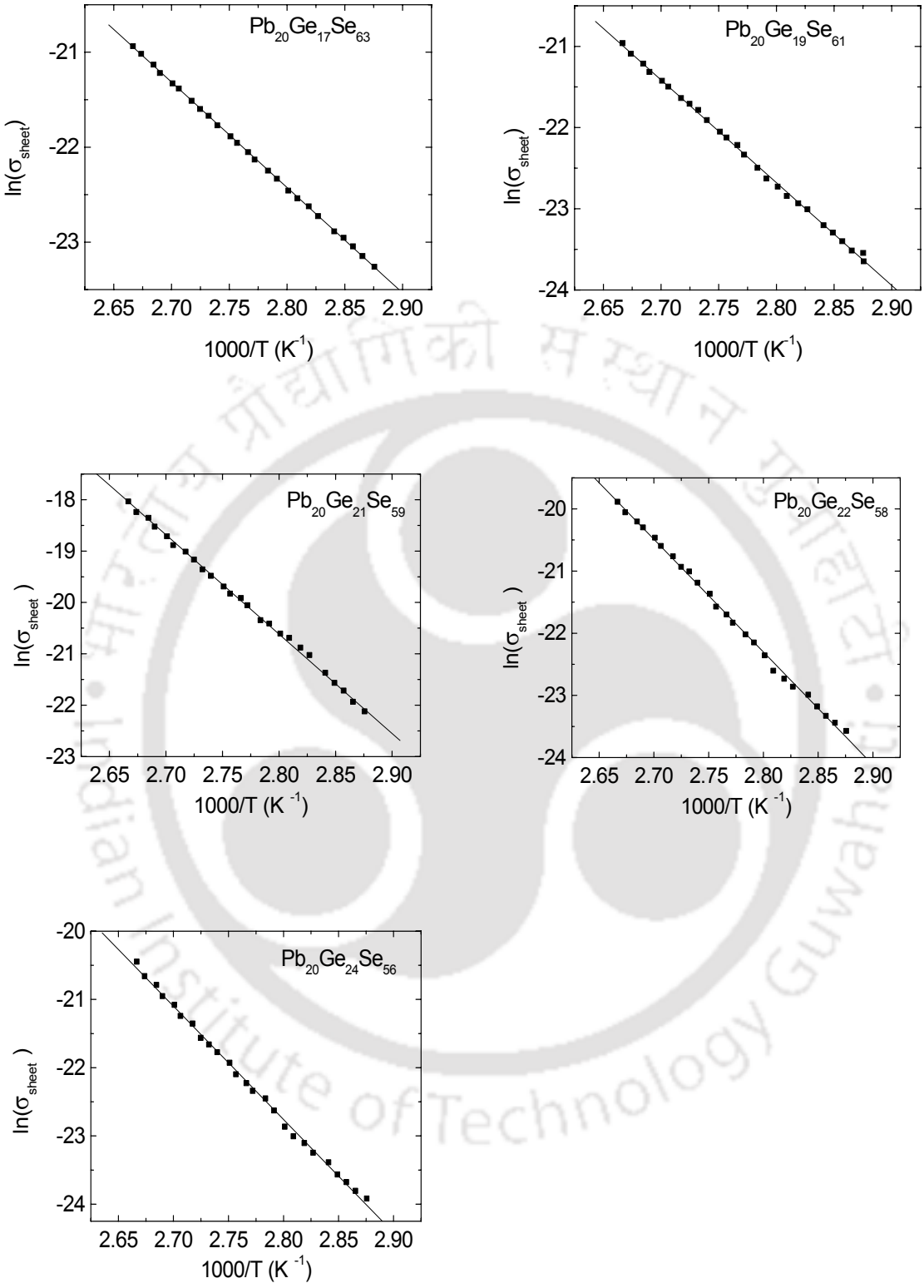

Figure 3.17b: ln (σ) versus 1000/T plots of $Pb_{20}Ge_xSe_{80-x}$ thin films

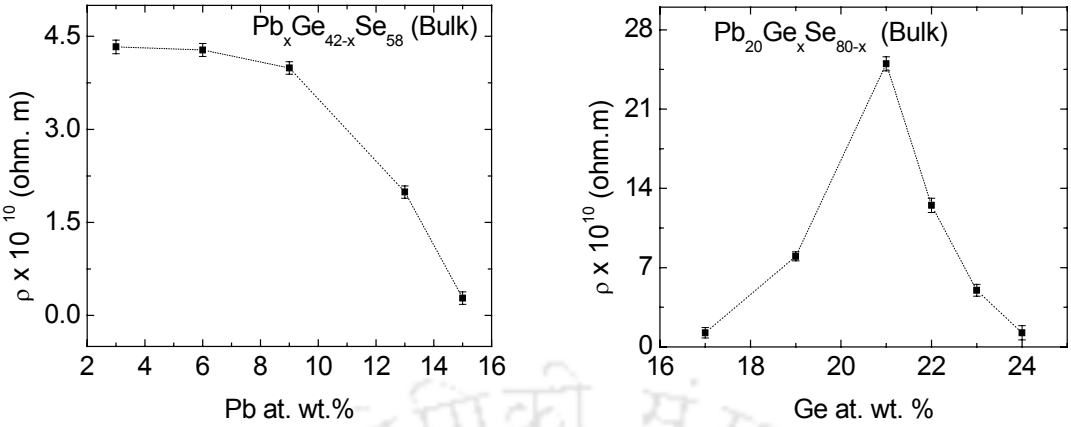

Figure 3.18: Variation of resistivity of bulk Pb-Ge-Se glass with composition.

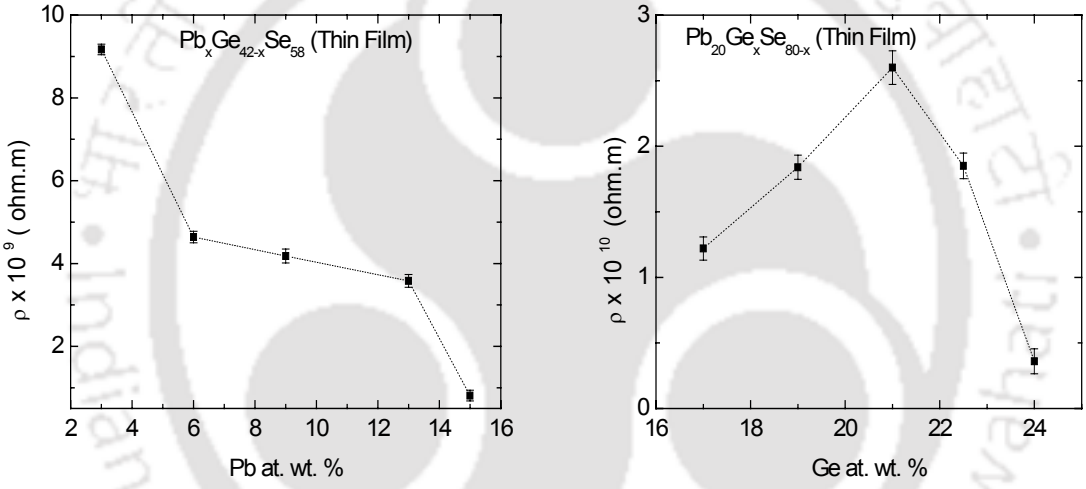

Figure 3.19: Variation of resistivity with composition (at 348 K) for thin films Pb-Ge-Se glasses.

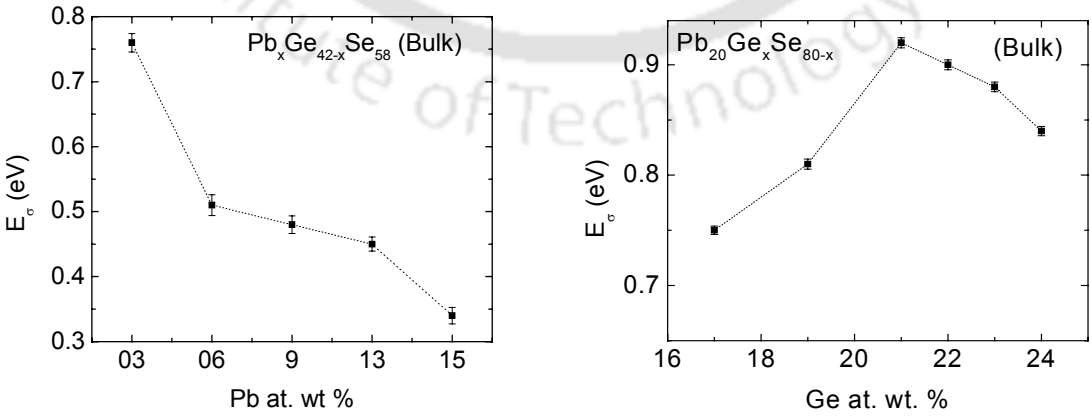

Figure 3.20: Variation of E_σ with composition of bulk Pb-Ge-Se glasses.

Table 3.6: Activation energy for electrical conduction in bulk Pb-Ge-Se glasses. The $Pb_xGe_{42-x}Se_{58}$ data in parentheses was taken from [131] and the $Pb_{20}Ge_xSe_{80-x}$ data from [107]

Bulk sample composition	ρ x 10^{10} at 348K (ohm.m)	E_σ (eV)	Bulk sample composition	ρ at 298 K (ohm.m)	E_σ (eV)
$Pb_{03}Ge_{39}Se_{58}$	4.33 ± 0.11	0.76 ± 0.02	$Pb_{20}Ge_{17}Se_{63}$	(1.25 x 10^9)	(0.75)
$Pb_{05}Ge_{37}Se_{58}$	(1.81 x 10^{11})	(0.86)	$Pb_{20}Ge_{19}Se_{61}$	(2 .0x 10^{10})	(0.81)
$Pb_{06}Ge_{36}Se_{58}$	4.28 ± 0.10	0.51 ± 0.01	$Pb_{20}Ge_{21}Se_{59}$	(2.5 x 10^{11})	(0.92)
$Pb_{09}Ge_{33}Se_{58}$	3.99 ± 0.10	0.48 ± 0.01	$Pb_{20}Ge_{22}Se_{58}$	(1.25 x 10^{11})	(0.90)
$Pb_{10}Ge_{32}Se_{58}$	(1.35 x 10^9)	(0.78)	$Pb_{20}Ge_{23}Se_{57}$	(1.67 x 10^{10})	(0.88)
$Pb_{13}Ge_{29}Se_{58}$	1.99 ± 0.05	0.45 ± 0.01	$Pb_{20}Ge_{24}Se_{56}$	(5.0 x 10^9)	(0.84)
$Pb_{15}Ge_{27}Se_{58}$	0.28 ± 0.01 (5.64 x 10^8)	0.34 ± 0.01 (0.73)			

Table 3.7: ρ_s and E_σ of Pb-Ge-Se thin films.

Thin film composition	ρ_s x 10^9 (ohm. m)	E_σ (eV)	Thin film composition	ρ_s x 10^{10} (ohm. m)	E_σ (eV)
$Pb_{03}Ge_{39}Se_{58}$	9.17 ± 0.27	1.33 ± 0.02	$Pb_{20}Ge_{17}Se_{63}$	1.22 ± 0.03	0.95 ± 0.02
$Pb_{06}Ge_{36}Se_{58}$	4.18 ± 0.12	1.25 ± 0.02	$Pb_{20}Ge_{19}Se_{61}$	1.84 ± 0.05	1.10 ± 0.02
$Pb_{09}Ge_{33}Se_{58}$	4.64 ± 0.12	1.07 ± 0.02	$Pb_{20}Ge_{21}Se_{59}$	2.60 ± 0.08	1.67 ± 0.03
$Pb_{13}Ge_{29}Se_{58}$	3.58 ± 0.11	0.95 ± 0.01	$Pb_{20}Ge_{22.5}Se_{57.5}$	1.85 ± 0.05	1.56 ± 0.03
$Pb_{15}Ge_{27}Se_{58}$	0.81 ± 0.02	0.77 ± 0.01	$Pb_{20}Ge_{24}Se_{56}$	0.36 ± 0.02	1.43 ± 0.03

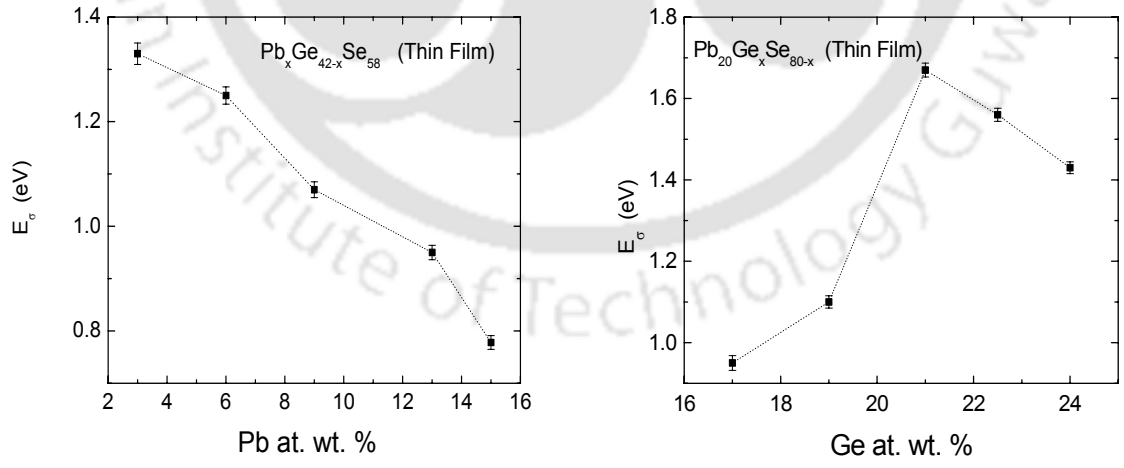

Figure 3.21: Variation activation energy for electrical conduction in thin film samples with composition at 348 K.

3.5. Optical absorption

The optical band gap of Pb-Ge-Se glasses was measured using a dual beam uv-vis-nir spectrophotometer as explained in chapter 2. It was already pointed out that in the high absorption region, the absorption coefficient α(v) follows a power law behaviour {relation 1.23}. The optical band gap calculated for the $Pb_xGe_{42-x}Se_{58}$ and $Pb_{20}Ge_xSe_{80-x}$ glasses in bulk and thin film form are shown in table 3.8. Figure 3.22 shows the $(\alpha hv)^{1/2}$ versus (hv) for $Pb_{03}Ge_{39}Se_{58}$ and $Pb_{20}Ge_{17}Se_{63}$ thin films for Pb-Ge-Se glasses. The variation of E_{opt} with composition are shown in figure 3.23 for bulk glasses and in figure 3.24 for thin films.

The variation of optical band gap energy (E_{opt}) of Pb-Ge-Se glasses (Series II) with increase in Ge at. wt. % could be understood on the basis of the average bond energy of the glasses. It has already been pointed in section 3.2 of this chapter that the average bond energy of the glasses of series II is maximum at $Pb_{20}Ge_{21}Se_{59}$. Since E_{opt} depends on the average bond energy of the glass, E_{opt} shows a maximum at $Pb_{20}Ge_{21}Se_{59}$. In the case of series I glasses the average bond energy decreases and attains a minimum near 9 at. wt. % Pb. So $E_{opt}$of series I bulk glasses decreases sharply with increase in Pb content and then remain almost steady after 9 at. wt. % of Pb. This films of series II glasses replicate the behaviour shown by bulk glasses. In the case of thin films of series I glasses, the increase in E_{opt} after 9 at. wt. % Pb may be due to the presence of large amount of higher energy bonds like Pb-Se.

Table 3.8: Optical band gap energy for bulk and thin film Pb-Ge-Se glass

Sample composition	E_{opt} (eV) (Bulk)	E_{opt} (eV) (Thin Film)	Sample composition	E_{opt} (eV) (Bulk)	E_{opt} (eV) (Thin Film)
$Pb_{03}Ge_{39}Se_{58}$	1.91	1.76 ± 0.01	$Pb_{20}Ge_{17}Se_{63}$	1.66 (1.63)	1.61 ± 0.01
$Pb_{06}Ge_{36}Se_{58}$	1.79	1.72 ± 0.01	$Pb_{20}Ge_{19}Se_{61}$	1.72 (1.67)	1.65 ± 0.01
$Pb_{09}Ge_{33}Se_{58}$	1.72	1.67 ± 0.01	$Pb_{20}Ge_{21}Se_{59}$	1.74 (1.68)	1.66 ± 0.01
$Pb_{13}Ge_{29}Se_{58}$	1.73	1.69 ± 0.01	$Pb_{20}Ge_{22.5}Se_{57.5}$	1.67 (---)	1.64 ± 0.01
$Pb_{15}Ge_{27}Se_{58}$	1.74	1.77 ± 0.01	$Pb_{20}Ge_{23}Se_{57}$	--- (1.51)	---
			$Pb_{20}Ge_{24}Se_{56}$	1.61 (1.46)	1.63 ± 0.01

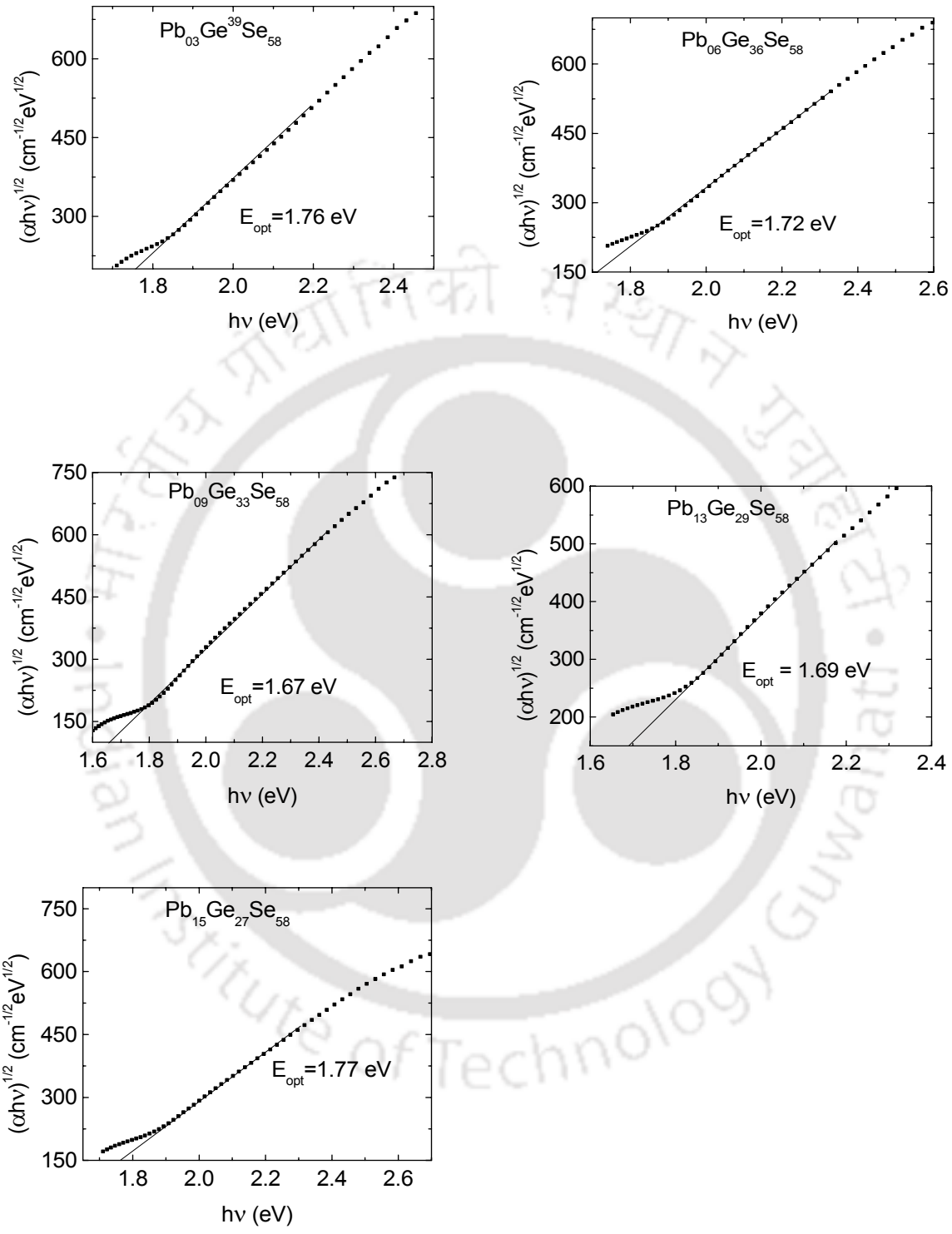

Figure 3.22a: $(\alpha h\nu)^{1/2}$ versus hν plots for $Pb_xGe_{42-x}Se_{58}$ thin films.

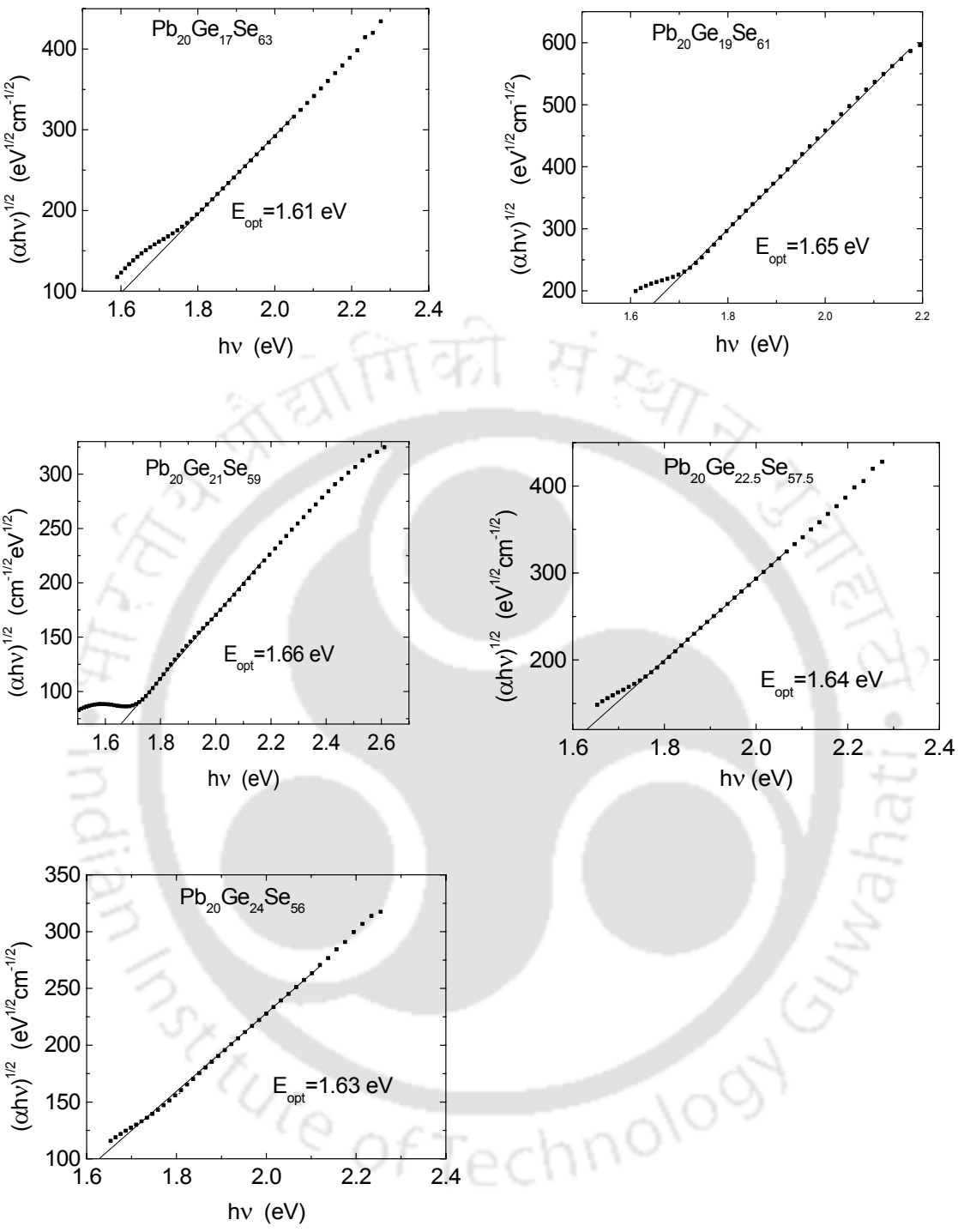

Figure 3.22b: $(\alpha h\nu)^{1/2}$ versus hν plots for $Pb_{20}Ge_xSe_{80-x}$ thin films.

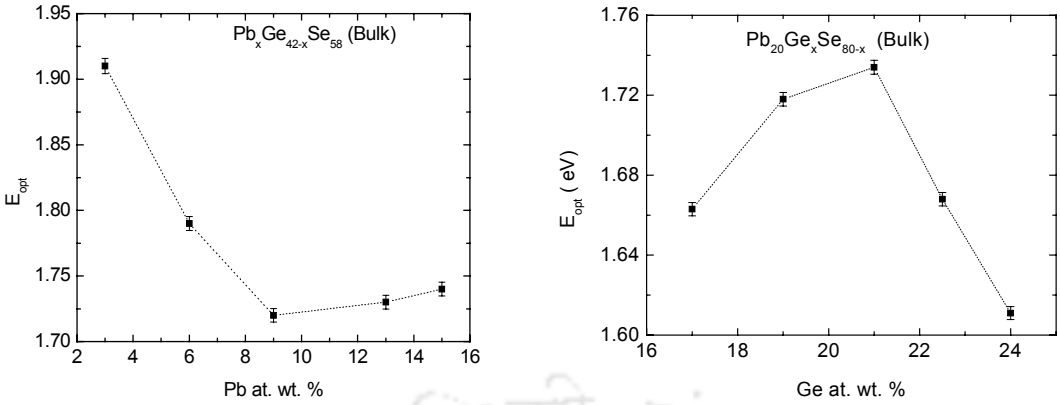

Figure 3.23: Variation of optical band gap with composition of bulk Pb-Ge-Se glasses.

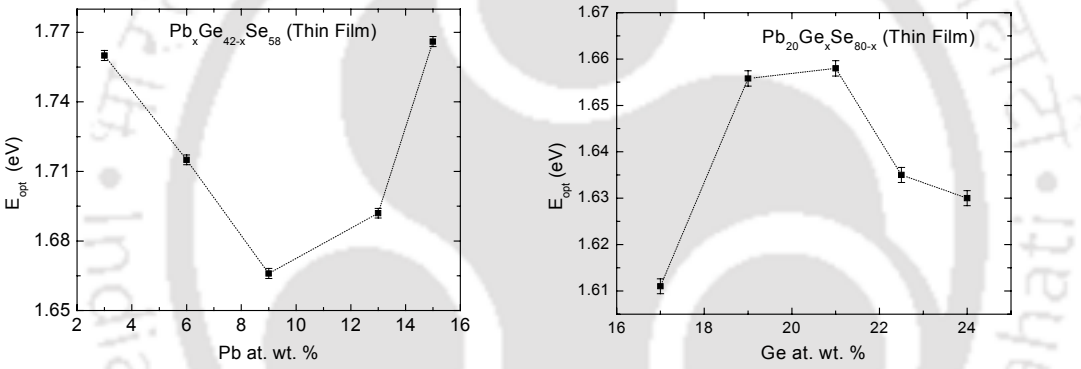

Figure 3.24: Variation of optical band gap with composition of Pb-Ge-Se thin films

3.6. Microhardness

The microhardness of glasses has been measured by the procedure already described in second chapter. Figure 3.25 shows a typical indentation made on a Pb-Ge-Se glass surface. The microhardness expressed in terms of the measured Vickers hardness number (VHN) are tabulated in table 3.9. Each value quoted is the average of at least ten independent measurements. Figure 3.26 shows the variation of VHN with composition. Microhardness is a bond sensitive property [3]. With the increase in the concentration of Pb in series I glasses, VHN decreases. This

behaviour can be understood in terms of the variation in the average bond energy of the glasses with change in composition. Substitution of Ge with Pb atoms results in the reduction of Ge-Se bonds and an increase in Pb-Se bonds. Since Pb-Se bonds have a lower energy than Ge-Se bonds, addition of Pb results in a reduction in the average bond energy of $Pb_xGe_{42-x}Se_{58}$ glasses. This reduction in the average bond energy of the glasses is reflected in the reduction in the microhardness of these glasses. Similar interpretation could be made on the basis of average bond energy value for the series II glasses. Since Ge-Se bonds are maximum near 21 at. wt. % Ge, VHN shows a maximum value at 21 at. wt. % Ge.

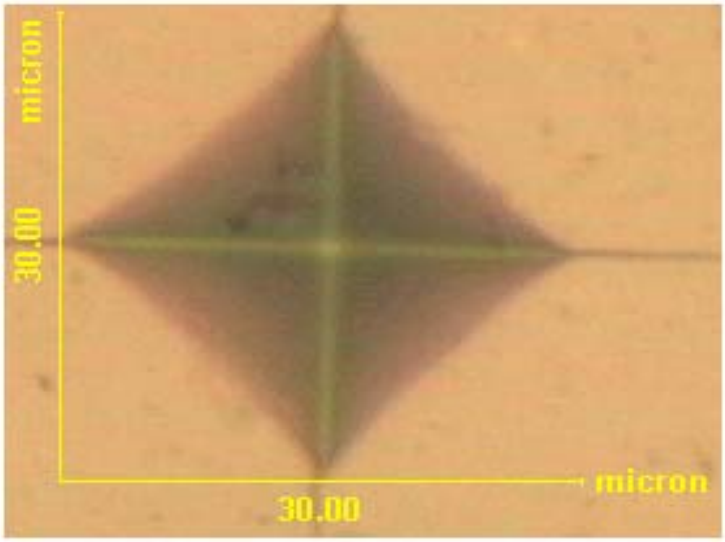

Figure 3.25: A typical indent made on the polished Pb-Ge-Se glass surface

Table 3.9: Vickers Hardness Number (VHN) for Pb-Ge-Se bulk glasses.

Sample composition	VHN ($kg.mm^{-2}$)	Sample composition	VHN ($kg.mm^{-2}$)
$Pb_{03}Ge_{39}Se_{58}$	227 ± 3	$Pb_{20}Ge_{17}Se_{63}$	191 ± 3
$Pb_{06}Ge_{36}Se_{58}$	224 ± 3	$Pb_{20}Ge_{19}Se_{61}$	195 ± 3
$Pb_{09}Ge_{33}Se_{58}$	218 ± 3	$Pb_{20}Ge_{21}Se_{59}$	203 ± 3
$Pb_{13}Ge_{29}Se_{58}$	214 ± 3	$Pb_{20}Ge_{22.5}Se_{57.5}$	197 ± 3
$Pb_{15}Ge_{27}Se_{58}$	207 ± 3	$Pb_{20}Ge_{24}Se_{56}$	177 ± 3

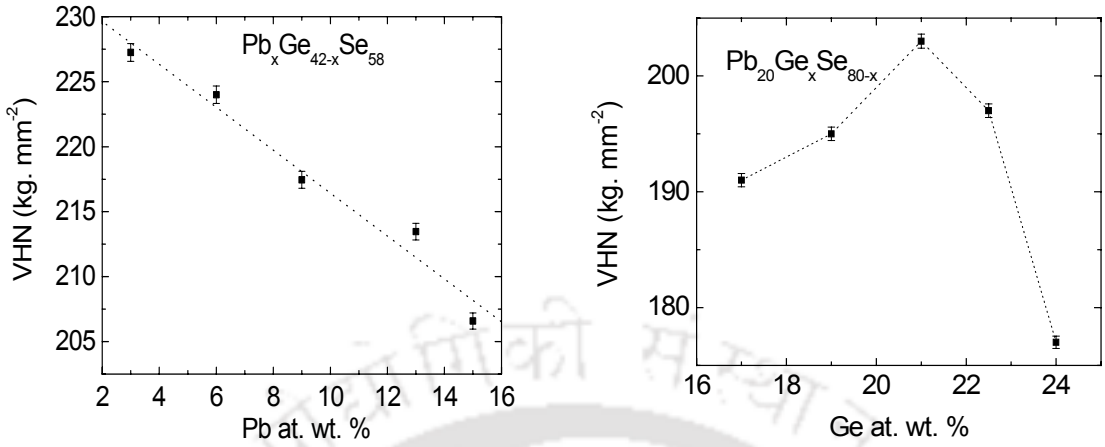

Figure 3.26: Variation of Vickers Hardness Number with composition of the Pb-Ge-Se glasses.

3.7. Summary

The main results obtained from the studies reported in this chapter can be summarized as follows:

1. DSC studies shows that (i) T_g is a minimum for the glass with 9 at. wt. % Pb in series I and maximum at the composition with 21 at. wt. % Ge in series II bulk glasses. The first crystallization temperature (T_c) follows the same trend as the T_g for both the series of glasses. (ii) Degree of fragility (m) and excess heat capacity (ΔC_p) of series I and series II glasses show minimum values at the composition at which the carrier reversal was observed indicating that these compositions are kinematically stronger and thermodynamically stronger than the rest of the compositions.
2. From the thermoelectric power measurements, the sign of the majority carrier type was determined for the Pb-Ge-Se glasses. Bulk $Pb_{03}Ge_{39}Se_{58}$, $Pb_{06}Ge_{36}Se_{58}$, $Pb_{20}Ge_{17}Se_{63}$, $Pb_{20}Ge_{19}Se_{61}$ glasses were *p*- type semiconductor and the rest of the glasses were *n*-type semiconductor. However in thin films, the $Pb_{09}Ge_{33}Se_{58}$ composition showed *p*- type conductivity. The carrier type reversal

in these glasses was explained on the basis of the change in the concentration of charged defect states with the variation in composition.

3. The optical band gap energy is a minimum for the composition with 9 at. wt. % Pb for series I and a maximum at the composition with 21 at. wt. % Ge for series II glasses.
4. From d. c. electrical conductivity measurements, the electronic conduction in the temperature range 325 K to 425 K could be attributed to band transport mechanism. Composition dependence of resistivity and activation energy of electrical conductivity showed appreciable changes at the composition at which the carrier reversal was observed.
5. Microhardenss of series I and series II glass show similar trends as depicted by T_g (and E_{opt}), since this property also depends on the average bond energy of the glass.

Chapter 4

Studies on bulk and thin films of Pb-Ge-Se-Te glasses

Subsequent to the observation of carrier type reversal in Pb modified Ge-Se glasses [107]. Murugavel *et al* [136] showed that the sign of the charge carrier could be reversed on the addition of Pb in $Pb_xGe_{42-x}Se_{48}Te_{10}$ ternary glasses. They attributed the conduction type change in these glasses to the modification of defect states on the addition of Pb. They also addressed the role of the polarizibilty of the dopant, band structure *etc*., on the carrier type reversal. According to this report, charge carrier reversal occurs in these glass systems on addition of more than 8 at. wt. % Pb. Thermoelectric power measurements showed that the Seebeck coefficient varied between 0.35 to -1.6 $mV.K^{-1}$ at 413K for the composition range of $5 \leq x \leq 20$ (where x corresponds to at. wt. % of Pb). The electrical conductivity ranged from 10^{13} to 10^{8} $ohm^{-1}cm^{-1}$ and the activation energy for electrical conduction varied from 1.0 to 0.5 eV at 300 K. The advantage of the Pb-Ge-Se-Te system over Pb-Ge-Se is the higher electrical conductivity exhibited by the former system. Melt quenched $Ge_{20}Bi_xSe_{70-x}Te_{10}$ glasses [106] show a higher electrical conductivity than $Ge_{20}Bi_xSe_{80-x}$ glasses [105].

Literature survey shows that there are no further reports on these quaternary glass system. In this chapter, $Pb_xGe_{42-x}Se_{48}Te_{10}$ ($0 \leq x \leq 15$) and $Pb_{20}Ge_xSe_{70-x}Te_{10}$ ($17 \leq x \leq 24$) glasses have been prepared in the bulk and thin film forms. The composition dependence of various physical properties of these glasses have also been studied.

4.1. Sample preparation and characterisation

Bulk glass samples of $Pb_xGe_{42-x}Se_{48}Te_{10}$ ($0 \leq x \leq 15$) and $Pb_{20}Ge_xSe_{70-x}Te_{10}$ ($17 \leq x \leq 24$) were prepared by the melt quenching technique. Precautions were taken to prepare glasses under similar conditions as explained in chapter 3. All the as-quenched glasses were verified to be amorphous by XRD patterns recorded in the 2θ range of 10º < 2θ < 70º. A typical XRD pattern for Pb modified Ge-Se-Te glass is shown in figure 4.1. Thermoelectric power measurements on individual glass samples revealed that glass compositions with 3 and 6 at. wt. % Pb in $Pb_xGe_{42-x}Se_{48}Te_{10}$ and compositions with 17 and 19 at. wt. % Ge in $Pb_{20}Ge_xSe_{70-x}Te_{10}$ series of glasses showed *p*- type conduction, whereas the rest of the compositions exhibited *n*- type conduction. Glass transition temperature was observed using a DSC under a constant heating rate of 10 ˚C.min^{-1} as explained in chapter 2.

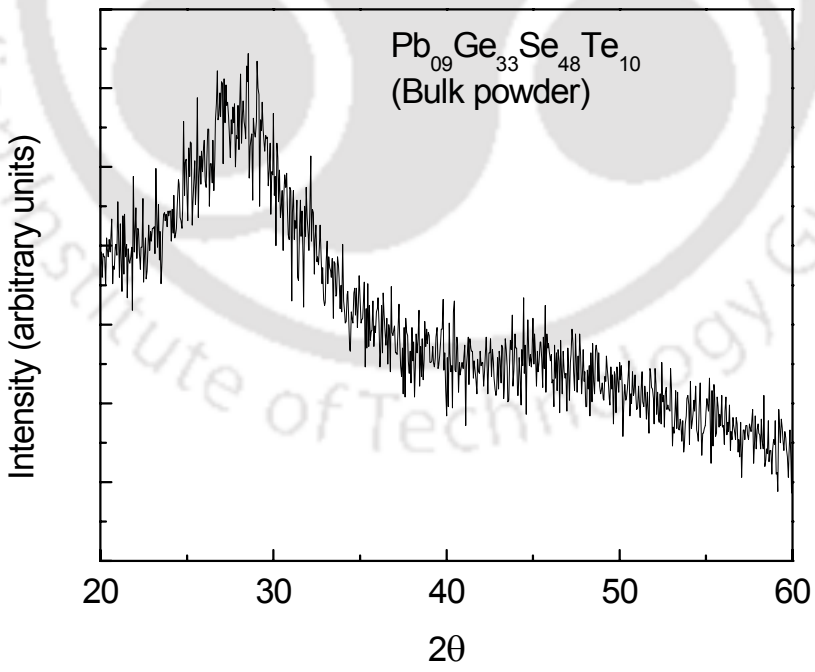

Figure 4.1: XRD pattern of Pb-Ge-Se-Te glasses in powdered form.

Thin films of the above mentioned glass compositions were prepared by thermal evaporation technique. The films were deposited on cleaned glass substrates (microscope cover slips) by passing a current of 200 A through the molybdenum boat for about 3-5 minute duration. An X-ray diffractometer equipped with grazing incidence device (GID) was used to verify the amorphous nature of the thin films. Thickness of the deposited films was measured with the help of an ellipsometer. Composition analysis for the individual films was done using SEM-EDX. The composition of each sample was found to be identical to the bulk samples used for deposition with an uncertainty of ± 2 %.

4.2. Differential scanning calorimeter studies

Non-isothermal studies on $Pb_xGe_{42-x}Se_{48}Te_{10}$ ($3 \leq x \leq 15$) and $Pb_{20}Ge_xSe_{80-x}$ ($17 \leq x \leq 24$) glasses were performed following the procedure explained in chapter 2 and chapter 3. Figure 4.2 shows the DSC curves obtained for Pb-Ge-Se-Te bulk glasses under a constant heating rate of 10 °C.min^{-1}.

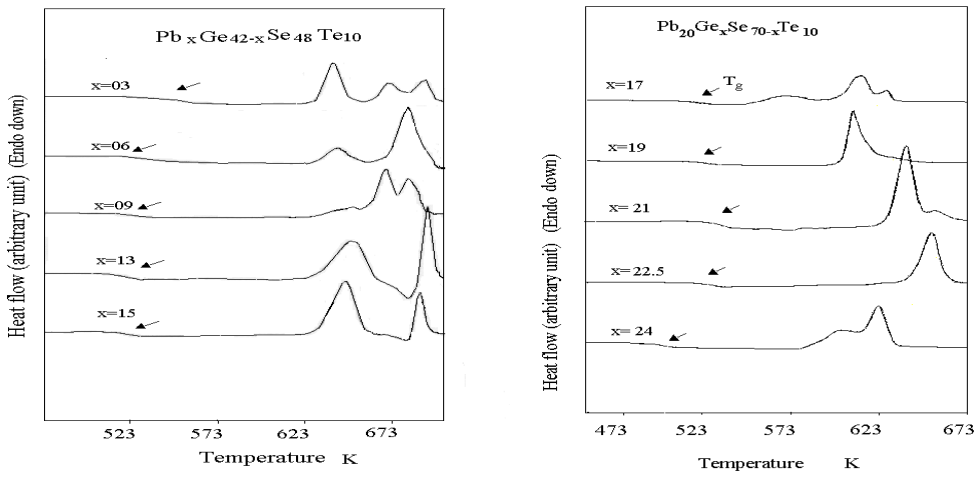

Figure 4.2: DSC curves of Pb-Ge-Se-Te glasses recorded when heated at 10° C min^{-1}.

Glass transition temperature (T_g) of various compositions of these glasses was observed in the temperature between 495 K to 540 K for both $Pb_xGe_{42-x}Se_{48}Te_{10}$ (series I) and $Pb_{20}Ge_xSe_{70-x}Te_{10}$ (series II) glasses when heated at 10 °C.min^{-1}. These glasses also showed multiple crystallization peaks as in Pb-Ge-Se glasses on heating beyond the glass transition temperature, signifying the devitrification of different crystalline phases in the multicomponent glasses. Glasses with x ≤ 9 at. wt. % belonging to series I exhibited (Figure 4.2) three crystallization peaks, whereas, glasses with x > 9 at. wt. % Pb showed two well-resolved crystallization peaks. It can be observed that the glass with x = 21 at. wt. % Ge belonging to Series II exhibited a sharp crystallization exotherm. The variation of T_g and the crystallization temperature T_c of both the series of glasses as a function of composition is shown in figure 4.3. All the DSC curves shown in (Figure 4.2) were recorded under a constant heating rate of 10 °C.min^{-1}. The corresponding data are tabulated in the table 4.1.

Table 4.1: Glass transition temperature (T_g) and crystallization temperature (T_c) of Pb-Ge-Se-Te glasses.

Sample composition	T_g (K)	T_c (K)	Sample composition	T_g (K)	T_c (K)
$Pb_{03}Ge_{39}Se_{48}Te_{10}$	536 ± 1	639 ± 1	$Pb_{20}Ge_{17}Se_5Te_{10}$	496 ± 1	563 ± 1
$Pb_{06}Ge_{36}Se_{48}Te_{10}$	522 ± 1	641 ± 1	$Pb_{20}Ge_{19}Se_{51}Te_{10}$	510 ± 1	606 ± 1
$Pb_{09}Ge_{33}Se_{48}Te_{10}$	517 ± 1	653 ± 1	$Pb_{20}Ge_{21}Se_{49}Te_{10}$	518 ± 1	634 ± 1
$Pb_{13}Ge_{29}Se_{48}Te_{10}$	514 ± 1	650 ± 1	$Pb_{20}Ge_{22.5}Se_{47.5}Te_{10}$	514 ± 1	653 ± 1
$Pb_{15}Ge_{27}Se_{48}Te_{10}$	515 ± 1	646 ± 1	$Pb_{20}Ge_{24}Se_{46}Te_{10}$	508 ± 1	622 ± 1

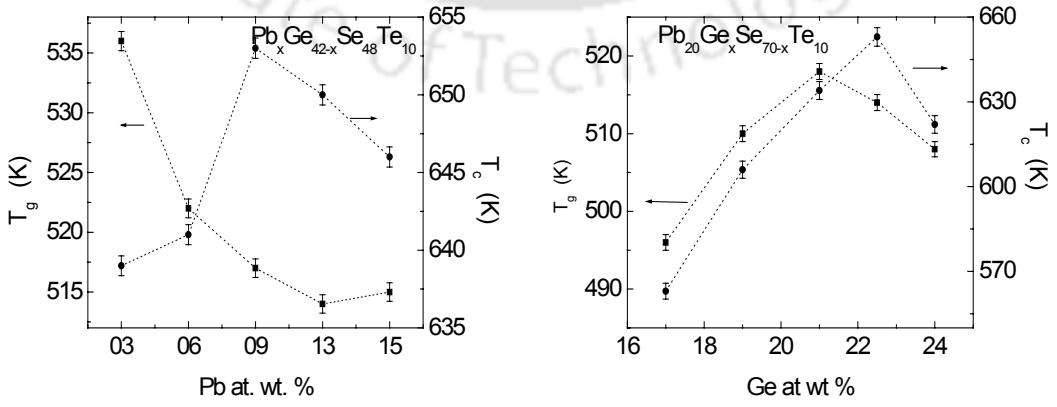

Figure 4.3: Glass transition temperature (T_g) and crystallization temperature (T_c) for Pb-Ge-Se-Te glasses at the heating rate 10° C min^{-1}.

Figure 4.3 shows that in the case of $Pb_xGe_{42-x}Se_{48}Te_{10}$ glasses, T_g shows a sharp decrease initially as Pb replaces Ge until 9 at. wt. % of Pb. After this T_g shows no appreciable change. T_g is a bond sensitive property. The variation of T_g with composition can be understood on the basis of the variation in average bond energy of these glasses in a manner similar to the case of Pb-Ge-Se glasses. In $Pb_xGe_{42-x}Se_{48}Te_{10}$ glasses Te content remains the same all through the series. Hence, the same arguments applicable to $Pb_xGe_{42-x}Se_{58}$ are also applicable here since Pb content varies in this series at the cost of Ge content. The average bond energy of the glasses decrease as Pb content is increased in $Pb_xGe_{42-x}Se_{48}Te_{10}$ series of glasses. Since Te bonds have lower bond energy as compared to Se bonds, (Appendix I) $Pb_xGe_{42-x}Se_{48}Te_{10}$ glasses exhibit a lower T_g as compared to the corresponding $Pb_xGe_{42-x}Se_{58}$ glasses (Table 3.1). In the case of Series $Pb_{20}Ge_xSe_{70-x}Te_{10}$, T_g increases with the addition of Ge, attains a maximum value at 21 at. wt. % of Ge and then decreases. In this series the Pb and Te concentration remain constant, whereas, Se atoms are gradually replaced by Ge atoms. From the bond calculation on $Pb_{20}Ge_xSe_{80-x}$ glasses proposed by Tohge *et al* [107], Ge-Se bonds were a maximum near x = 20 at. wt. % Ge. Accordingly, the average bond energy of the glasses start increasing with addition of Ge, attains a maximum value near 21 at. wt. % of Ge and then decreases in this series of glasses. Since T_g depends on the average bond energy of the glass, it shows a maximum at 21 at. wt. % Ge. It can be seen that substitution of Se with Te results in lowering of T_g of $Pb_{20}Ge_xSe_{70-x}Te_{10}$ glasses as compared to $Pb_{20}Ge_xSe_{80-x}$ in all cases.

The crystallization temperature T_c for the two series of Pb-Ge-Se-Te glasses is shown in figure 4.3. T_c shows a maximum at the 22.5 at. wt. % of Ge and at 9 at. wt. % of the Pb for $Pb_xGe_{42-x}Se_{48}Te_{10}$ glass and $Pb_{20}Ge_xSe_{70-x}Te_{10}$ glasses

respectively. A higher T_c signifies a relatively stronger inhibition to the nucleation and growth of the crystalline phase. From the data presented in the table 4.1, one can say that the glass compositions at x = 9 at. wt. % Pb ($Pb_xGe_{42-x}Se_{48}Te_{10}$ series) and x = 22.5 at. wt. Ge ($Pb_{20}Ge_xSe_{70-x}Te_{10}$ series) exhibit the highest inhibition to crystallization. It was not possible to compare composition dependence T_c of other exotherms since all glasses do not exhibit the same number of crystalline exotherms.

Kissinger's and Thakor's relations (equation 2.1 and 2.2) were used for estimating the activation energy for the glass transition of various glass compositions using the procedure already described in chapter 2. The activation energy obtained for glass transition E_K (Kissinger) and E_T (Thakor) obtained for these glasses have been plotted in figure 4.4 and figure 4.5.

Table: 4.2: Activation energy for glass transition (E_K and E_T) for Pb-Ge-Se-Te glasses.

Sample composition	E_K kJ.mol^{-1}	E_T kJ.mol^{-1}	Sample composition	E_K kJ.mol^{-1}	E_T kJ.mol^{-1}
$Pb_{03}Ge_{39}Se_{48}Te_{10}$	280 ± 3	307 ± 3	$Pb_{20}Ge_{17}Se_{53}$ Te_{10}	217 ± 2	268 ± 3
$Pb_{06}Ge_{36}Se_{48}$ Te_{10}	248 ± 2	268 ± 3	$Pb_{20}Ge_{19}Se_{51}$ Te_{10}	206 ± 2	213 ± 2
$Pb_{09}Ge_{33}Se_{48}$ Te_{10}	240 ± 2	249 ± 2	$Pb_{20}Ge_{21}Se_{49}$ Te_{10}	199 ± 2	208 ± 2
$Pb_{13}Ge_{29}Se_{48}$ Te_{10}	258 ± 2	245 ± 2	$Pb_{20}Ge_{22.5}Se_{47.5}Te_{10}$	292 ± 3	303 ± 3
$Pb_{15}Ge_{27}Se_{48}$ Te_{10}	307 ± 3	313 ± 3	$Pb_{20}Ge_{24}Se_{46}$ Te_{10}	317 ± 3	329 ± 3

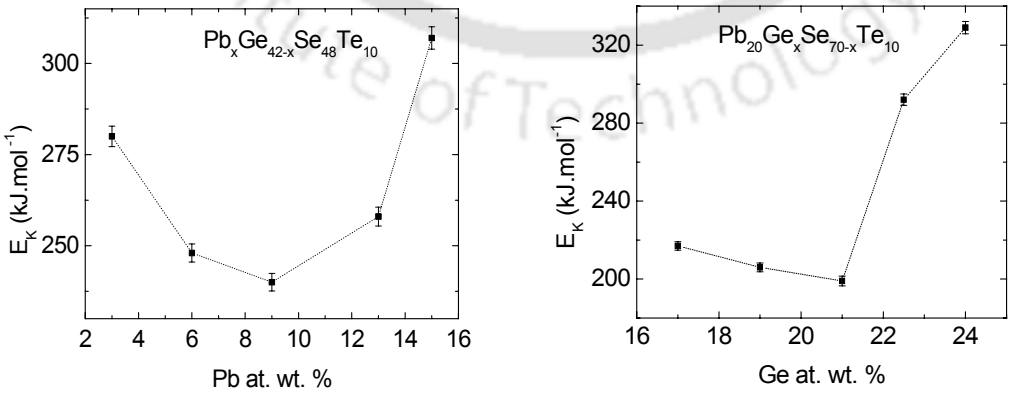

Figure 4.4: Activation energy (E_K) for glass transition of Pb-Ge-Se-Te glasses.

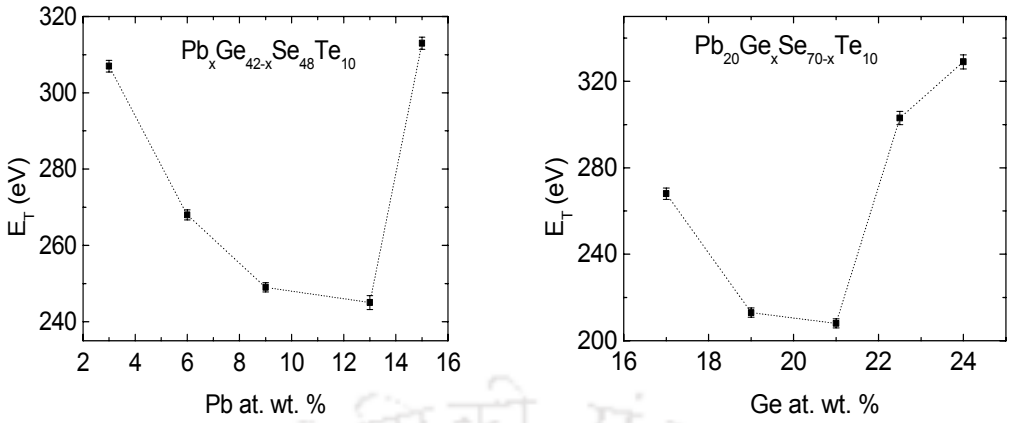

Figure 4.5: Activation energy (E_T) for glass transition of Pb-Ge-Se-Te glasses.

From figure 4.4 and figure 4.5, it can be seen that E_K and E_T for both the series of glasses show a minimum value at the composition at which the *p*- to *n*- transition was observed. As the activation energy is a measure of the resistance imposed by the glassy network for the glass-super-cooled liquid transition, one can say that the glass-super-cooled liquid transition is least hindered for the compositions with 9 at. wt. % of Pb in $Pb_xGe_{42-x}Se_{48}Te_{10}$ series of glasses and 21 at. wt. % of Ge in $Pb_{20}Ge_xSe_{70-x}Te_{10}$ series of glasses.

Table: 4.3 : Excess heat capacity and degree of fragility (m) of Pb-Ge-Se-Te glasses.

Sample composition	ΔC_p $JK^{-1}mol^{-1}$	E_η $kJmol^{-1}$	m	Sample composition	ΔC_p $JK^{-1}mol^{-1}$	E_η $kJmol^{-1}$	m
$Pb_{03}Ge_{39}Se_{48}Te_{10}$	20.08 ± 0.20	307	30	$Pb_{20}Ge_{17}Se_{53}$ Te_{10}	28.48 ± 0.30	268	28
$Pb_{06}Ge_{36}Se_{48}$ Te_{10}	17.30 ± 0.17	268	27	$Pb_{20}Ge_{19}Se_{51}$ Te_{10}	18.70 ± 0.19	213	22
$Pb_{09}Ge_{33}Se_{48}$ Te_{10}	11.20 ± 0.11	249	25	$Pb_{20}Ge_{21}Se_{49}$ Te_{10}	12.00 ± 0.12	208	21
$Pb_{13}Ge_{29}Se_{48}$ Te_{10}	19.80 ± 0.20	245	25	$Pb_{20}Ge_{22.5}Se_{47.5}$ Te_{10}	16.90 ± 0.17	303	31
$Pb_{15}Ge_{27}Se_{48}$ Te_{10}	28.80 ± 0.30	313	32	$Pb_{20}Ge_{24}Se_{46}$ Te_{10}	26.30 ± 0.26	329	35

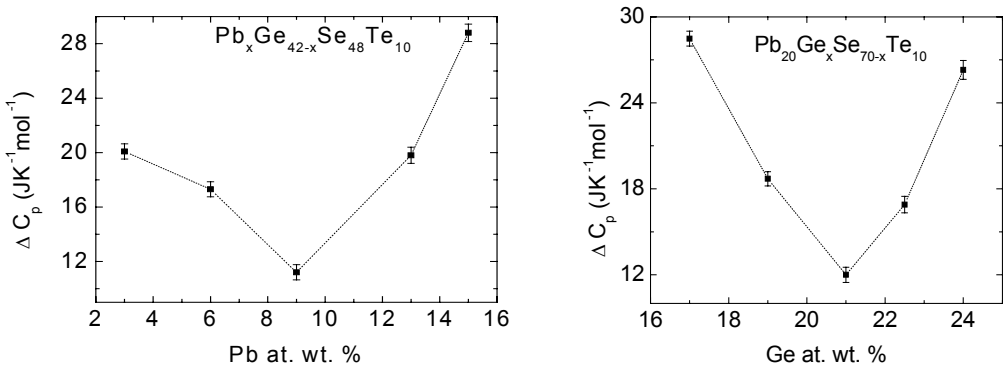

Figure 4.6: Excess heat capacity of Pb-Ge-Se-Te glasses.

The activation energy for viscous flow E_η has been estimated using relation 2.3. E_η values of Pb-Ge-Se-Te samples are tabulated in table 4.3, together with the degree of fragility m estimated using relation (2.9). Both E_η and m show minimum value at the compositions at which the *p*- to *n*- type transition was observed. Further from the value of m, these glasses can be classified as kinetically strong (KS). Figure 4.6 shows the variation of the excess heat capacity at T_g (ΔC_p) of Pb-Ge-Se-Te glasses belonging to $Pb_xGe_{42-x}Se_{48}Te_{10}$ and $Pb_{20}Ge_xSe_{70-x}Te_{10}$ glasses. As shown in the figure, ΔC_p shows a minimum at the glass MCCR composition in the case of $Pb_xGe_{42-x}Se_{48}Te_{10}$ and $Pb_{20}Ge_xSe_{70-x}Te_{10}$ glasses. A small ΔC_p is also a proof of a strong thermodynamic behavior which indicates that the glass is not far away from its thermodynamic equilibrium. Analysis of the activation energy and the excess heat capacity at the glass transition of these glasses shows that $Pb_{09}Ge_{33}Se_{48}Te_{10}$ and $Pb_{20}Ge_{21}Se_{49}Te_{10}$ glasses exhibit minimum configuration changes at the glass-to-super-cooled liquid transition. Comparison with the m and ΔC_p values of the corresponding Pb-Ge-Se glass composition shows that Pb-Ge-Se-Te glasses exhibit a less fragile (or more stronger) behaviour in both kinetic and thermodynamic sense.

4.3. Thermoelectric power

Seebeck coefficient (Q) of the two series of glasses, namely, $Pb_xGe_{42-x}Se_{48}Te_{10}$ ($0 \leq x \leq 15$) and $Pb_{20}Ge_xSe_{70-x}Te_{10}$ ($17 \leq x \leq 24$) in both bulk as well as thin film forms were measured following the procedure as mentioned in chapter 2. Q values at 348 K are tabulated in table 4.4. The composition dependence of Q for various compositions of glasses is shown in figure 4.7 for bulk glasses and in figure 4.10 for the corresponding thin films. The temperature dependence of the Seebeck coefficient (Q) for individual glass samples in the range of 313 K to 413 K is shown in figure 4.8 and figure 4.11 for bulk and thin film samples respectively. The activation energy for thermoelectric power (E_s) (table 4.4) has been calculated following the procedure as explained in the chapter 3. Figure 4.9 and figure 4.12 show the variation of E_s with composition for the bulk and thin films of these glasses. The present thermoelectric power measurements revealed that the compositions with 03 and 06 at. wt. % Pb in $Pb_xGe_{42-x}Se_{48}Te_{10}$ series and compositions with 17 and 19 at. wt. % Ge in $Pb_{20}Ge_xSe_{70-x}Te_{10}$ series are *p*-type semiconductors, whereas, the rest of the compositions are *n*- type semiconductors in the case of bulk glasses. In the case of thin films, the *n*- type transition occurred in $Pb_xGe_{42-x}Se_{48}Te_{10}$ glasses after 9 at. wt. % Pb. The other series of thin films, namely, $Pb_{20}Ge_xSe_{70-x}Te_{10}$ showed the transition at the same compositions as the bulk glasses. This variation in bulk and thin film behaviour is attributed to the dimensionality constraint of the films, requiring more Pb^{2+} concentrations to suppress the C_3^+ defects. The transition from *p*- type conduction to *n*- type conduction in Pb modified glasses could also be explained on the basis of Kolobov's proposal of modification in defect states with the addition of Pb in a manner similar to Pb modified Ge-Se glasses (Chapter 3).

Table 4.4: Seebeck coefficient and activation energy for $Pb_xGe_{42-x}Se_{48}Te_{10}$ for thermal conduction in bulk glasses.

Sample composition	Q (mV. K^{-1})	E_s (eV)	Sample composition	Q (mV. K^{-1})	E_s (eV)
$Pb_{03}Ge_{39}Se_{48}Te_{10}$	1.65 ± 0.05	1.04 ± 0.03	$Pb_{20}Ge_{17}Se_{53}$ Te_{10}	1.56 ± 0.05	1.38 ± 0.03
$Pb_{06}Ge_{36}Se_{48}$ Te_{10}	1.22 ± 0.04	0.74 ± 0.03	$Pb_{20}Ge_{19}Se_{51}$ Te_{10}	0.91 ± 0.03	1.11 ± 0.03
$Pb_{09}Ge_{33}Se_{48}$ Te_{10}	-1.24 ± 0.04	0.60 ± 0.03	$Pb_{20}Ge_{21}Se_{49}$ Te_{10}	-0.90 ± 0.03	0.85 ± 0.03
$Pb_{13}Ge_{29}Se_{48}$ Te_{10}	-1.56 ± 0.05	1.00 ± 0.03	$Pb_{20}Ge_{22.5}Se_{47.5}$ Te_{10}	-1.15 ± 0.03	1.17 ± 0.03
$Pb_{15}Ge_{27}Se_{48}$ Te_{10}	-1.90 ± 0.06	1.35 ± 0.03	$Pb_{20}Ge_{24}Se_{46}$ Te_{10}	-1.44 ± 0.04	1.34 ± 0.03

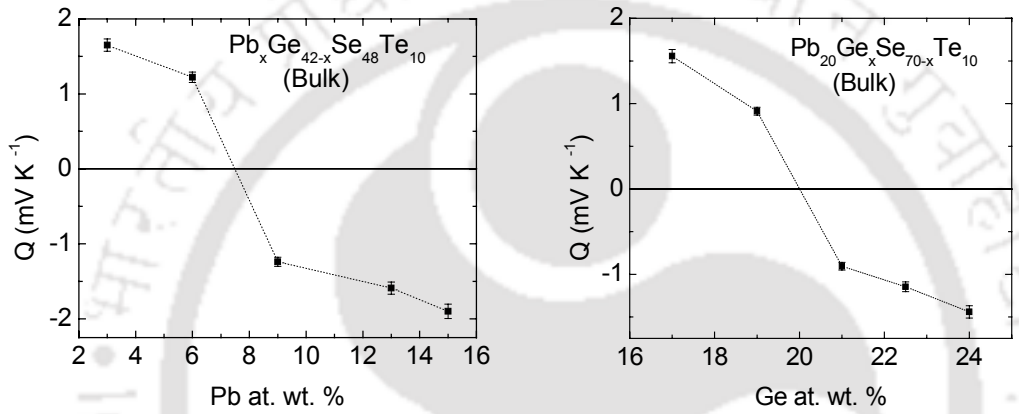

Figure 4.7: Composition dependence of TEP of bulk Pb-Ge-Se-Te glasses.

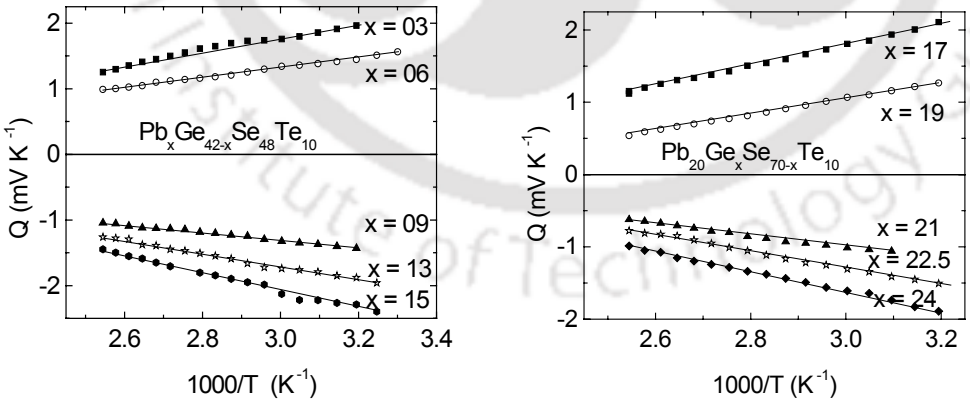

Figure 4.8: Temperature dependence of TEP of bulk Pb-Ge-Se-Te glasses.

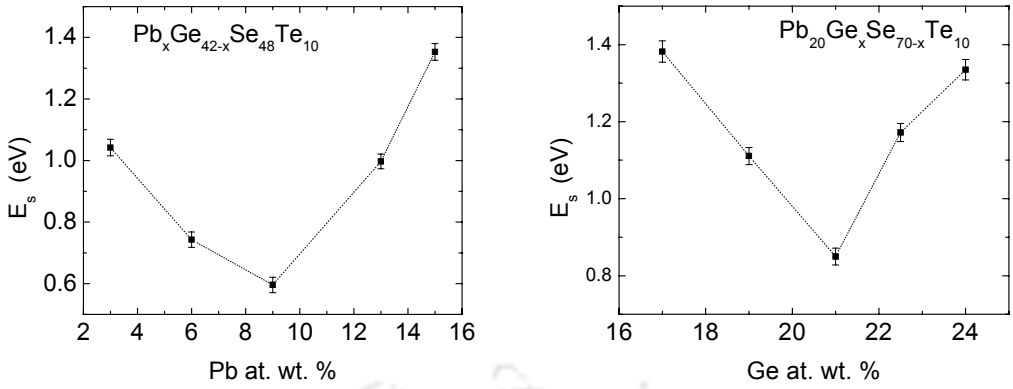

Figure 4.9: Composition dependence of activation energy for thermal conduction (E_s) of bulk Pb-Ge-Se-Te glasses.

Table 4.5: Seebeck coefficient and activation energy for TEP of $Pb_xGe_{42-x}Se_{48}Te_{10}$ thin films.

Sample composition	Q (mV. K^{-1})	E_s (eV)	Sample composition	Q (mV. K^{-1})	E_s (eV)
$Pb_{03}Ge_{39}Se_{48}Te_{10}$	1.86 ± 0.06	2.77 ± 0.03	$Pb_{20}Ge_{17}Se_{53}$ Te_{10}	2.00 ± 0.06	2.89 ± 0.03
$Pb_{06}Ge_{36}Se_{48}$ Te_{10}	1.57 ± 0.05	2.27 ± 0.03	$Pb_{20}Ge_{19}Se_{51}$ Te_{10}	1.42 ± 0.04	2.66 ± 0.03
$Pb_{09}Ge_{33}Se_{48}$ Te_{10}	0.94 ± 0.03	1.85 ± 0.03	$Pb_{20}Ge_{21}Se_{49}$ Te_{10}	-1.51 ± 0.05	2.25 ± 0.03
$Pb_{13}Ge_{29}Se_{48}$ Te_{10}	-1.14 ± 0.03	1.95 ± 0.03	$Pb_{20}Ge_{22.5}Se_{47.5}$ Te_{10}	-1.64 ± 0.05	2.42 ± 0.03
$Pb_{15}Ge_{27}Se_{48}$ Te_{10}	-1.47 ± 0.05	2.37 ± 0.03	$Pb_{20}Ge_{24}Se_{46}$ Te_{10}	-1.99 ± 0.06	2.68 ± 0.03

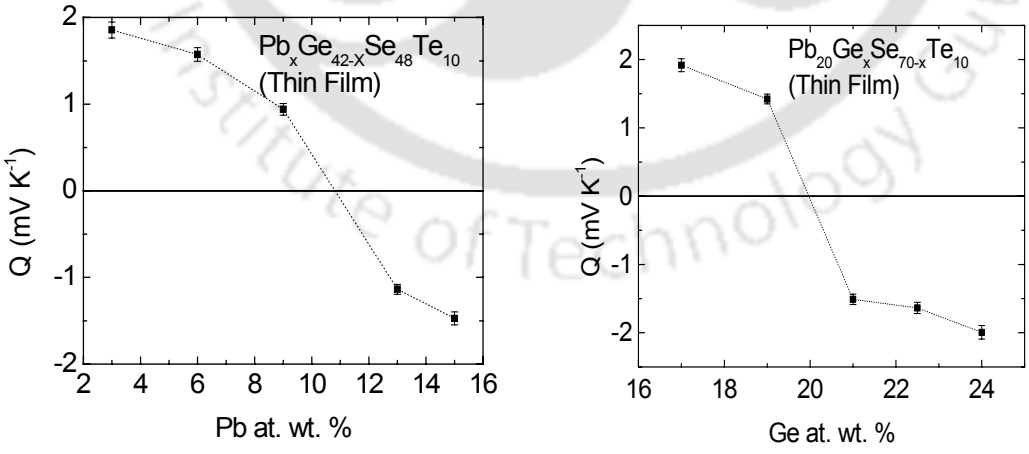

Figure 4.10: Composition dependence of TEP of Pb-Ge-Se-Te thin films.

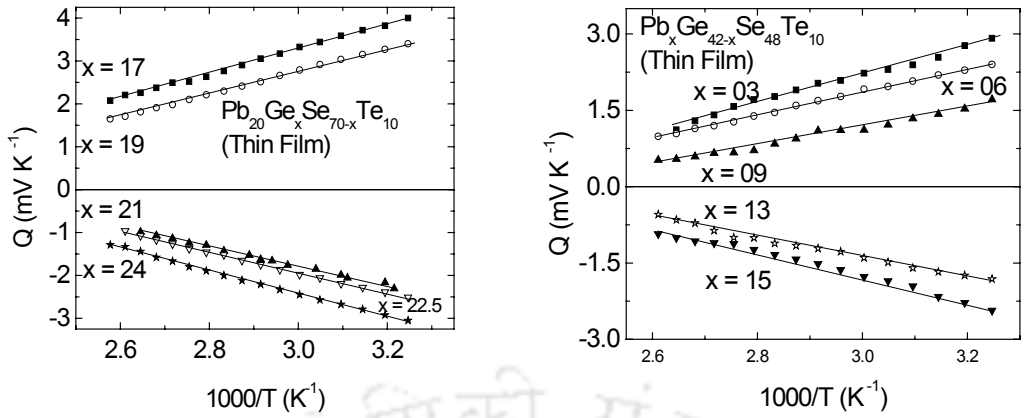

Figure 4.11: Temperature dependence of TEP of Pb-Ge-Se-Te thin films

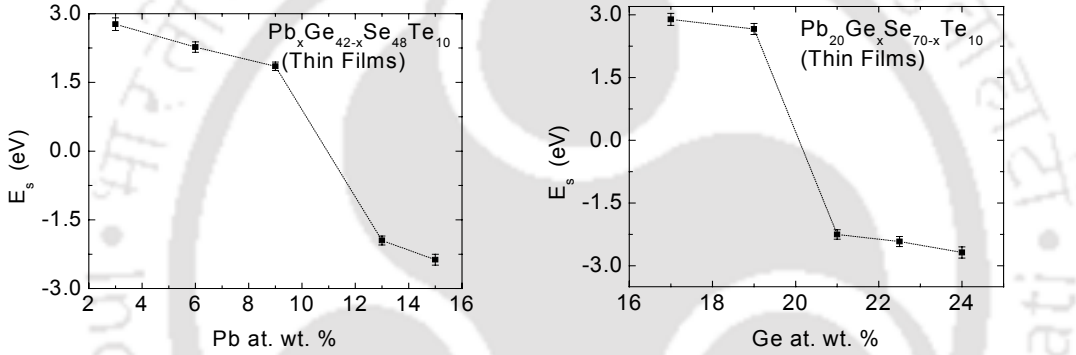

Figure 4.12: Compositional dependence of activation energy for thermal conduction in Pb-Ge-Se-Te thin films.

In the case of chalcogen atoms (Se or Te) the triply and singly co-coordinated defect states are C_3^+ and C_1^- respectively. One can consider C_3^+ as a hole-bearing atom. X-ray studies have confirmed [162] that Pb exists as Pb^{2+} in lead chalcogenide glasses. On addition of Pb to Ge-Se glasses, Pb^{2+} converts some C_3^+ into C_1^-, whereas, the number of Ge_3^- remains unaffected. As the number of C_3^+ decreases, the number of holes generated at the time of thermal excitation also decreases. Simultaneously, the number of negative charge defect states C_1^- increases. This results in the reduction of hole generating (triply co-ordinated positively charged) defect states and at the same time increases the number of electron generating

(singly co-ordinated negatively charged) defect states. This disturbance in the concentration of the VAPs culminates in the unpinning of the Fermi level and shifts it towards the conduction band. In this manner, one can account for the *p*- to *n*- type transition observed in these glasses with the addition of Pb. SEM studies on Pb-Ge-Se-Te glasses do not show any evidence of structural inhomogeneities at sub-micron scales. Hence percolation of microcrystalline clusters does not seem to be a plausible model for the conduction type change in these glasses. In the case of $Pb_{20}Ge_xSe_{70-x}Te_{10}$ glasses, Pb and Te concentration remains constant whereas Ge atoms gradually replace Se atom. The effect of Pb in suppressing C_3^+ defect states has already been discussed. When replaces Se, Ge_3^- states increase in number gradually depleting C_3^+. Effectively, the positive charge defect state responsible for the generation of holes reduces in number, resulting in the alternation of charge defect states. This unpins the Fermi level and shifts it towards the conduction band. The effect of Te substitution of Se manifests in the higher Q and E_s values of these glasses as compared to the Pb-Ge-Se glasses.

4. 4. Electrical conductivity

The d.c. electrical conductivity of bulk Pb-Ge-Se-Te glasses was measured from 348 K to 425 K and that of the glassy films from 313 K to 400 K. The electrical resistivity of the bulk samples as well as thin films at 348 K are tabulated in the table 4.6 and 4.7 respectively. The bulk resistivity and sheet resistant of series I and series II glasses are plotted as function of composition in figure [4.13] and figure [4.14] respectively. In the case of series I glasses, a slope change can be observed at the composition at which the carrier reversal occurs. On the other hand, resistivity

and sheet resistant of series II glasses show maximum values at the MCCR composition.

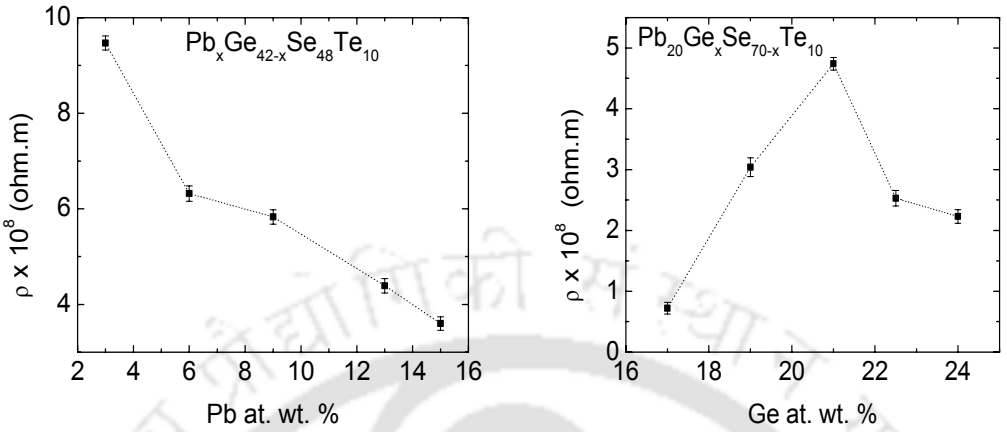

Figure 4.13: Variation of electrical resistivity with composition of bulk Pb-Ge-Se-Te glasses.

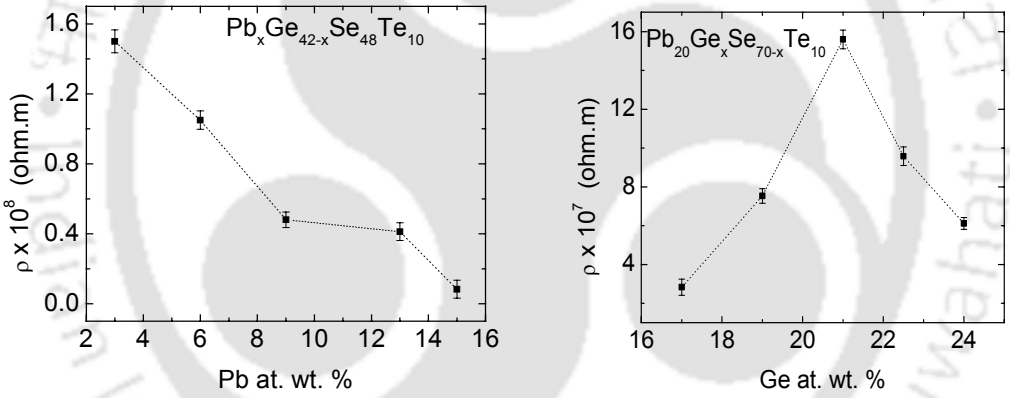

Figure 4.14: Resistivity of Pb-Ge-Se-Te thin films

Similar change in slope in resistivity versus composition plot of Pb-Ge-Se-Te glasses has been reported [136]. The present values of resistivity are lower than those reported by Murugavel *et al* since the data quoted correspond to higher temperature (348 K) (where the earlier data correspond to measurements at 298 K). Our data was limited to 313 K due to the high resistance of the samples.

ln(σ) versus 1000/T plots for data taken in the temperature range of 345 K to 425 K for all the glasses are shown in figure 4.15 and 4.16. The linearity of the plots

shows that there is a single conduction mechanism, namely, band transport is responsible for the electronic conduction in this temperature range. The activation energy for electrical conduction calculated from the slope of plots shown in figure 4.15 and 4.16 are tabulated in table 4.6. The variation of the activation energy for electrical conduction (E_σ) of bulk of Pb-Ge-Se-Te glasses with composition is shown in figure 4.17. ln(σ) versus 1000/T plots for thin film of Pb-Ge-Se-Te glasses are shown in figure 4.19 and figure 4.20. Similarly, activation energy for electrical conduction E_σ for thin films can be calculated from the slope of ln(σ) versus 1000/T plots. Composition dependence of E_σ is shown in figure 4.18. E_σ of bulk and thin film of series I and series II glasses show the same features exhibited by resistivity and sheet resistant as a function of composition. In the case of series I glass, the drastic decrease in E_σ (for bulk and thin film) shows that the electrical conduction is more favoured for *n*-type glass as compare to *p*-type glass. The data of Murugavel *et al* (table 4.6) support this argument. The linearity of these ln(σ) versus 1000/T confirms that the electronic conduction is due to the band transport mechanism, in which the electron in the extended state behaves as a conduction electron. However, the composition dependence of resistivity of the thin film show the same decreasing trend with the addition of Pb (in $Pb_xGe_{42-x}Se_{48}Te_{10}$ glasses) and Ge (in $Pb_{20}Ge_xSe_{70-x}Te_{10}$ glasses) as the bulk glasses. Reported data for $Pb_xGe_{42-x}Se_{48}Te_{10}$ glasses at 300 K are given within parentheses [136] for comparison.

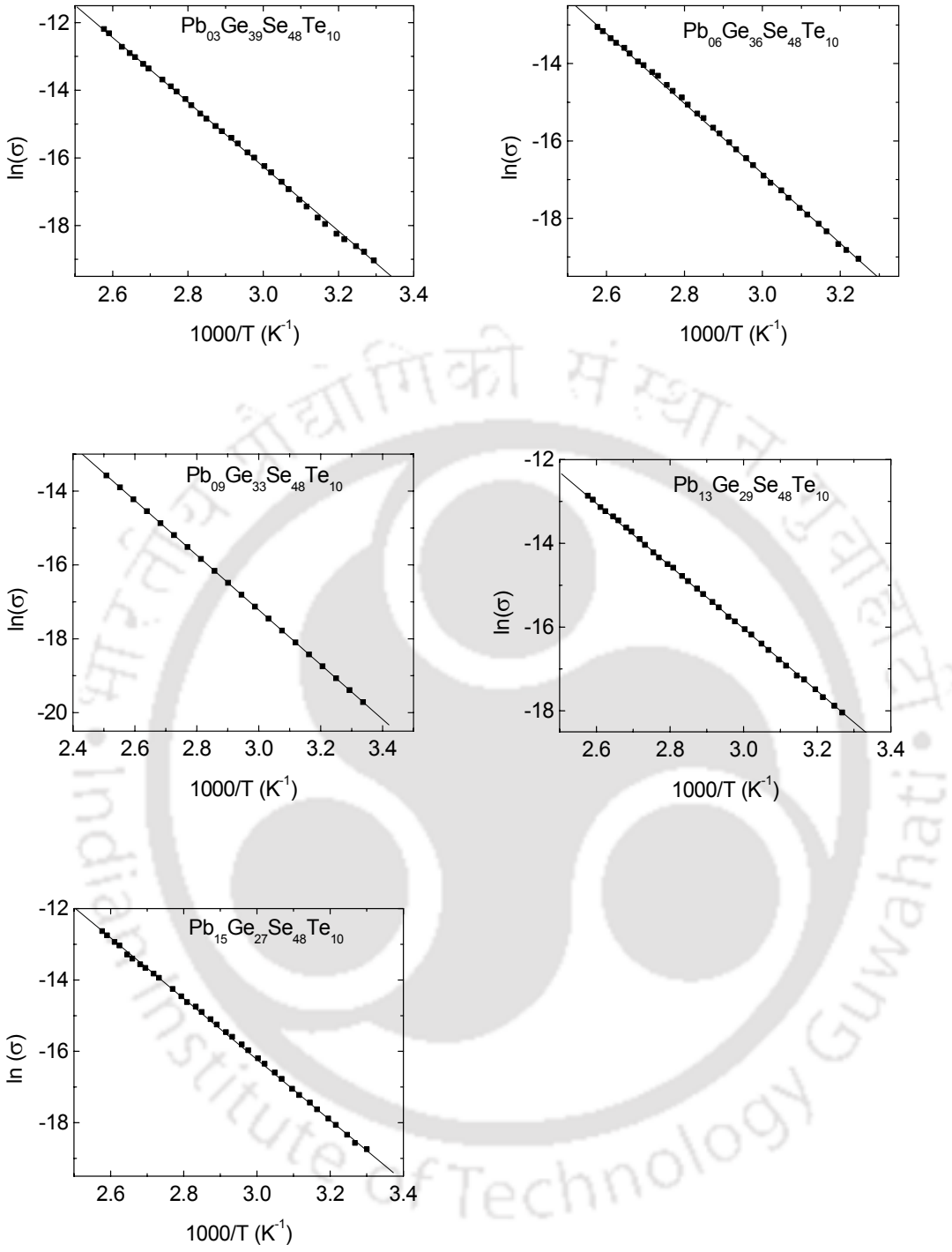

Figure 4.15: ln(σ) versus 1000/T of bulk $Pb_xGe_{42-x}Se_{48}Te_{10}$ glasses.

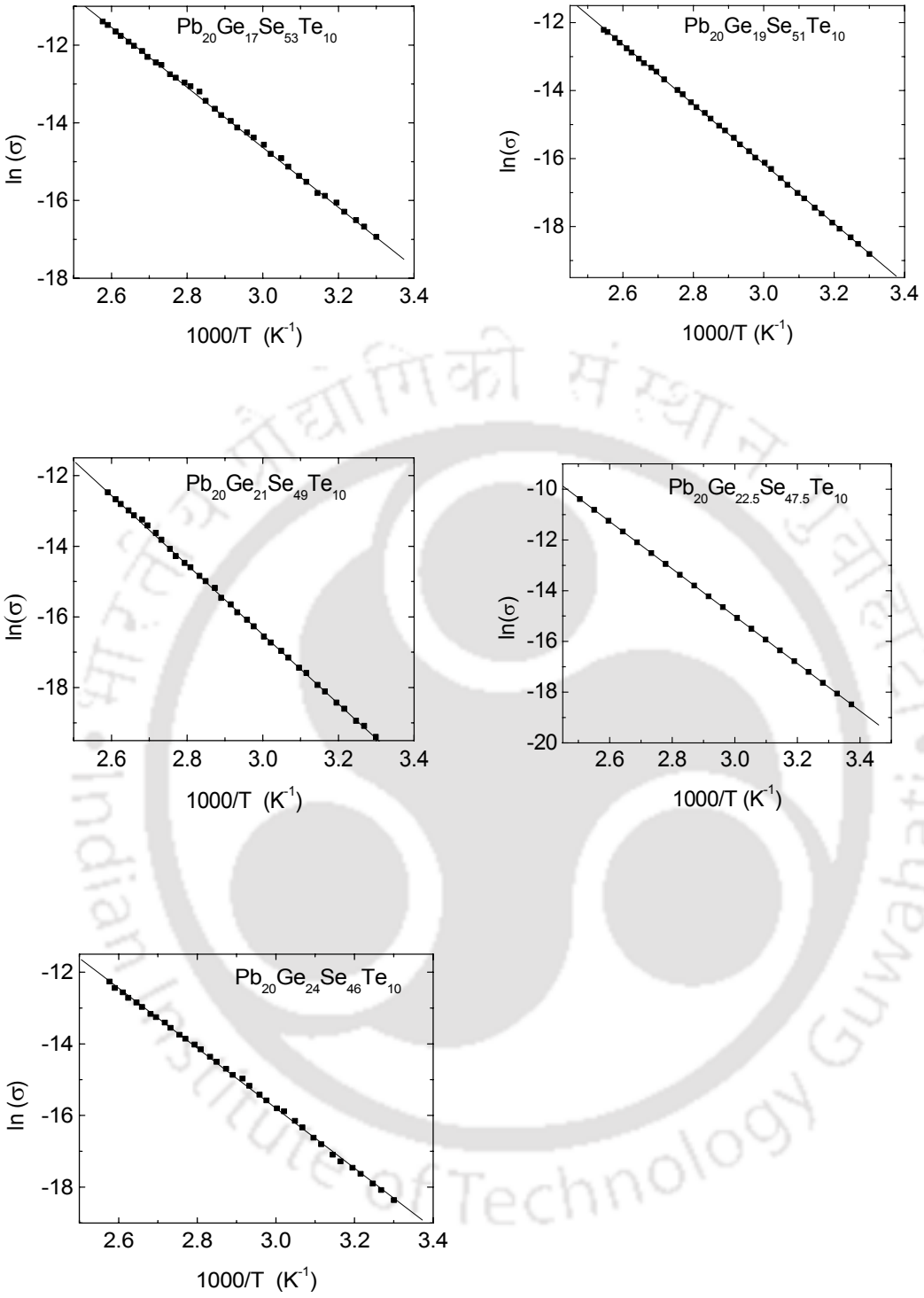

Figure 4.16: ln(σ) versus 1000/T of $Pb_{20}Ge_xSe_{70-x}Te_{10}$ bulk glasses.

Table 4.6: Resistivity ρ, Activation energy for electrical conduction E_σ of bulk Pb-Ge-Se-Te glasses. Data given within parentheses are from [136].

Bulk sample composition	ρ (ohm.m)	E_σ (eV)	Bulk sample composition	ρ x 10^8 (ohm.m)	E_σ (eV)
$Pb_{03}Ge_{39}Se_{48}Te_{10}$	9.47 x 10^8 ± 0.28	0.85 ± 0.01	$Pb_{20}Ge_{17}Se_{53}Te_{10}$	0.72 ± 0.02	0.70 ± 0.01
$Pb_{05}Ge_{37}Se_{48}Te_{10}$	(1.0 x 10^{10})	(0.98)	$Pb_{20}Ge_{19}Se_{51}Te_{10}$	3.04 ± 0.09	0.79 ± 0.01
$Pb_{06}Ge_{36}Se_{48}Te_{10}$	6.32 x 10^8 ± 0.19	0.81 ± 0.01	$Pb_{20}Ge_{21}Se_{49}Te_{10}$	4.74 ± 0.14	0.88 ± 0.01
$Pb_{09}Ge_{33}Se_{48}Te_{10}$	5.83 x 10^8 ± 0.17	0.79 ± 0.01	$Pb_{20}Ge_{22.5}Se_{47.5}Te_{10}$	2.53 ± 0.08	0.83 ± 0.01
$Pb_{10}Ge_{32}Se_{48}Te_{10}$	(1.1 x 10^9)	(0.70)	$Pb_{20}Ge_{24}Se_{46}Te_{10}$	2.23 ± 0.07	0.75 ± 0.01
$Pb_{13}Ge_{29}Se_{48}Te_{10}$	4.39 x 10^8 ± 0.13	0.72 ± 0.01			
$Pb_{15}Ge_{27}Se_{48}Te_{10}$	3.60 x 10^8 ± 0.11	0.69 ± 0.01			
$Pb_{15}Ge_{27}Se_{48}Te_{10}$	(5.4 x 10^7)	(0.59)			

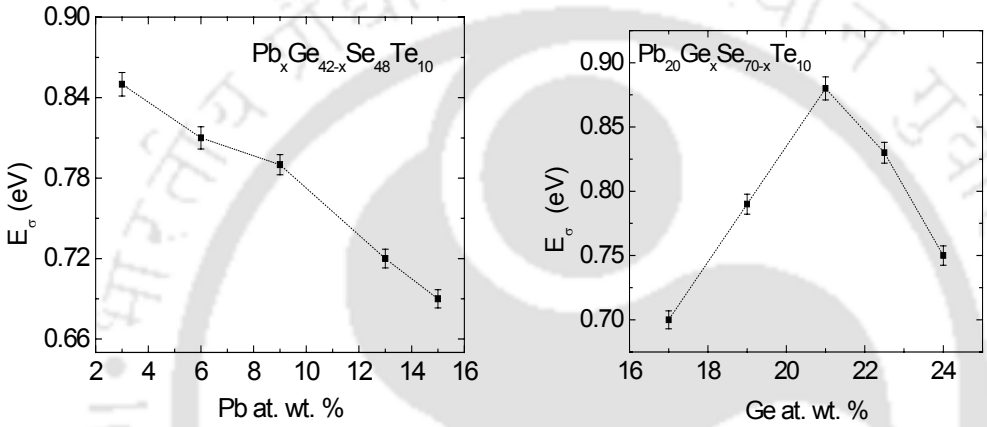

Figure 4.17: composition dependence of activation energy for electrical conduction (E_σ) in Pb-Ge-Se-Te glasses.

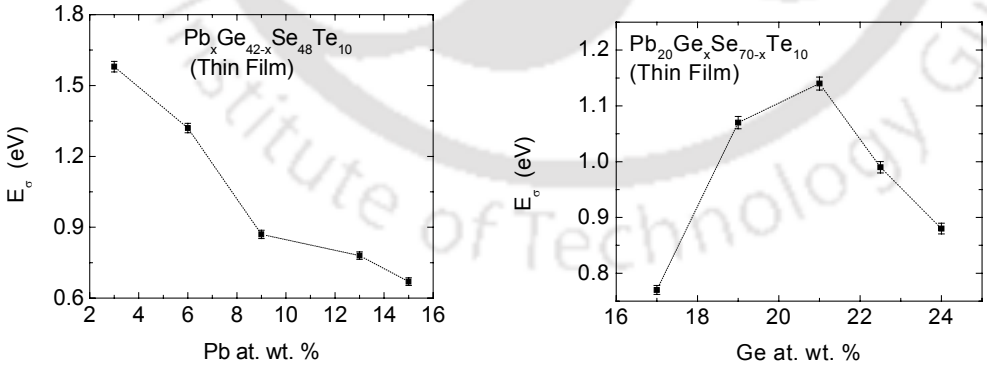

Figure 4.18: Composition dependence of activation energy for electrical conduction (E_σ) in Pb-Ge-Se-Te thin films.

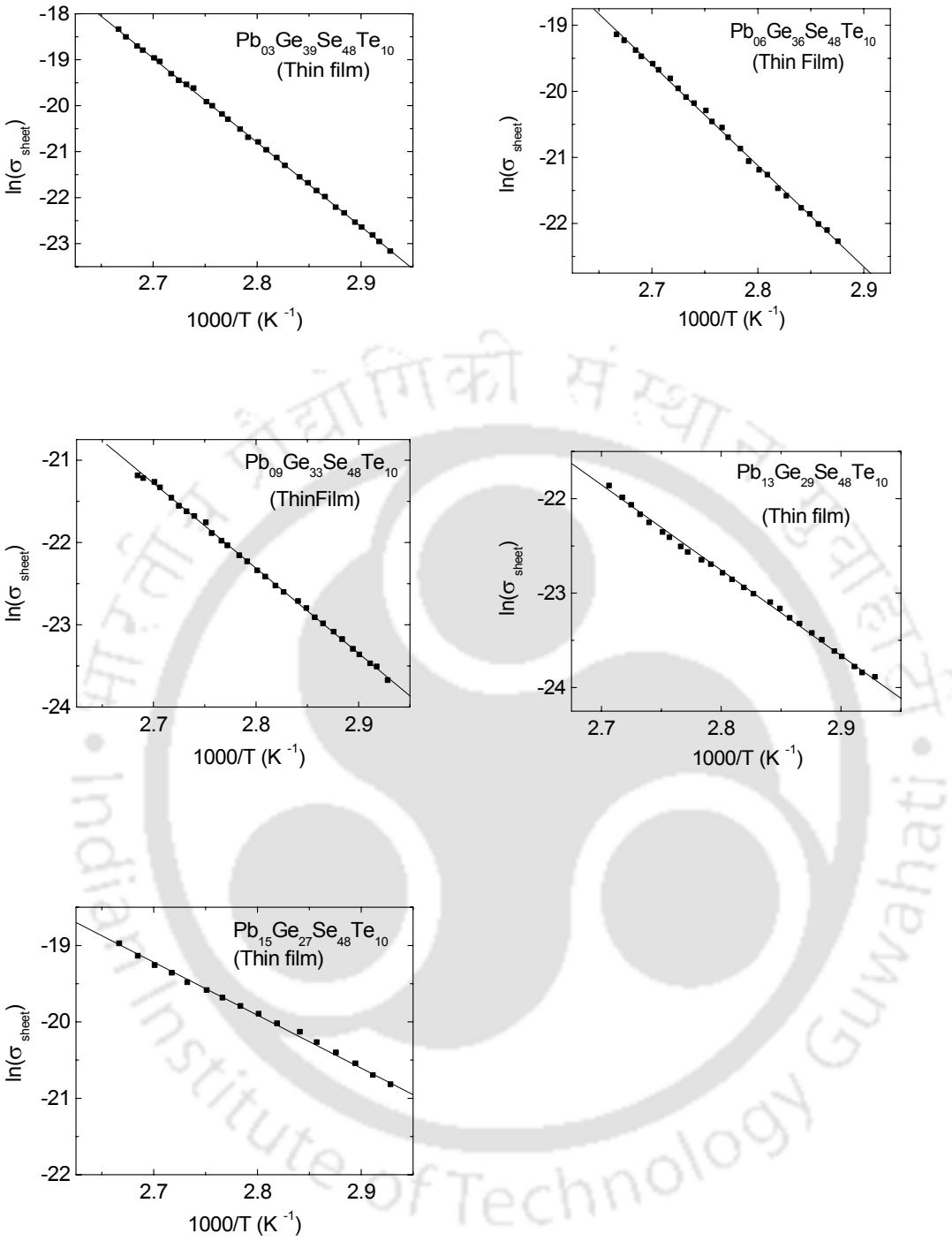

Figure 4.19: ln(σ) versus 1000/T plots of $Pb_xGe_{42-x}Se_{48}Te_{10}$ thin films.

Table 4.7: ρ_s and E_σ of Pb-Ge-Se-Te thin films.

Thin film composition	ρ_s (ohm. m)	E_σ (eV)	Thin film composition	$\rho_s \times 10^7$ (ohm. m)	E_σ (eV)
$Pb_{03}Ge_{39}Se_{48}$ Te_{10}	1.50 x 10^8 ± 0.05	1.58 ± 0.04	$Pb_{20}Ge_{17}Se_{53}$ Te_{10}	2.83 ± 0.08	0.77 ± 0.04
$Pb_{06}Ge_{36}Se_{48}$ Te_{10}	1.05 x 10^8 ± 0.03	1.32 ± 0.04	$Pb_{20}Ge_{19}Se_{51}$ Te_{10}	7.53 ± 0.22	1.07 ± 0.04
$Pb_{09}Ge_{33}Se_{48}$ Te_{10}	4.82 x 10^7 ± 0.02	0.87 ± 0.04	$Pb_{20}Ge_{21}Se_{49}$ Te_{10}	15.6 ± 0.46	1.14 ± 0.04
$Pb_{13}Ge_{29}Se_{48}$ Te_{10}	4.12 x 10^7 ± 0.02	0.78 ± 0.04	$Pb_{20}Ge_{22.5}Se_{47.5}$ Te_{10}	9.58 ± 0.28	0.99 ± 0.04
$Pb_{15}Ge_{27}Se_{48}$ Te_{10}	8.33 x 10^6 ± 0.01	0.67 ± 0.04	$Pb_{20}Ge_{24}Se_{46}$ Te_{10}	6.11 ± 0.20	0.88 ± 0.04

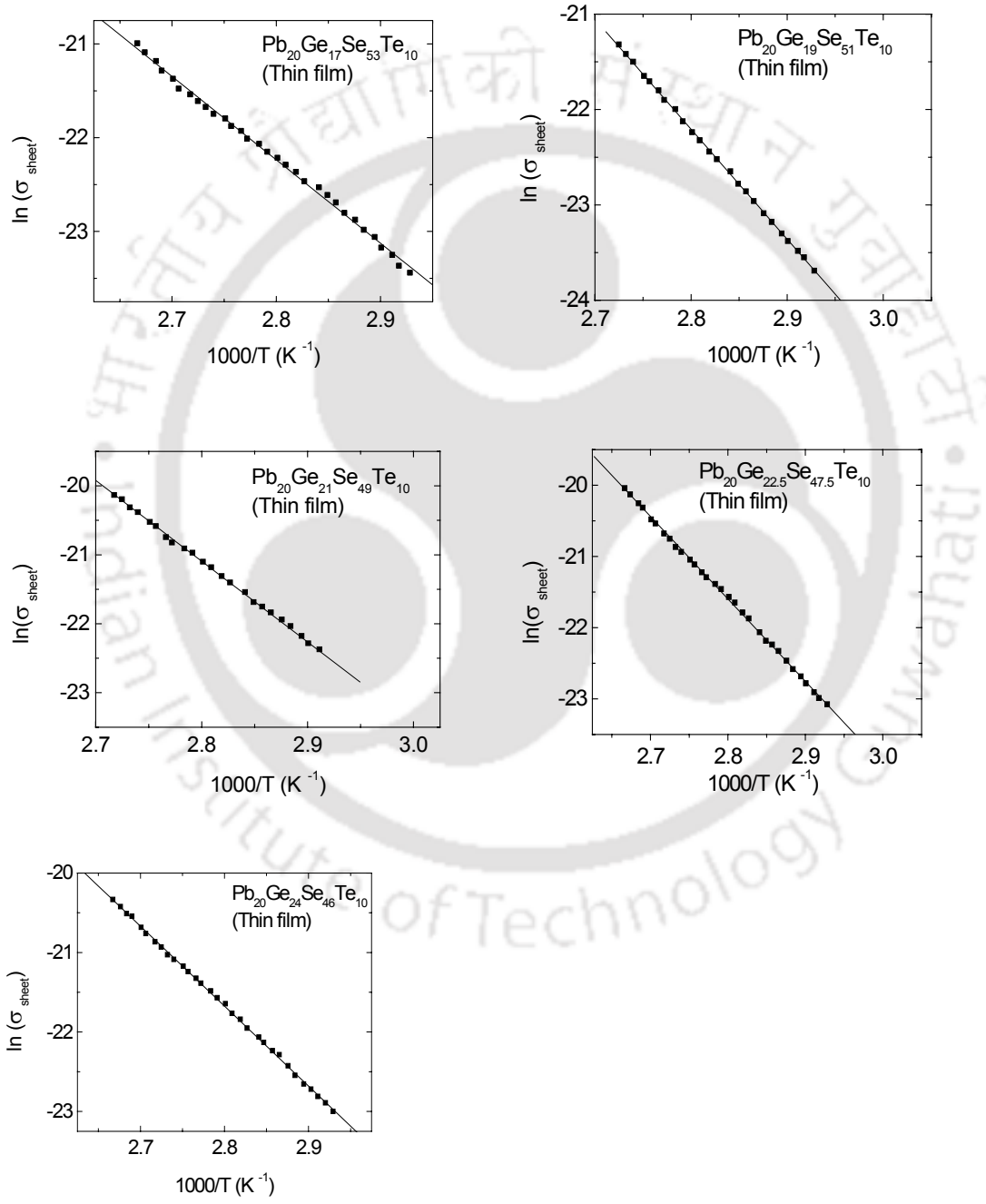

Figure 4.20: ln(σ) versus 1000/T plots of $Pb_{20}Ge_xSe_{70-x}Te_{10}$ thin films

4.5. Optical absorption

The optical band gap (E_{opt}) of Pb-Ge-Se-Te glasses was determined from optical absorption data as explained in chapter 2. The linear fit to $(\alpha h\nu)^{1/2}$ versus hν curves, extrapolated to $(\alpha h\nu)^{1/2} = 0$ gave the optical band gap energy values of these glass. E_{opt} calculated for $Pb_xGe_{42-x}Se_{48}Te_{10}$ and $Pb_{20}Ge_xSe_{70-x}Te_{10}$ glasses in thin film form are shown in table 4.8. Figure 4.21 and figure 4.22 shows the $(\alpha h\nu)^{1/2}$ versus hν plots for thin films for Pb-Ge-Se-Te glasses. The variation of E_{opt} with composition is shown in figure 4.23.

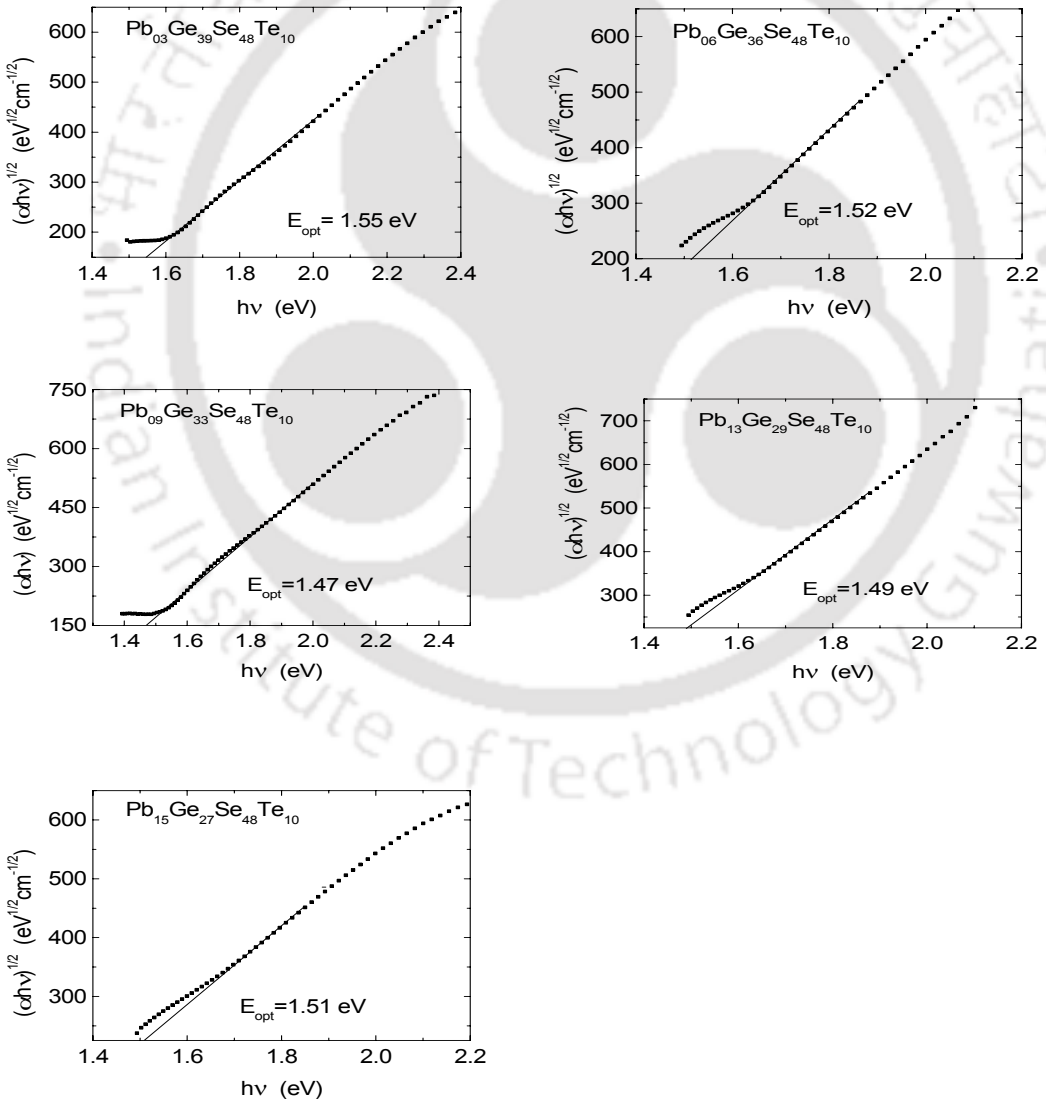

Figure 4.21: $(\alpha h\nu)^{1/2}$ versus hν plots for $Pb_xGe_{42-x}Se_{48}Te_{10}$ thin films.

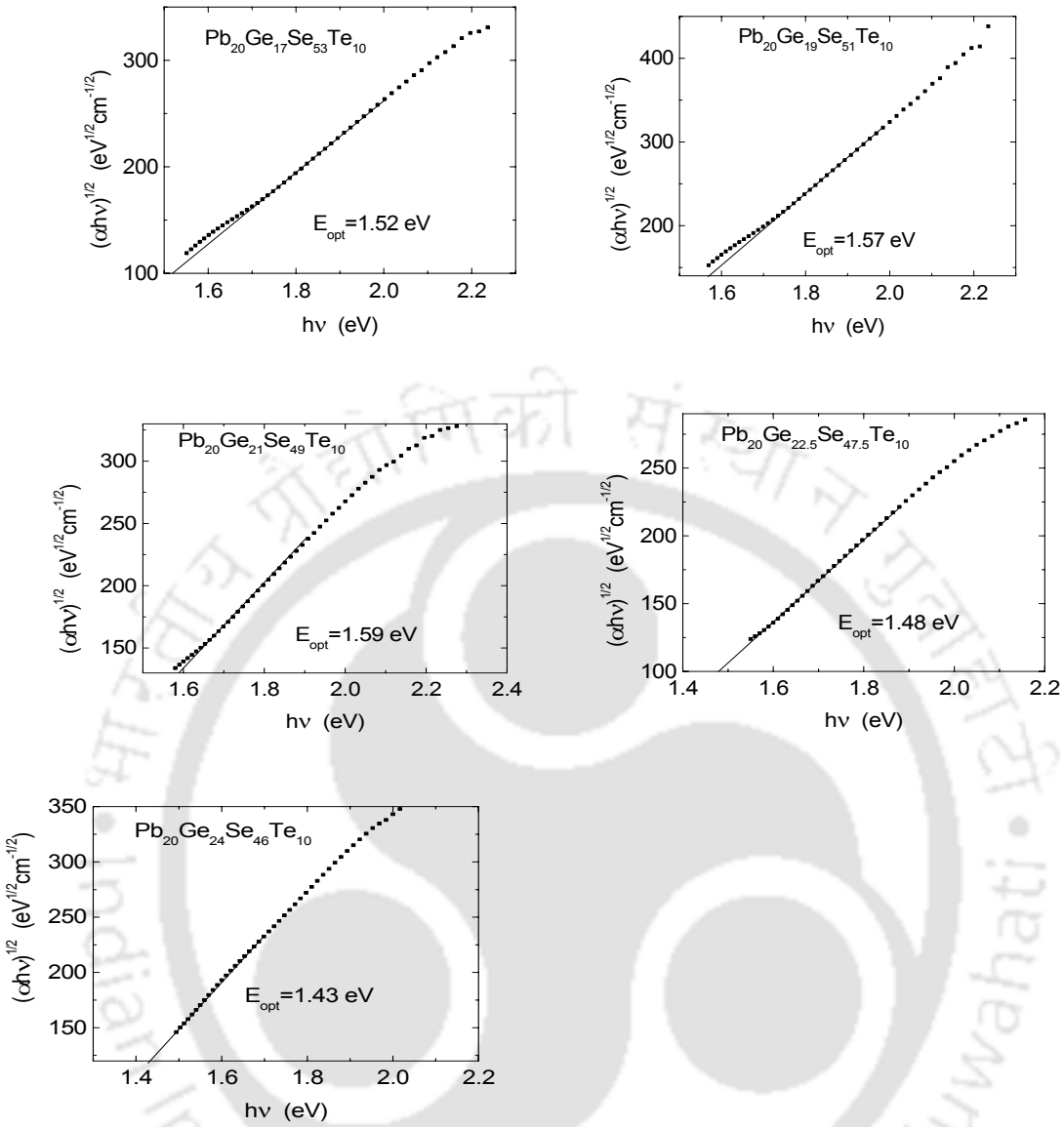

Figure 4.22: $(\alpha h\nu)^{1/2}$ versus hν plots for $Pb_{20}Ge_xSe_{70-x}Te_{10}$ thin films.

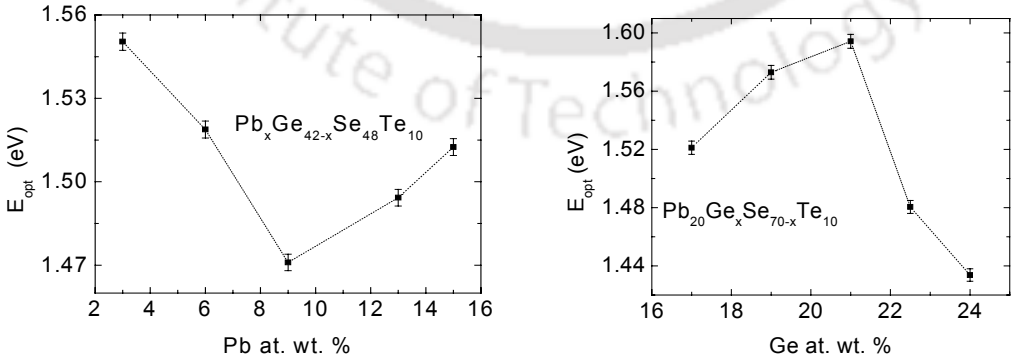

Figure 4.23: Variation of optical band gap with composition for Pb-Ge-Se-Te thin films.

Table 4.8: Optical band gap energy of Pb-Ge-Se-Te thin films.

Sample composition	E_{opt} (eV)	Sample composition	E_{opt} (eV)
$Pb_{03}Ge_{39}Se_{48}Te_{10}$	1.55 ± 0.01	$Pb_{20}Ge_{17}Se_{53}Te_{10}$	1.52 ± 0.01
$Pb_{06}Ge_{36}Se_{48}Te_{10}$	1.52 ± 0.01	$Pb_{20}Ge_{19}Se_{51}Te_{10}$	1.57 ± 0.01
$Pb_{09}Ge_{33}Se_{48}Te_{10}$	1.47 ± 0.01	$Pb_{20}Ge_{21}Se_{49}Te_{10}$	1.59 ± 0.01
$Pb_{13}Ge_{29}Se_{48}Te_{10}$	1.49 ± 0.01	$Pb_{20}Ge_{22.5}Se_{47.5}Te_{10}$	1.48 ± 0.01
$Pb_{15}Ge_{27}Se_{48}Te_{10}$	1.51 ± 0.01	$Pb_{20}Ge_{24}Se_{46}Te_{10}$	1.43 ± 0.01

The variation of E_{opt} of $Pb_{20}Ge_xSe_{70-x}Te_{10}$ glasses with Ge at. wt. % could be understood on the basis of the variation in the average bond energy of the glasses. Since Te remains constant in both series of Pb-Ge-Se-Te glasses, the variation in average bond energy of the glass is only due to the variation in Pb, Ge and Se in these glasses. So, in principle the average bond should show the same behaviour as in the case of Pb-Ge-Se glasses. In section 3.2 of chapter 3, it was showed that the average bond energy of series II glasses is maximum near $Pb_{20}Ge_{21}Se_{59}$. This results in the maximum E_{opt} depicted in figure 4.23 for $Pb_{20}Ge_xSe_{70-x}Te_{10}$ glass. In the case of $Pb_xGe_{42-x}Se_{48}Te_{10}$ glasses the average bond energy decreases and attains a minimum near 9 at. wt. % Pb. This accounts for the minimum in E_{opt} at the composition depicted in figure 4.23. In order to verify the validity of the above arguments, the E_{opt} of the Pb-Ge-Se-Te glasses may be compared with the corresponding Pb-Ge-Se glasses. E_{opt} of Pb-Ge-Se-Te glasses would be lower in all cases since low energy Te bonds reduce the average bond energy and hence the E_{opt} of Pb-Ge-Se-Te glasses.

4.6. Microhardness

The microhardness of bulk Pb-Ge-Se-Te glasses has been measured by the procedure already described in second chapter. Vickers hardness number (VHN) values corresponding to various Pb-Ge-Se-Te glass compositions are tabulated in table 4.9. Figure 4.24 shows the variation of VHN values of Pb-Ge-Se-Te glasses

with composition. Microhardness is a bond sensitive property [3]. Variation in VHN of both series of Pb-Ge-Se-Te glasses would then be interpreted in same line as the composition dependence of E_{opt} and T_g. Thus the decrease in VHN with addition of Pb in series I glasses and the maximum at 21 at. wt. % Ge in series II glasses are a consequence of the magnitude of the average bond energy of the respective glass composition. Comparison of the Pb-Ge-Se-Te microhardness data with that of Pb-Ge-Se would reveals that the microhardness of Pb-Ge-Se-Te glass is lower than the corresponding Pb-Ge-Se glasses as expected.

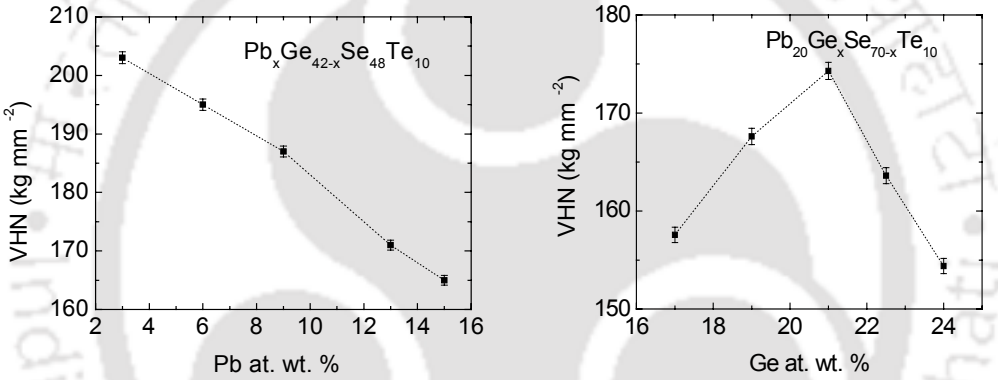

Figure 4.24: Variation of Vickers Hardness Number of bulk Pb-Ge-Se-Te glasses with composition.

Table 4.9: Vickers Hardness Number (VHN) of Pb-Ge-Se-Te bulk glasses.

Sample composition	VHN (kg.mm^{-2})	Sample composition	VHN (kg.mm^{-2})
$Pb_{03}Ge_{39}Se_{48}Te_{10}$	203 ± 4	$Pb_{20}Ge_{17}Se_{53}Te_{10}$	158 ± 4
$Pb_{06}Ge_{36}Se_{48}Te_{10}$	195 ± 4	$Pb_{20}Ge_{19}Se_{51}Te_{10}$	168 ± 4
$Pb_{09}Ge_{33}Se_{48}Te_{10}$	187 ± 4	$Pb_{20}Ge_{21}Se_{49}Te_{10}$	174 ± 4
$Pb_{13}Ge_{29}Se_{48}Te_{10}$	171 ± 4	$Pb_{20}Ge_{22.5}Se_{47.5}Te_{10}$	164 ± 4
$Pb_{15}Ge_{27}Se_{48}Te_{10}$	165 ± 3	$Pb_{20}Ge_{24}Se_{46}Te_{10}$	154 ± 4

4.7. Summary

The highlights of the results obtained from the studies performed on Pb-Ge-Se-Te can be summarized as follows:

1. DSC studies show that T_g does not vary much after 9 at. wt. % Pb for $Pb_xGe_{42-x}Se_{48}Te_{10}$ glasses and reaches a maximum value at 21 at. wt. % Ge for $Pb_{20}Ge_xSe_{70-x}Te_{10}$ glasses. The degree of fragility (m) and the excess heat capacity (ΔC_p) reflect that the composition at which carrier type reversal occurs is kinetically stronger and thermodynamically stronger then the rest of the glass compositions.
2. TEP measurement on these glasses revealed that bulk glasses with $x \geq 9$ at. wt. % Pb and $x \geq 21$ at. wt. % Ge in $Pb_xGe_{42-x}Se_{48}Te_{10}$ and $Pb_{20}Ge_xSe_{70-x}Te_{10}$ glasses respectively showed *n*-type conduction, whereas, in case of the thin films $Pb_{09}Ge_{33}Se_{48}Te_{10}$ glass also showed *n*-type conduction. This carrier type reversal phenomenon is explained on the basis of change in the charge carrier concentration of charged defect states with the addition of Pb.
4. Optical band gap energy and microhardness showed the same behaviour as that of glass transition temperature because they are all bond sensitive properties.
5. d.c. electrical conductivity studies showed that resistivity (ρ) and activation energy (E_σ) for electrical conduction decreases in $Pb_xGe_{42-x}Se_{48}Te_{10}$ glass, with a slope change at the composition at which the carrier reversal was observed. In the case of $Pb_{20}Ge_xSe_{70-x}Te_{10}$ glasses (bulk and thin films), ρ and E_σ showed a maximum value at 21 at. wt. % Ge. Thin film had higher electrical conductivity value than the bulk samples.
6. An interesting outcome of the studies on Pb-Ge-Se-Te glasses is the influence of the substitution of Se with Te. Te substitution decrease the average bond energy

of the glasses, which in turn result in lower T_g, E_{opt} and VHN values. m and ΔC_p are also lower for Pb-Ge-Se-Te glasses, which suggests that Te substitution results in kinetically and thermodynamically strong glasses.

Chapter 5

Studies on bulk and thin films of Pb-In-Se

Recently Mehra *et al* [73] reported *p*- type to *n*-type carrier reversal in bulk $Pb_xIn_{25-x}Se_{75}$ glasses. This is interestingly the only reported bulk chalcogenide glass to exhibit *p*- to *n*- type carrier reversal phenomenon which does not contain Ge as one of its constituents. A report on the optical and electrical properties [73] and another on high pressure resistivity studies [137] published by the same research group showed that $Pb_xIn_{25-x}Se_{75}$ glasses with x ≥ 5 at. wt. % Pb showed *n*-type conduction. The carrier reversal phenomenon in this glass system has been attributed to changes in the network matrix of In-Se glasses induced by the addition of Pb. They reported that the Seebeck coefficient varied from 1.0 $mV.K^{-1}$ to -0.32 $mV.K^{-1}$ and the activation energy for the TEP (E_s) ranged from 0.73 eV to 0.15 eV on increasing Pb content from 0 to 15 at. wt. % in these glasses. The electrical conductivity measured at 273 K increased from 10^{-10} to 10^{-4} $ohm^{-1}.cm^{-1}$ and the activation energy for electrical conduction varied between 0.74 to 0.32 eV in these glasses. Glass transition temperature (T_g) increased with an increase in Pb content. Glass transition temperature (T_g) of these glasses have been reported [137] to lie between 325 K and 335 K when heated at $10^{\circ}Cmin^{-1}$. Data reported [73,137] on Pb-In-Se system are summarised in table 5.1.

Table 5.1: Reported data [73,137] on bulk Pb-In-Se glasses.

Sample composition	Q (mVK^{-1})	E_s (eV)	ρ at 273 K (ohm.m)	E_σ (eV)	E_{opt} (eV)	T_g (K)
$Pb_{00}In_{25}Se_{75}$	0.10	0.73	1.11×10^6	0.74	1.70	326
$Pb_{05}In_{20}Se_{75}$	-0.20	0.32	1.42×10^5	0.49	1.52	328
$Pb_{10}In_{15}Se_{75}$	-0.25	0.25	3.33×10^3	0.41	1.41	332
$Pb_{15}In_{10}Se_{75}$	-0.32	0.15	5.00×10^2	0.32	1.32	334

5.1. Preparation and characterization of samples

5.1.1. Preparation and characterization of bulk samples

Bulk samples of $Pb_xIn_{25-x}Se_{75}$ series of glasses with x = 1, 3, 5, 7 were prepared by the melt quenching technique as discussed in chapter 2. In order to verify the amorphous nature of the as-quenched glasses, X-ray diffraction patterns of the as-quenched were recorded over a 2θ range of 10º < 2θ < 70º. XRD patterns revealed a number of crystalline peaks showing that the sample was not entirely amorphous. XRD pattern of two Pb-In-Se quenched samples are shown in figure 5.1. The presence of crystalline phase(s) is clearly evident from the figure. Such an XRD pattern was obtained in the case of all the quenched samples.

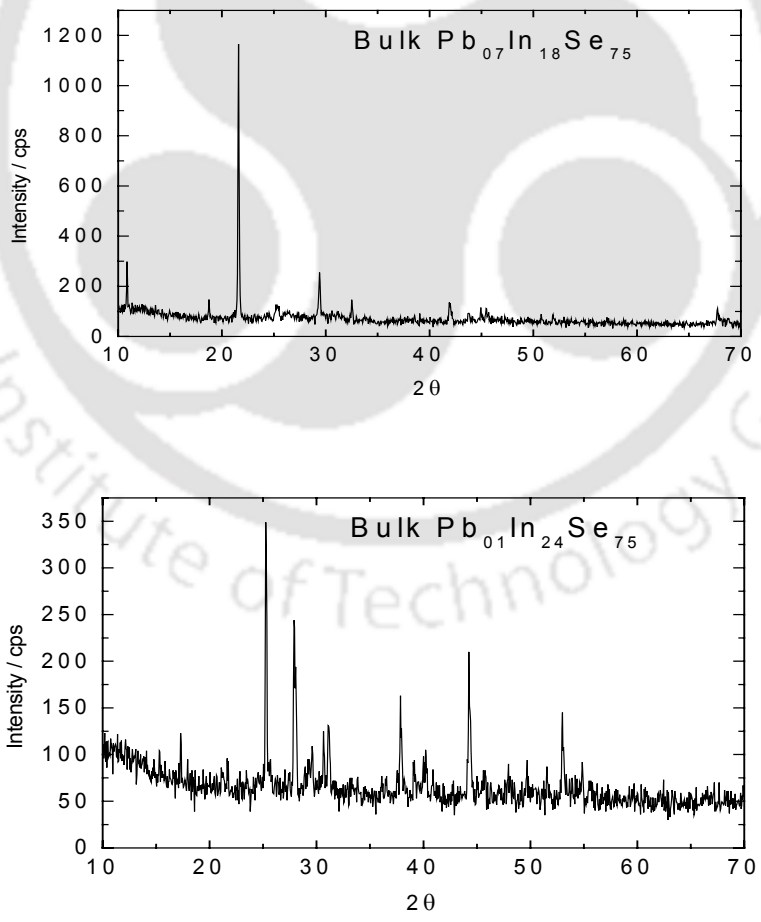

Figure 5.1: XRD patterns of melt quenched $Pb_{01}In_{24}Se_{75}$ and $Pb_{07}In_{18}Se_{75}$ bulk samples.

In order to obtain a completely amorphous sample, the following variations in the preparation procedure were adopted. (i) Reduction of weight of the powder to be melted, (ii) homogenization of the constituent powders by mixing prior to melting, (iii) varying the temperature from which the melt was quenched, (iv) varying the homogenization time between 10-15 hours, and (v) quenching the melt (in sealed ampoule) in liquid nitrogen. None of these efforts yielded a completely amorphous samples. This was surprising considering the two published papers on this system [73, 137]. T_g and thermoelectric power of these partially amorphous bulk samples were measured for the sake of obtaining information about the nature of these materials.

DSC runs at 10°C.min^{-1} were performed. The DSC curves are shown in figure 5.2 and the corresponding data are given in table 5.2. DSC curves shown in figure 5.2 show that there is sufficient amount of glassy phase in the melt quenched material to record an observable glass transition temperature (T_g). This glass phase subsequently crystallized at (T_c) and then melted at T_m. From table 5.2 it can be seen than T_g shows hardly any variation with composition, a feature also pointed out by the data reported earlier [137]. The broad and weak crystallization peak signifies the spontaneous nucleation and growth of probably more than one crystalline phase. T_c shows a maximum for the $Pb_{05}In_{20}Se_{75}$ composition. A single T_m suggests that the same phase has melted at this temperature. The glass forming tendency (k_g) [164,165] is measure of the ease of glass formation, and is given by the expression,

$$k_g = \frac{T_c - T_g}{T_m - T_c} \qquad (5.1)$$

where T_g, T_c and T_m are the glass transition, crystallization and melting temperature of the glass. Equation 5.1 has been obtained under the assumption that the glass

forming tendency is proportional to the thermal stability of the glass. A lower k_g signifies a poor tendency to glassify. k_g values obtained from the present DSC data are given in table 5.2. From the k_g values, the $Pb_{05}In_{20}Se_{75}$ composition shows the highest glass forming tendency as compared to the rest of the compositions.

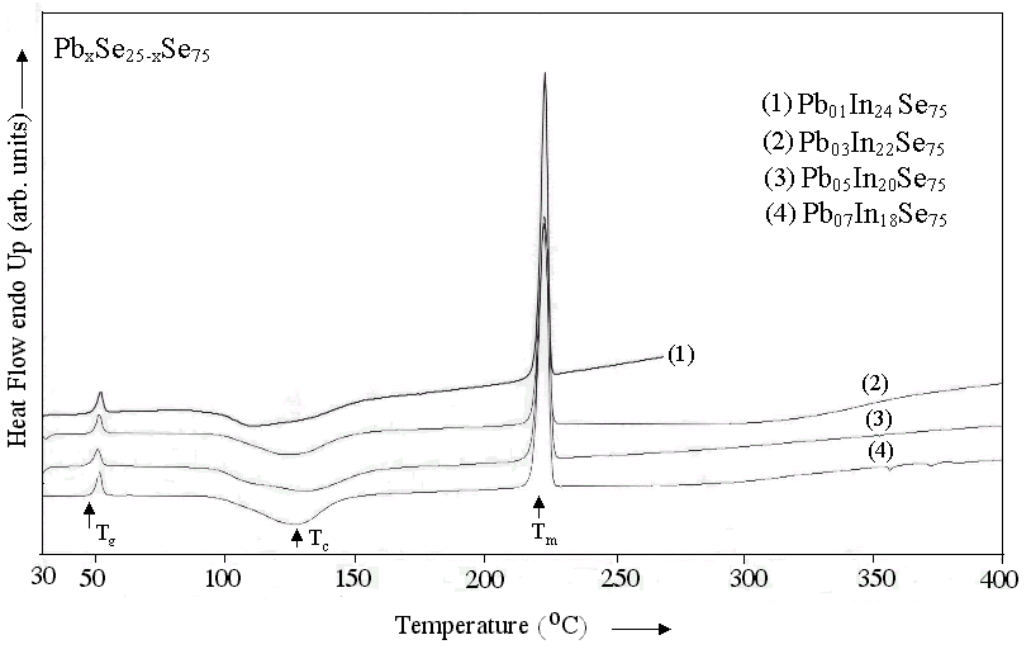

Figure 5.2: DSC curves of Pb-In-Se glasses recorded at a constant heating rate of 10 °C.min^{-1} [It may be noted that unlike the DSC curves shown in fig. 2.6, 3.4 and 4.2, these curves have been plotted such that endothermic deflections are upwards and exothermic deflections are downwards].

Table 5.2: DSC and TEP data obtained in the present studies on melt quenched bulk Pb-In-Se samples.

Sample composition	T_g (K)	T_c (K)	T_m (K)	k_g	Q
$Pb_{01}In_{24}Se_{75}$	323	387	496	0.64	positive
$Pb_{03}In_{22}Se_{75}$	323	397	496	0.75	negative
$Pb_{05}In_{20}Se_{75}$	321	404	496	0.89	negative
$Pb_{07}In_{18}Se_{75}$	323	400	496	0.82	negative

From the above studies on melt quenched (bulk) $Pb_xIn_{25-x}Se_{75}$ with x = 1, 3, 5, 7, it is clear that a completely amorphous phase could not be obtained in this system. It is however interesting to note that the partially crystallized $Pb_xIn_{25-x}Se_{75}$

alloys showed a *p*- type to *n*-type transition as reported earlier [73]. Since it is very difficult to quantify the results of such a partially crystallized bulk sample, further investigations were not carried out on the bulk samples.

5.1.2. Preparation and characterization of thin films

As the preparation of the Pb-In-Se glasses in the bulk form was not possible in the above mentioned method, attempts were made to prepare thin films of the same compositions. In order to prepare the starting material for deposition, weighed quantities of Pb, In and Se corresponding to desired composition were taken in fused silica ampoules. The ampoule was heated to 600ºC and homogenized at this temperature for 10 hours in the rotary furnace. Subsequently, the ampoule was cooled to room temperature. The alloy was powdered and used as the source for deposition. To verify the amorphous nature of the films deposited on microscope cover slips, XRD patterns were recorded in a X-ray diffractometer equipped with grazing incidence device. The XRD patterns of films deposited at about 310 K (during thermal evaporation the substrate holder temperature increases by 5º to 10º C above the ambient) showed two crystalline peaks in the range $10º < 2\theta < 70º$. In order to suppress the crystallization, the substrate was cooled by passing liquid nitrogen through a container kept in contact with the substrate holder. The temperature of the substrate holder (SH in figure 2.2) was measured with a calibrated PT100 sensor embedded on the substrate holder. Substrate temperature could be lowered to 200 K with such an arrangement. It was realized that mere reduction of temperature could not completely suppress the crystallization. However, the intensity of the two peaks reduced drastically signifying a reduction in nucleation of the crystalline phases. A corresponding broadening of the peaks with reduction in deposition temperature indicated a reduction in the size of the crystallites. The x-ray

diffractogram for two films deposited at different substrate temperature are shown in figure 5.3. XRD patterns corresponding to thin films of various compositions of Pb-In-Se are shown in figure 5.4.

After many attempts, it was confirmed that crystallinity could not be completely removed from the amorphous films of Pb-In-Se deposited by the above procedure. The presence of a small amount of crystallinity in the films as compared to the bulk specimen gave the encouragement to further characterize the as-deposited films of Pb-In-Se. XRD analysis [search match with International Centre for Diffraction Data (ICDD) database] showed that the two crystalline peaks appeared at the same 2θ values (44.4° and 51.6°) in the case of all the samples and showed a reasonably good match with the powder diffraction file (PDF) data on crystalline Selenium (PDF no. 85-568) with hexagonal structure [lattice parameter a =3.956, b = 5.069 with <hkl> = (0 1 2) and (1 1 -1) and corresponding 2θ values of 44.8° and 51.1° respectively and intensity values of 338 and 108 respectively]. Since no other combination of prospective elements (*viz.*, Pb, In, Se, O) gave any proximate match to these two peaks, it was presumed that crystalline Selenium in hexagonal structure is embedded in these amorphous films. The large width of the two peaks suggested that the size of these Se crystallites could be small.

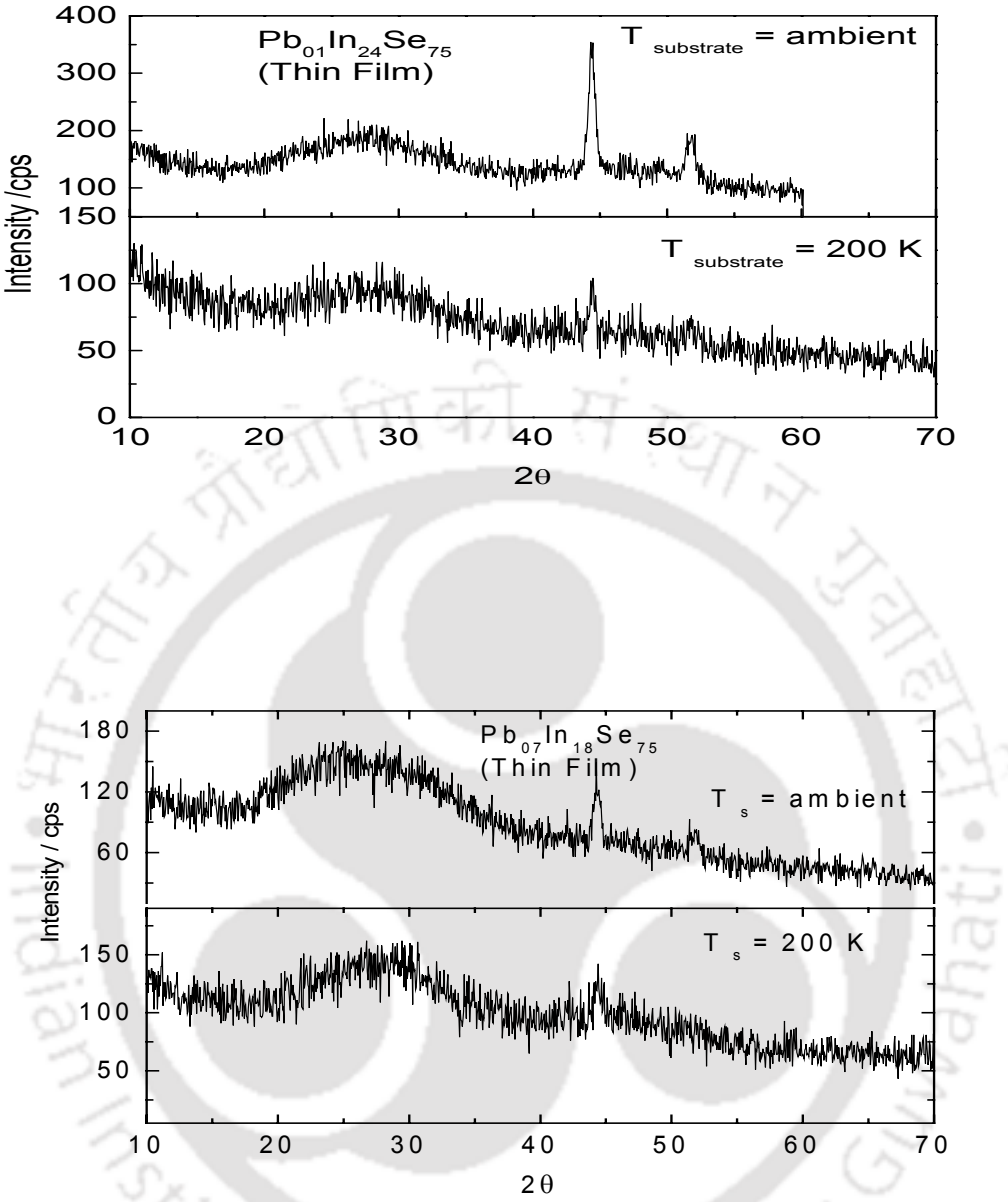

Figure 5.3: Thin films of the $Pb_{01}In_{24}Se_{75}$ and $Pb_{07}In_{18}Se_{75}$ deposited at different substrate temperatures (T_s). The two weak Bragg peaks and their intensity variation on cooling the substrate are illustrated in the figure.

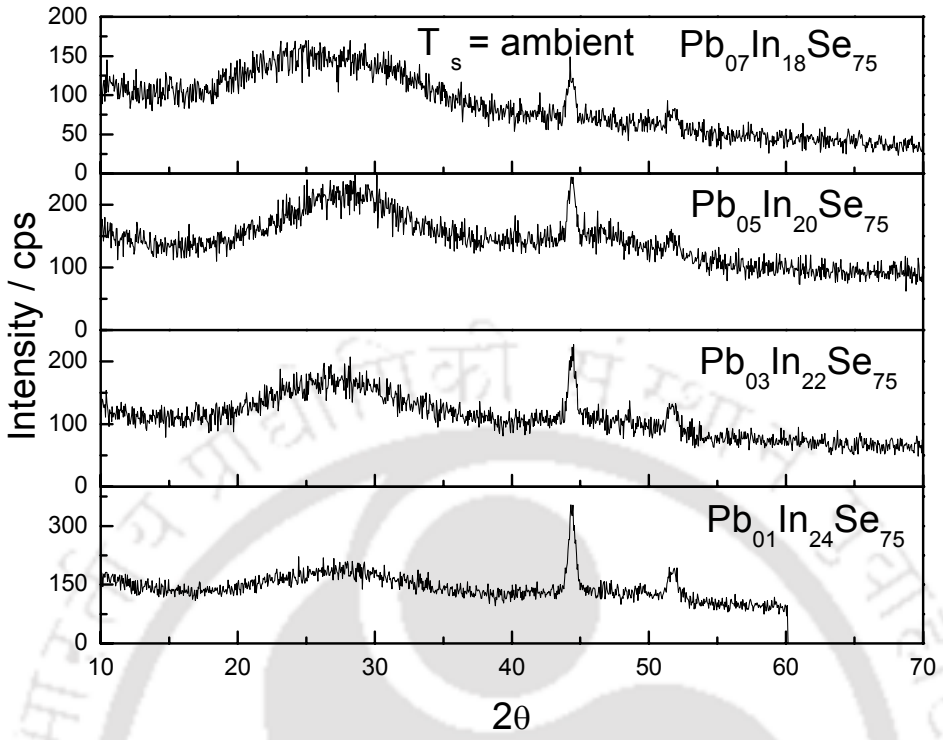

Figure 5.4: XRD pattern for all Pb-In-Se thin films deposited at ambient temperature (*i.e.*, without cooling the substrate).

From the XRD pattern, the Full Width Half Maximum (FWHM) (i.e. B) can be found by fitting a Lorentzian function and the corresponding peak profiles. The crystal size can be calculated using the Scherrer's formula [138]

$$t = \frac{0.9\lambda}{B\cos\theta_B}$$

where λ is the wavelength of X-rays, B is the FWHM and θ_B is the Bragg's angle. The crystal size corresponding to the first peak in Pb-In-Se glasses is shown in table 5.3. It was not possible to obtain a reasonable fit for the second (weak) Bragg peak. Sometimes a Voigt is used. Since the Lorentzian function gave a reasonably good fit to the experimental peaks, the Lorentzian function was used because of its simple form. Table 5.3 shows that the particle (crystallite) size decreases when the films are deposited at low temperatures. Low temperature deposition inhibits diffusion and

aggregation and hence the particle size decreases when deposited at low temperatures.

Table 5.3: Crystal size measured from XRD patterns of Pb-In-Se glasses at different substrate temperatures. Ambient means that the substrate holder is not cooled.

Sample composition	Substrate temperature	FWHM (B)	Position of the peak(2θ)	Crystal Size (Å)
$Pb_{01}In_{24}Se_{75}$	Ambient	0.596º	44.38º	144
	200 K	0.636º	44.41º	135
$Pb_{03}In_{22}Se_{75}$	Ambient	0.976º	44.39º	88
	200 K	--	--	--
$Pb_{05}In_{20}Se_{75}$	Ambient	0.548º	44.40º	156
	200 K	0.974º	44.38º	88
$Pb_{07}In_{18}Se_{75}$	Ambient	1.140º	44.30º	75
	200 K	--	--	--

The compositional analysis for these samples was done by the SEM-EDX. The composition of each sample was found to be identical to the bulk compositions with an uncertainty of ± 2 %. A typical SEM-EDX spectrum is shown in the figure 5.5. Figure 5.6 is a photograph of $Pb_{01}In_{24}Se_{75}$, which shows that nanometer sized crystallites of Se is embedded in this glass. The thickness of the films was measured by the ellipsometer and found to be within the range 1500 Å to 2000 Å.

From the above studies, it can be said that the Pb-In-Se films deposited are amorphous with a fine disperse of nanometer sized Se crystallites. The crystallite size could be reduced by depositing the films at a lower temperature. Precise characterization of the particle size could be done by transmission electron microscope (TEM) studies. Unfortunately, the candidate could not access a TEM. Moreover, the primary aim behind this investigation is to investigate the majority charge carrier phenomenon in Pb modified chalcogenide glasses. Hence, no further structural characterization was attempted beyond the ones mentioned above.

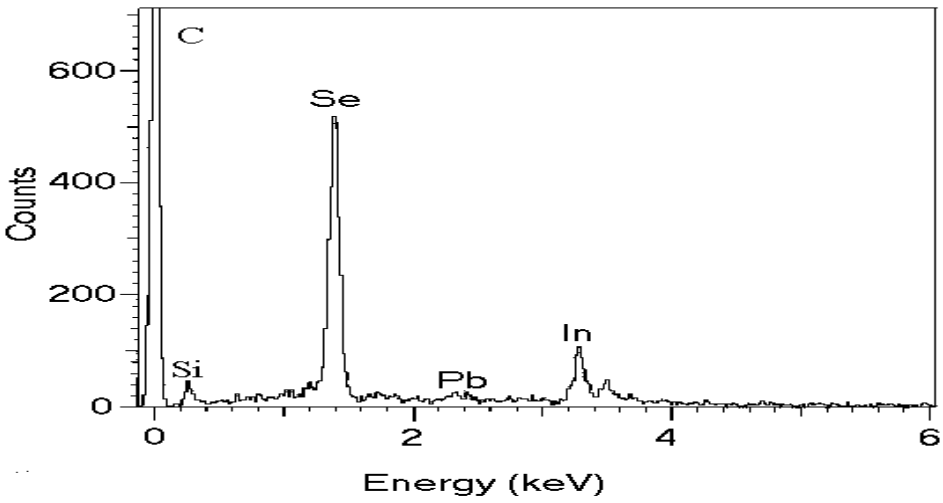

Figure 5.5: EDX spectrum for a Pb-In-Se thin film glass.

The majority charge carrier type in the all the samples was determined by TEP measurements. The details of the measurement technique were discussed earlier in chapter 2. From the Seebeck coefficient it was found that $Pb_1In_{24}Se_{75}$, glass composition as *p*-type and the rest were *n*-type semiconductors.

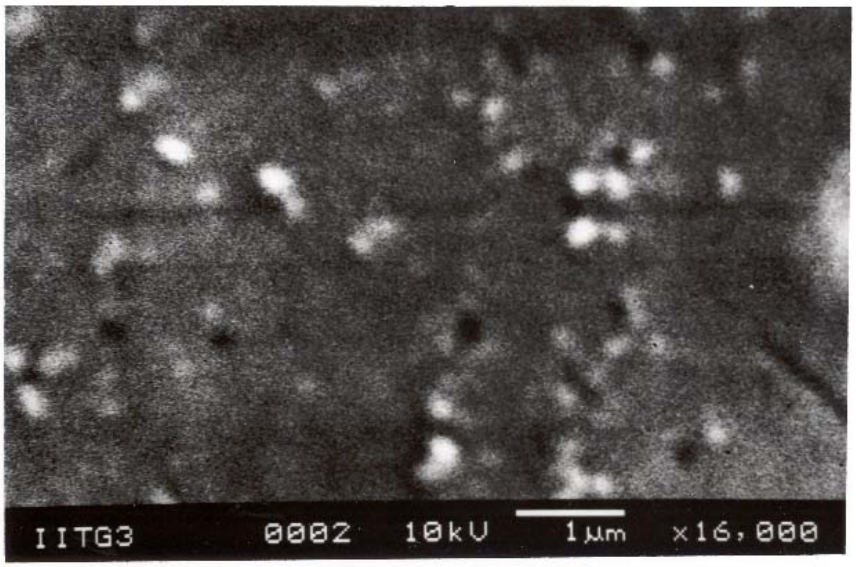

Figure 5.6: SEM photograph of $Pb_{01}In_{24}Se_{75}$ glass showing nanometer sized crystallites embedded in the amorphous matrix. The black spots are voids in the film.

5.2. Thermoelectric power

The thermoelectric power (TEP) measurements on films of $Pb_xIn_{25-x}Se_{75}$ alloys was carried out using the procedure described in chapter 2 in the temperature range of 320 K to 400 K. From the data obtained from these measurement (figure 5.7), it was observed that $Pb_{01}In_{24}Se_{75}$ was the only composition which showed *p*-type conduction. Temperature dependence of the Seebeck coefficient (Q) of all thin film samples is shown in figure 5.8a. The variation of activation energy for TEP with composition is shown in figure 5.8b. The activation energy shows a sharp fall at the composition at which the *p*- to *n*- transition occurs.

Table 5.4: Seebeck coefficient and Activation energy for TEP of Pb-In-Se glasses.

Sample composition	Q ($mV.K^{-1}$)	E_s (eV)
$Pb_{01}In_{24}Se_{75}$	3.43 ± 0.10	1.50 ± 0.03
$Pb_{03}In_{22}Se_{75}$	-1.58 ± 0.05	1.21 ± 0.03
$Pb_{05}In_{20}Se_{75}$	-4.82 ± 0.15	1.08 ± 0.03
$Pb_{07}In_{18}Se_{75}$	-6.35 ± 0.20	0.99 ± 0.03

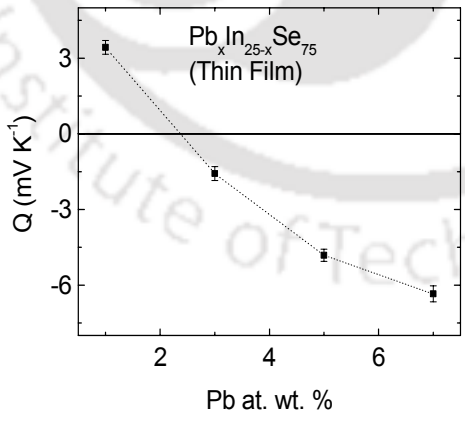

Figure 5.7: Variation of Q of Pb-In-Se thin films as a function of Pb content.

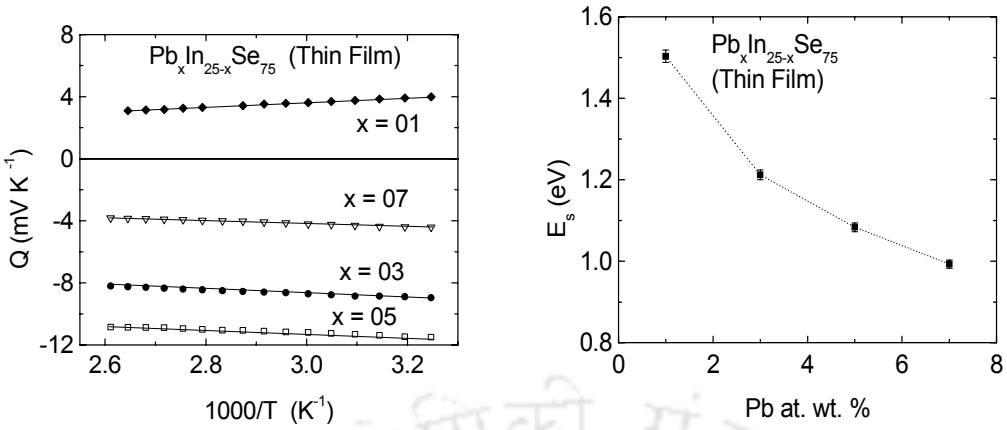

Figure 5.8: (a) Q versus 1000/T plots, and (b) E_s versus composition plot for Pb-In-Se films.

From the slope Q versus 1000/T curves, the activation energy for TEP (E_s) was calculated and tabulated in the table 5.4. The carrier type reversal phenomenon in these glasses could be understood on the basis of Kolobov's Valence Alternation Pair model [64]. In this series of glasses, Pb is assumed to be present in the Pb^{2+} state. On addition of Pb to In-Se, some Se_3^+ states get converted into Se_1^-. So the positive charge defect states which are responsible for the generation of holes in the valence band decreases in number as Pb is added. This disturbs the equilibrium between the positive and negative charge defect states leading to the unpinning the Fermi level and shifting it towards conduction band edge. It has to be mentioned that SEM and XRD studies show the presence of a nanocrystalline phase in these glasses. Hence, models based on pecolation of sub-microscopic clusters cannot be entirely ruled out.

5.3. Electrical conductivity studies

d. c. electrical resistivity of these samples was measured in the temperature range of 300 K to 385 K by the procedure outlined in chapter 2. $\ln(\sigma_{sheet})$ versus 1000/T plots of the four compositions are shown in the figure 5.10. The activation

energy for the electrical conduction (E_σ) was calculated from the slopes of the least squares fits to the $\ln(\sigma_{sheet})$ versus 1000/T plots. E_σ values calculated are tabulated in table 5.5. Variation of E_σ with Pb content is shown in figure 5.11.

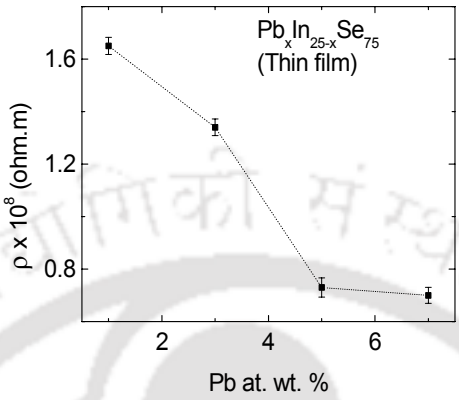

Figure5.9: Variation of Pb-In-Se thin films with composition.

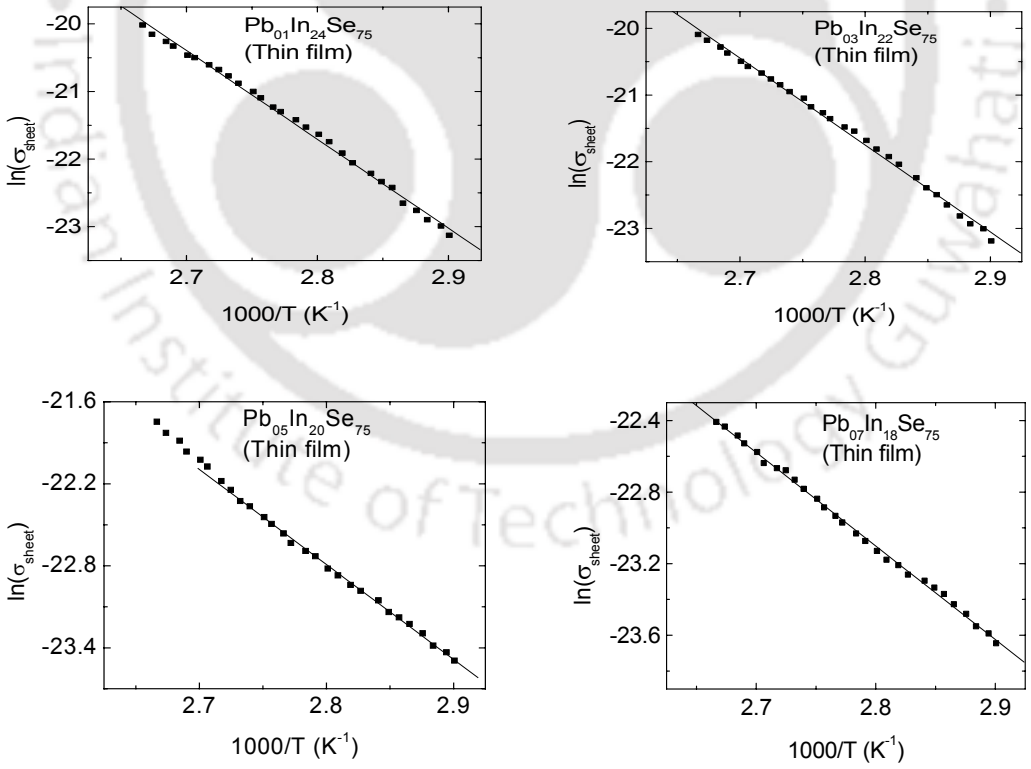

Figure 5.10: $\ln(\sigma_{sheet})$ versus 1000/T plots of Pb-In-Se glasses.

Table 5.5: Activation energy for electrical conduction (E_σ) and sheet resistance (ρ_{sheet}) of Pb-In-Se thin films.

Sample composition	E_σ (eV)	ρ_{sheet} x 10^8 (ohm.m)
$Pb_{01}In_{24}Se_{75}$	1.13 ± 0.03	1.65 ± 0.03
$Pb_{03}In_{22}Se_{75}$	1.11 ± 0.03	1.34 ± 0.03
$Pb_{05}In_{20}Se_{75}$	0.63 ± 0.02	0.73 ± 0.03
$Pb_{18}In_{17}Se_{75}$	0.45 ± 0.01	0.70 ± 0.03

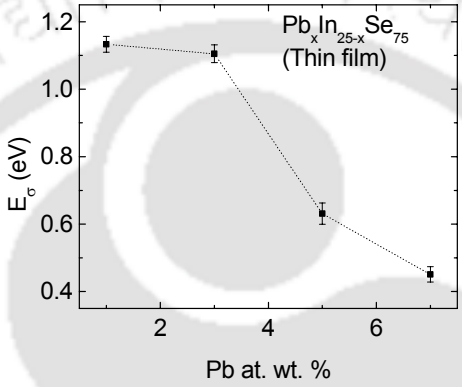

Figure5.11: Variation E_σ of Pb-In-Se thin films with composition.

It can be seen from figure 5.10 that all the data in the temperature range 323 K to 378 K could be fit to the Arrhenius form of relation 1.12. This implies that in this temperature range, the conduction is determined by the band transport mechanism. The composition dependence of activation energy for electrical conduction figure 5.11 shows a subtle slope change after the 3 at. wt. % Pb composition at which the carrier type reversal occurs. ρ_{sheet} versus composition plot (figure 5.9) for these glasses show a slope change after 3 at. wt. % Pb, the composition at which the carrier reversal takes place.

5.4. Optical Studies

Figure 5.12 shows the $(\alpha h\nu)^{1/2}$ versus hv plots of the Pb-In-Se system. The optical band gap energy value obtained from these curves are tabulated in table 5.6.

The composition dependence of optical band gap energy (E_{opt}) is shown in figure 5.13.

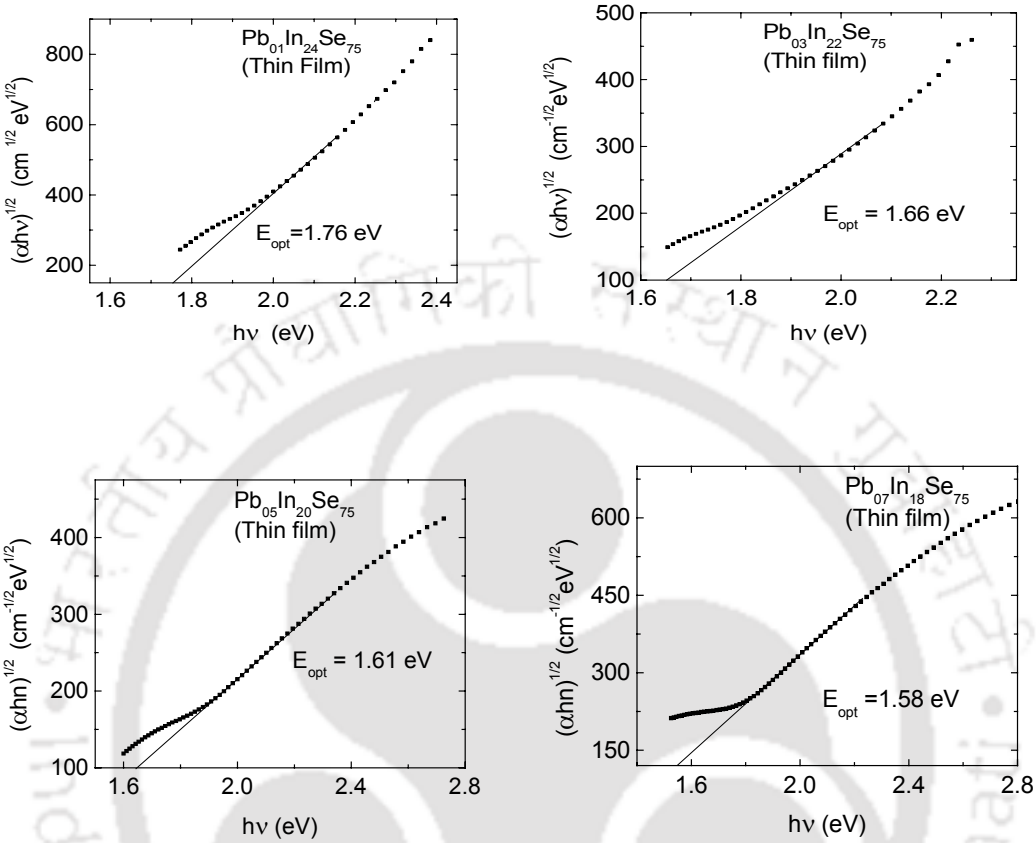

Figure 5.12: $(\alpha h\nu)^{1/2}$ versus hν plots of Pb-In-Se thin films.

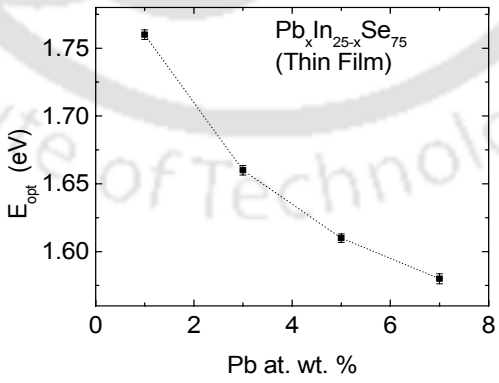

Figure 5.13: Variation of optical band gap energy E_{opt} with composition of Pb-In-Se thin films.

Table 5.6: Optical band gap energy of Pb-In-Se thin films.

Sample composition	E_{opt} (eV)
$Pb_{01}In_{24}Se_{75}$	1.76 ± 0.01
$Pb_{03}In_{22}Se_{75}$	1.66 ± 0.01
$Pb_{05}In_{20}Se_{75}$	1.61 ± 0.01
$Pb_{07}In_{18}Se_{75}$	1.58 ± 0.01

The band gap energy of Pb-In-Se system decreases as Pb content increase as shown in figure 5.13. This behaviour could be explained on the basis of the variation in average bond energy of the glasses. The average bond energy of Pb-Se is lower than the average bond energy of In-Se (Appendix-I). So when the Pb content increases In-Se bonds are replaced by the Pb-Se bonds in this system. This results in the lowering of the average bond energy of the system. Hence optical band gap decreases on addition of Pb to the In-Se.

5.5. Summary

The main features of the studies on the Pb-In-Se system are as follows:

1. From the sample preparation procedure it was established that bulk samples could not be prepared in completely amorphous form. Only an alloy of Pb-In-Se containing Se crystallites embedded in an amorphous matrix could be prepared. Thin films of these materials could not be prepared in completely amorphous form. However, the nucleation of the crystalline phase could be reduced by depositing the films at lower temperature. The particle size of crystallites in Pb-In-Se ranged from 75 Å to 160 Å. Particle size decreased when the films were deposited at lower temperature.
2. However, T_g and TEP data on melt quenched bulk Pb-In-Se showed a good correspondence with the data reported in literature. *p*- type to *n*- type transition could be observed in this partially crystallized bulk samples.

3. Thermoelectric power measurements on thin film samples with nanometer crystallites showed that the carrier reversal occurs at 3 at. wt. % Pb. The charge carrier type reversal phenomenon is attributed due to the presence of charged defect states disturbing the equilibrium of the VAPs. But the presents of nanaometer size crystallites shows that an alternate model for the carrier reversal, based on percolation of sub-microscopic clusters could be ruled out.

4. Electrical resistivity of these thin amorphous films with nanocrystallites decrease with the increase in Pb content.

5. The optical band gap also decreases as the Pb content was increased. This behaviour is attributed to the lowering of average bond energy on the addition of Pb in In-Se

भारतीय प्रौद्योगिकी संस्थान गुवाहाटी
Indian Institute of Technology Guwahati

Chapter 6

Conclusions

Three systems of Pb modified chalcogenide glasses, namely, Pb-Ge-Se, Pb-Ge-Se-Te, Pb-In-Se exhibiting a majority charge carrier reversal from *p*-type to *n*-type have been studied in this thesis work. The choice of these three systems were made on the basis of certain reports in the literature indicating the possibility of obtaining *n*-type glasses in these glass systems. The classical case is that of Pb-Ge-Se, on which some research publications exist. Two series of Pb-Ge-Se glasses, namely, $Pb_xGe_{42-x}Se_{58}$ ($3 \leq x \leq 15$) and $Pb_{20}Ge_xSe_{80-x}$ ($17 \leq x \leq 24$) were studied in detailed in bulk and thin film forms in chapter 3 of this thesis. The studies on thin films of this system are entirely new and correspond to unreported work. In the fourth chapter, two series of Pb-Ge-Se-Te glasses, *viz.*, $Pb_xGe_{42-x}Se_{48}Te_{10}$ ($3 \leq x \leq 15$) and $Pb_{20}Ge_xSe_{70-x}Te_{10}$ ($17 \leq x \leq 24$) were studied in bulk and thin film form. This study follows the only report on bulk $Pb_xGe_{42-x}Se_{48}Te_{10}$ glasses report in the literature. The third system *i.e.*, $Pb_xIn_{25-x}Se_{75}$ was taken up for study since our literature showed only two reports on this glass system. Since this system happened to be the only glass system without Ge to show carrier reversal, this system was studied in bulk and thin film form in chapter 5. Experimental techniques such as DSC, TEP, XRD, electrical resistivity, spectrophotometry and microhardness were used as the main probes of study, supported by SEM / EDX and ellipsometry work. The results obtained were analysed within the scope of the available techniques.

Direct comparison of the results obtained on Pb-Ge-Se glasses (chapter 3) with those obtained on Pb-Ge-Se-Te glasses (chapter 4) brings out the influence of Te substitution in these glasses. This analysis provides a means to tailor the

properties of these glasses for future applications. A comparison between the properties of the bulk and thin films of the same system shows that most of the features observed in the bulk are reproduced in the thin film form. The two-dimensional constraint of the thin films leads to slight variations in the properties, which provides a means to understand the 2-d and 3-d forms of chalcogenide glasses.

The studies on Pb-In-Se system (chapter 5) showed that a completely amorphous bulk sample could not be obtained by the melt quenching method. The present results on the partially crystalline Pb-In-Se glasses agreed well with the data published earlier. The crystallite size could be controlled in the case of thin films. But the nanometer sized Se crystallites could not be completely suppressed by attempts to deposit at 200 K. Hence, the carrier reversal phenomenon encountered in bulk and thin film samples of Pb-In-Se obtained in the present work cannot be treated in the same manner as the ones observed in Pb-Ge-Se and Pb-Ge-Se-Te glasses. *p*- and *n*-type carrier reversal is not new in crystalline semiconductors as seen by many reports in the literature. However, the presence of nanometer sized crystallites in this system ensures that this conduction mechanism change in this system is of contemporary relevance.

It would be interesting to investigate the effect of crystallite size on various physical properties of the Pb-In-Se films. Transmission electron microscope studies would provide a better estimate of crystallite size. Light induced structural changes on thin films of Pb modified glasses would be interesting since the density of the VAP is modified in these glasses with the addition of Pb.

APPENDIX - I

Calculation of bond energy of A-B type bonds from A-A type bonds

Rao and Mohan [166] calculated the bond energies of a variety of III-VI, V-VI and IV-VI elements using the method described by Sanderson [167]. The single covalent bond energy values of Ge-Ge, Se-Se and Pb-Pb were taken from the above source and heteronuclear bond energies (Ge-Se, Pb-Se) were calculated using Pauling's formula [168],

$$D(A\text{-}B) = [D(A\text{-}A) \,.\, D(B\text{-}B)]^{1/2} + 30(x_A - x_B)^2$$

where D(A-A) and D(B-B) are the single bond energies of atom A and atom B, respectively; x_A and x_B are the electronegativities of atom A and atom B, respectively.

Electronegativity values can be expressed in three different scales like Pauling's, Allred-Rochow's and Mulliken's scale. This results in different single bond energy value for heteronuclear atoms depending the electronegativity scale used. The Allred-Rockow electronegativity scale is accepted by the International Union for Pure and Applied Chemistry (IUPAC). To avoid such discrepancy, the single bond energy suggested by Sanderson and Allred-Rochow electronegativity values were used for calculating the single bond energy values of heteronuclear bonds in the present work. The average bond energy for the relevant bonds are tabulated in table A.1 and A.2.

Table A.1: Electronegativity and bond energies of homonuclear bonds of Pb, Ge, Se, Te, In.

Element	Electronegativity	(A-A) Bond	Bond energy. ($kCal.mol^{-1}$)
Pb	1.6	Pb-Pb	20.5
Ge	2.0	Ge-Ge	49.1
Se	2.5	Se-Se	49.3
Te	2.0	Te-Te	38.0
In	1.5	In-In	20.3

Table A.2: Bond energies of heteronuclear bonds of Pb, Ge, Se, Te, In.

(A-B) Bond	Bond energy ($kCal.mol^{-1}$)
Pb-Ge	36.5
Pb-Se	55.3
Ge-Se	56.2
Pb-Te	43.8
Ge-Te	43.1
Se-Te	48.1
Pb-In	20.3
In-Se	61.6

References

1. A. K. Varshneya, Fundamentals of Inorganic Glasses, Academic Press, INC, New York, 1993.
2. Materials Advisory Board, Nat. Acad. Sci. Res. Council MAB – 243, 1968.
3. J. Zarzycki, Materials Science and Technology, **9,** Weinheim, New York, 1991.
4. R. Zallen, The Physics of Amorphous Solids, John Wiley, 1983.
5. S. R. Elliott, Physics of Amorphous Materials, Longman, London, 1984.
6. M. W. Zemansky and R. H. Dittman, Heat and Thermodynamics 6 ed., McGraw Hill, Auckland, 1981.
7. A. E. Owen, in Electronic and Structural Properties of Amorphous Conductors, eds. P. G. LeComber and J. Mort, Academic Press, New York, 1973.
8. G. W. Scherrer, J. Non-Cryst. Solids, **123** (1990) 75.
9. M. H. Cohen and D. Turnbull, J. Chem. Phys., **52** (1970) 3038.
10. M. H. Cohen and D. Turnbull, J. Chem. Phys., **31** (1959) 1164.
11. C. A. Angell, J. Non-Cryst. Solids, **73** (1985) 1.
12. C. A. Angell, J. Non-Cryst. Solids, **131-133** (1991) 13.
13. G. Adam and J. H. Gibbs, J. Chem. Phys., **43** (1965) 139.
14. C. A. Angell, W. Sichina, Ann. N. Y. Acad. Sci., **279** (1976) 53.
15. A. Saiter, C. Devallencourt, J. M. Saiter, J. Grenet, Mater. Lett., **45** (2000) 180.
16. R. Bohmer, C. A. Angell, Disorder Effects on Relaxational Processes, ed. R. Richert, Springer, Berlin, 1994.
17. R. J. Nemanich, S. A. Solin, G. Lucovsky, Solid State Commun., **21** (1977) 2734.
18. J. C. Philips, J. Non-Cryst. Solids, **43** (1981) 37.
19. A. L. Renninger, M. D. Rechtin, B. L. Avebach, J. Non-Cryst. Solids, **16** (1974).
20. W. H. Zachariasen, J. Am. Chem. Soc., **54** (1932) 3841.
21. G. Lucovsky, F. L. Galeener, R. H. Geils , R. C. Keezer, Structure of Non-crystalline Materials, Taylor and Francis, 1977.
22. A. Srinivasan, Investigations on the Mechanical Threshold in IV-V-VI Glasses, Ph.D. thesis, Indian Institute of Science, India (1991) (unpublished).
23. P. S. L. Narasimham, A. Giridhar, S. Mahadevan, J. Non-Cryst. Solids, **43** (1981) 365.

24. A. Giridhar, P. S. L. Narasimham, S. Mahadevan, J. Non-Cryst. Solids, **43** (1981) 29.
25. S. Mahadevan, A. Giridhar, A. K. Singh, J. Non-Cryst. Solids, **57** (1983) 423.
26. M. F. Thorpe, J. Non-Cryst. Solids, **57** (1983) 355.
27. J. C. Phillips, M. F. Thorpe, Solid State Commun., **53** (1985) 699.
28. S. Feng , M. F. Thorpe, E. Garboczi, Phys. Rev. B, **31** (1985) 276.
29. H. He , M. F. Thorpe, Phys. Rev. Lett., **54** (1985) 2107.
30. Y. Cai, M. F. Thorpe, Phys. Rev. B, **40** (1989) 10535.
31. B. L. Halfpap, S. M. Lindsay, Phy. Rev. Lett., **57** (1986) 847.
32. R. Ota, T. Yamate, N. Soga, M. Kunugi, J. Non-Cryst. Solids, **29** (1978) 67.
33. S. Asokan, M. V. N. Prasad, G. Parthasarathy, E. S. R. Gopal, Phys. Rev. Lett., **62** (1989) 808.
34. S. S. Yun, H. Li, R. L. Cappelletti, R. N. Enzweiler, P. Boolchand, Phy. Rev. B, **39** (1989) 8702.
35. J. Y. Duquesne, G. Bellaessa, Europhy. Lett., **9** (1989) 453.
36. K. Tanaka, Phy. Rev.B, **39** (1989) 1270.
37. P. Boolchand, X. Feng, W. J. Breser, J. Non-Cryst. Solids, **293-295** (2001) 384.
38. P. Boolchand, D. G. Georgiev, B. Goodman, J. Optoelectr. Adv. Mater., **3** (2001) 703.
39. Y. Wang, P. Boolchand, M. Micoulaut, Europhys. Lett., **52** (2000) 633.
40. P. Tronc, M. Bensoussan, A. Brenac, Phy. Rev. B, **8** (1973) 5947.
41. S. R. Elliott, J. Phys.: Condens. Matter, **4** (1992) 7661.
42. S. R. Elliott, Phys. Rev. Lett., **67** (1991) 711.
43. D. L. Price, S. C. Moss, R. Reijers, M. L. Saboungi, S. Susman, J. Phys. C: Solid State Phys., **21** (1989) L1069.
44. D. L. Price, S. C. Moss, R. Reijers, M. L. Saboungi, S. Susman, J. Phys.: Condens. Matter, **1** (1989) 1005.
45. L. E. Busse, Phys. Rev. B, **29** (1984) 3639.
46. C. Lin, L. E. Busse, S. R. Nagel, J. Faber, Phys. Rev. B, **29** (1984) 5060.
47. K. Tanaka, Phil. Mag. Lett., **57** (1988) 183.
48. R. J. Dejus, S. Susman, K. J. Volin, D. L. Price, J. Non-Cryst. Solids, **106** (1988) 34.
49. N. Ramesh Rao, P. S. R. Krishna, S. Basu, B. A. Dasannacharya, K. S. Sangunni, E. S. R. Gopal, J. Non-Cryst. Solids, **240** (1998) 221.

50. S. C. Moss, D. L. Price, in “Physics of Disordered Materials”, edited by D. Alder, H. Fritzche, and S. R. Ovshinsky, Plenum, New York, 1985, p. 77.
51. S. R. Elliott, Nature, **354** (1991) 445.
52. S. R. Elliott, Phys. Rev. B, **51** (1995) 8599.
53. L. E. Busse, S. R. Nagel, Phys. Rev. Lett., **47** (1981)1848.
54. N. F. Mott, E. A. Davis, Electronic processes in Non-Crystalline Materials, Clarendon Press, 1971.
55. N. F. Mott, Phil Mag., **22** (1970) 7.
56. P. W. Anderson, Phy. Rev., **109** (1958) 1492.
57. M. H. Cohen, H. Fritzsche, S. R. Ovshinsky, Phy. Rev. Lett., **22** (1969) 1065.
58. E. A. Davis, N. F. Mott, Phil Mag., **22** (1970) 903.
59. J. M. Marshall, A. E. Owen, Phil Mag., **24** (1971) 1281.
60. P. W. Anderson, Phys. Rev. Lett., **34** (1975) 953.
61. R. A. Street, N. F. Mott, Phys. Rev. Lett., **34** (1975) 1293.
62. M. Kastner, Phy. Rev. Lett., **28** (1972) 355.
63. M. D. Kastner, D. Adler, H. Fritzsche, Phys. Rev. Lett., **37** (1976) 1504.
64. A. V. Kolobov, J. Non-Cryst. Solids, **198-200** (1996) 728.
65. R. M. White, J Non-Cryst. Solids, **16** (1974) 387.
66. N. F. Mott, Adv. Phys., **16** (1967) 49.
67. P. Nagels, in Amorphous Semiconductors, 2 ed., ed. M. H. Brodsky, Springer-Verlag, New York, 1985.
68. N. F. Mott, E. A. Davis, Electronic Processes in Non-Crystalline Materials, Oxford, 1979.
69. J. J. Hauser, R. S. Hutton, Phys. Rev. Lett., **37** (1976) 868.
70. J. Lee, J. S. Yi, D. Mangalraj, J. Korean Phys. Soc., **41** (2002) 76.
71. A. R. Patil, P. N. Bhosale, L. P. Deshmukh, Mater. Chem. Phys., **65** (2000) 266.
72. H. Hosono, H. Maeda, Y. Kameshima, H. Kawazoe, J. Non-Cryst. Solids, **230** (1998) 804.
73. R. M. Mehra, S. Kohli, A. Pundir, V. K. Sachdev, P. C. Mathur, J. Appl. Phys., **81** (1997) 7842.
74. W. A. Phillips, Phil. Mag., **34** (1976) 983.
75. H. Mori, K. Gotoh, H. Sakata, J. Non-Cryst. Solids, **183** (1995) 122.
76. T. N. Kennedy, J. D. Mackenzie, Phys. Chem. Glasses, **8** (1967) 169.
77. N. F. Mott, J. Non-Cryst. Solids, **1** (1968) 1.

78. C. Kittel, Introduction to Solid State Physics 7 ed., John Wiley, Singapore, 1996.
79. A. Feltz, Amorphous Inorganic Materials and Glasses, VCH, New York, 1993.
80. B. T. Kolomiet, Vitreous Semiconductors, phys. stat. solidi (b), **7** (1964) 359.
81. J. C. Male, Brit. J. Appl. Phys., **18** (1967) 1543.
82. L. Friedman, J. Non-Cryst. Solids, **6** (1971) 329.
83. T. Holstein, Phil. Mag., **27** (1973) 225.
84. V. R. Panus, J. M. Kasendzov, Z. U. Borisova, Izvest. Aakad. Nauk. Neorg. Mater., **4** (1968) 778.
85. E. B. Ivkin, B. T. Kolomiec, E. A. Lebedev, Dokl., Akad, Nauk. SSSR, Phys. Ser., **28** (1964) 1190.
86. D. Weaire, M. F. Thorpe, Phys. Rev. B, **4** (1971) 2508.
87. J. Tauc, Amorphous and Liquid Semiconductors, ed. J. Tauc, Plenum Press, 1974.
88. K. Shimakawa, Phil. Mag. B, **46** (1982) 123.
89. J. Tauc, Mat. Res. Bull., **5** (1970) 721.
90. J.D. Dow, D. Redfield, Phys. Rev. B, **5** (1972) 5949.
91. R. A. Street, Solid State Comm., **24** (1977) 363.
92. J. S. Jen, M. R. Kalinowski, J. Non Cryst Solids, **38-39** (1980) 21.
93. H. Doweidar, Phys. Chem. Glasses, **39** (1998) 286.
94. A. Cousen, W. E. S. Turner, Glastech. Ber., **6** (1928) 393.
95. R. Jabra, J. Pelous, J. Phalippou, J. Non-Cryst. Sol., **37** (1980) 349.
96. M. Yamane, J. D. Mackenzie, J. Non-Cryst. Solids, **15** (1974) 153-64.
97. A. Petzold, F. G. Withsmann, H. Von Kampiz, Glasteck Ber., **43** (1961) 56.
98. J. E. Neely, J. D. Mackenzie, J. Mater. Sci., **3** (1968) 603.
99. J. E. Shelby, Introduction to Glass Science and Technology, RSC, 1997.
100. D. R. Swiler, A. K.Varhneya, R. H. Callahan, J. Non-Cryst. Solids, **125** (1990) 250.
101. A. N. Sreeram, A. K. Varshneya, D. R. Swiler, J. Non-Cryst. Solids, **130** (1991) 225.
102. J. Chitralekha, A. Srinivasan, K. Chattopadhyay, E. S. R. Gopal, phys. stat. solidi (b), **197** (1996) 343.
103. A. R. Hilton, C. E. Jones, M. Baru, Phys. Chem. Glasses, **7** (1966) 105.
104. M. Kastner, J. Non-cryst. Solids, **31** (1978) 223.

105. N. Tohge, Y. Yamamato, T. Minami, M. Tanaka, Appl. Phys. Lett., **346** (1979) 640.
106. N. Toghe, T. Minami, Y. Yamamoto, M. Tanaka, J. Non-Cryst. Solids, **37** (1980) 23.
107. N. Toghe, H. Matsuo, T. Minami, J. Non-Cryst. Solids, **95-96** (1987) 809.
108. T. Takahashi, T. Sagawa, H. Hamanaka, J. Non-Cryst. Solids, **65** (1984) 261.
109. P. Nagel., L. Tichy, A. Triska, H. Ticha, J. Non-Cryst. Solids, **59-60** (1983) 1015.
110. J. M. Saitar, T. Derrey, C. Vautieret, J. Non-Cryst. Solids, **77-78** (1985) 1169.
111. P. Nagels , M. Rotti, S. Vikhrov, J. Phys. Coll., **42** (1981) C4907.
112. N. Tohge, T. Minami, Y. Yamamato, M. Tanaka, J. Appl. Phys., **51**(1980) 1048.
113. K. L. Bhatia, J. Non-Cryst. Solids, **54** (1983) 17.
114. D. P. Gossain, K. L. Bhatia, G. Parthasarathy, E. S. R. Gopal, Phys. Rev B, **32** (1985) 2727.
115. P. Takahashi, J. Non-Cryst. Solids, **44** (1981) 239.
116. R. Mathur, A. Kumar, Solid State Commun., **59** (1986)163.
117. G. Mathew, J. Philip, J. Phys.: Condens. Matter, **11** (1999) 5283.
118. N. Tohge, Y. Yamamoto, M. Tanaka, J. Non-Cryst. Solids, **38-39** (1980) 283.
119. K. L. Bhatia, A. K. Sharma, J. Non-Cryst. Solids, **61** (1986) 285.
120. S. Kumar, S. C. Kashyap, K. L. Chopra, J. Non-Cryst. Solids, **85** (1986) 100.
121. M. K. Rabinal, N. Ramesh Rao, K. S. Sangunni, E. S. R. Gopal, Phil. Mag. B, **70** (1994) 89.
122. M. K. Rabinal, K. S. Sangunni, E. S. R. Gopal, S. V. Subramanyam, Solid State Commun., **88** (1993) 251.
123. S. Thomas, J. Philip, Solid State Commun., **107** (1998) 423.
124. B. Thangaraju, R Ganesan, N. A. Bhat, K. S. Sangunni, E. S. R. Gopal, J. Optoelctro. Adv. Mater., **2** (2000) 91.
125. A. K. Agnihotri, A. Kumar, A. N. Nigam, J. Non-Cryst. Solids, **93** (1987) 267.
126. S. Kumar, S. C. Kashyap, K. L. Chopra, J. Appl. Phys**. 72** (1992) 2066.
127. G. Saffarini, J. M. Saiter, Mater. Lett., **46** (2000) 327.
128. S. Rahman, K. V. Muralidhar, G. S. Sastry, Phys. Chem. Glasses, **34** (1993) 176.
129. S. Kumar, S. C. Kashyap, K. L. Chopra, Phil. Mag. Lett., **58** (1988) 24.

130. M. K. Rabinal, K. S. Sangunni, E. S. R. Gopal, S. V. Subramanyam, Physica B, **205** (1995) 403.
131. B. Vaidyanathan, S. Murugavel, S. Asokan, K. J. Rao, J. Phys. Chem B, **101** (1997) 9717.
132. K. L. Bhatia, S. K. Mallik, N. Kishore, S. P. Singh, Phil. Mag. B, **66** (1992) 587.
133. S. K. Mallik, K. L. Bhatia, N. Kishore, J.S. Phor, J. Non-Cryst. Solids, **142** (1992) 55.
134. S. Rahman, M. V. Ramana, G. S. Sastry, Phys. Chem. Glasses, **33** (1992) 209.
135. R. Ganesan, B. Thangaraju, K. S. Sangunni, E. S. R. Gopal, J. Optoelectro. Adv. Mater., **3** (2001) 467.
136. S. Murugavel, S. Asokan, Phys. Rev. B **58** (1998) 4449.
137. S. Kohli, V. K. Sachdev, R. M. Mehra, P. C. Mathur, phys. stat. solidi (b), **209** (1998) 389.
138. P. Scherrer, Nachr. Ges. Wiss. Gottingen, pp. 98, 1918.
139. E. Lifshin, X-ray Characterisation of Materials, Wiley-VCH, 1999.
140. P. Dutta, Current Science, **78** (2000) 1478.
141. E. S. Watson, M. J. O'Neil, J. Justin, N. Brener, Anal. Chem., **36**3 (1964) 123.
142. J. Wolny, J. Soltys, R. Kokoszka, J. Non-Cryst. Solids, **91** (1987) 209.
143. N. P. Bansal, R. H. Doremus, J. Thermal Analysis, **29** (1984) 115.
144. L. Kashif, A. A. Soliman, A. M. Sanad, Phys. Chem. Glasses, **39** (1998) 195.
145. B. Indrajit Sharma, A. K. Pattanaik, A. Srinivasan, Phys. Chem. Glasses, **43** (2002) 12.
146. M. J. O'Neill, Anal. Chem., **38** (1966) 1331.
147. T. A.Vilgis, Phys. Rev. B, **47** (1993) 2882.
148. T. Komatsu, R. Ike, R. Sato, K. Matusita, Phys. Chem. Glasses **36** (1995) 216.
149. R. M. A. Azzam, N. M. Bashara, Ellipsometry and Polarized Light, North Holland, Amsterdam, 1977.
150. ASM Handbook: Materials Characterization, **10,** ASM International, 1996.
151. J. Philibert, R. Tixier, Quantitative Electron Probe Microanalysis, NBS, Gaithersburg, 1968.
152. Y. C. Ratnakaram, A. Viswanadha Reddy, Phys. Chem. Glasses, **41** (2000) 121.
153. D. M. Sclapp, Phys. Chem. Glasses, **6** (1965) 168.
154. K.W. Peter, J. Non-Cryst. Solids, **5** (1970) 103.

155. D. K. Schroder, Semiconductor Material and Device Characterization, John Wiley, New York 1990.
156. L. P. Hunter, Hand book of Semiconductor Electronics, McGraw Hill, New York, 1962.
157. A. C. Melissinos, Experiments in Modern Physics, Academic Press, New York 1966.; W. Shockley, Electrons and Holes, DVN, New York, 1950.
158. J. Lindmayer and C.Y. Wriegley, Fundamental of Semiconductor Devices, East West Press, 1971.
159. D.J. Griffith, Introduction to Electrodynamics 2 ed., Prentice Hall India, New Delhi, 1995.
160. V. A. Feltz, L. Senf, Z. Anorg. Allg. Chem., **444** (1978) 195.
161. D. Linke, M. Gitter, F. Krug, Z. Anorg. Allg. Chem., **444** (1978) 217.
162. S. C. Rowland, F.Ritland, D.Haferburns, A.Bienenstock, Proc. 7th Int. Conf. Amorphous Liquid Semicond., Edinburgh, 1977.
163. P. Cortes, S. Montserrat, J. Ledru, J. M. Saiter, J. Non.-Cryst. Solids, **235-237** (1998) 522.
164. A. Hruby, Czech. J. Phys. B **22** (1972) 1187.
165. D. D. Thornburg, Mat. Res. Bull., **9** (1974) 1481.
166. K. J. Rao, R. Mohan, Solid State Commun., **39** (1991) 1065.
167. R. T. Sanderson, Chemical bonds and bond energies, ed. E. M. Loebl, vol: **21,** Academic Press, London & New York, 1971.
168. L. Pauling, The Nature of Chemical Bond, Oxford & IBH, 3rd ed. (1967)

****

भारतीय प्रौद्योगिकी संस्थान गुवाहाटी
Indian Institute of Technology Guwahati

Research papers published

Journal

1. A compact cryostat for electrical studies on semiconductors
   A. K. Pattanaik, C. Borgohain, A. Srinivasan, *Indian J. Phys*., **74A** (2000) 307.
2. Differential scanning calorimeter studies on Pb modified Ge-Se-Te glasses
   A. K. Pattanaik, A. Srinivasan, *J . Mater. Sci.,* **38** (2003) 2511.
3. Microhardness of Pb modified chalcogenide glasses
   A. K. Pattanaik, A. Srinivasan, *J. of Optoelectr. Adv. Materials*, **5** (2003) 35.
4. Optical and electrical studies of Pb-Ge-Se thin films
   A. K. Pattanaik, A. Srinivasan (Submitted to Thin Solid Films)
5. Optical and electrical studies of Pb-Ge-Se-Te thin films.
   A. K. Pattanaik, A. Srinivasan (Submitted to Semiconductor Science and Technology)
6. Electrical and optical properties of amorphous $Pb_xIn_{25-x}Se_{75}$ films with a dispersion of nanocrystallites
   A. K. Pattanaik, A. Srinivasan (Accepted in *J. of Optoelectr. Adv. Materials*)

Conferences

1. Optical band gap of Pb-Ge-Se glasses,
   A. K. Pattanaik, A. Srinivasan, *Solid State Physics (India),* **42** (1999) 289.
2. Composition dependence of the Density and Molar Volume of Pb- modified Ge-Se glasses
   B. I. Sharma, A. K. Pattanaik, A. Srinivasan, *Solid State Physics (India),* **43** (2000) 210.
3. Non isothermal and Optical properties of Pb- modified Ge-Se glasses
   A. K. Pattanaik, A. Srinivasan, *Proc Of VIth ATPC 2001*, **1** (2001) 188.
4. Microhardness of Pb modified Ge-Se glasses,
   A. K. Pattanaik, A. Srinivasan, *Solid State Physics (*India), **45** (2002)
5. Neutron diffraction studies on the Pb-modified chalcogenide glasses exhibiting majority charge carrier reversal
   B.I.Sharma, A.K.Pattanaik, A. Srinivasan, P.S.R. Krishna, A.B.Shinde, *Solid State Physics (*India), **45** (2002)